# Online Condition Monitoring of Lithium Ion Batteries by Performing Impedance Spectroscopy Using a DC-DC Converter




**Prepared By**

**SEAN MOORE**

Department of Electrical Engineering

University of Cape Town

**March 2018**

Submitted to the Department of Electrical Engineering at the University of Cape Town in partial fulfilment of the academic requirements for a Master of Science degree in **ELECTRICAL ENGINEERING**

# DECLARATION

1. I know that plagiarism is wrong. Plagiarism is to use another's work and pretend that it is one's own.
2. I have used the IEEE convention for citation and referencing. Each contribution to, and quotation in, this final year project report from the work(s) of other people, has been attributed and has been cited and referenced.
3. This Master's Thesis Dissertation is my own work.
4. I have not allowed, and will not allow, anyone to copy my work with the intention of passing it off as their own work or part thereof
5. I know the meaning of plagiarism and declare that all the work in the document, save for that which is properly acknowledged, is my own. This thesis/dissertation has been submitted to the Turnitin and I confirm that my supervisor has seen my report and any concerns revealed by such have been resolved with my supervisor.

Name: SEAN MOORE

Signature: Signed by candidate

Date: 28 March 2018

# ACKNOWLEDGMENTS

This dissertation was made possible by the guidance and support of many people throughout my research. To my supervisor, Prof. Paul Barendse, I would like to say a big thank you for giving me this opportunity and for guiding me to complete my masters.

To Mr. Chris Wozniak and Mr. Philip Titus for their technical assistance in the laboratory and for imparting so much of the technical expertise. To my research group I would like to express my gratitude for the support and friendship with a special thanks to Olufemi Olayiwola for the countless hours you put in assisting me.

The financial assistance of the National Research Foundation (NRF) towards this research is hereby acknowledged. Opinions expressed, and conclusions arrived at, are those of the author and are not necessarily to be attributed to the NRF.

And finally, to my incredible parents. I could not have done this without their constant encouragement, prayer and support. I am so grateful for everything they have done for me and know that I am truly blessed to be their son. This thesis is dedicated to them.

# ABSTRACT

Li-Ion batteries are currently being used extensively in a variety of applications such as portable electronics, electric vehicles and grid storage applications, due to the high demand for high power and high energy density storage batteries. However, the usage of Li-Ion batteries requires extensive condition monitoring to increase overall performance and life expectancy. This research is focused on implementing rapid online condition monitoring techniques, using signal injection via the associated power converter in the battery management system.

The technique implemented in this work is known as Electrochemical Impedance Spectroscopy (EIS). EIS is a well-known technique, that has been used to characterize an electrochemical cell's behaviour and state by monitoring changes in the cell's impedance. This is accomplished by injecting currents at different frequencies into the battery and measuring the voltage response. This technique is conventionally implemented, using standard Frequency Response Analysers (FRA), while the battery is disconnected from the load (offline) due to the long procedural times involved. This has limited the use of EIS to laboratory testing.

In recent years, there has been literature regarding incorporating EIS testing into the battery system, which is done in mainly 2 ways, by including a linear amplifier into the system to inject the current perturbations directly, or by using the existing circuitry in the BMS (typically the DC-DC converter) to inject the current perturbations using various control techniques. Although, these strategies have been applied in literature for online systems, they are still riddled with a lengthy EIS measurement time issue.

This work seeks to significantly reduce the associated testing time with the use broadband signals to implement Impedance Spectroscopy for online systems via the associated BMS converter. Broandband Impedance Spectroscopy (BIS) is implemented by injecting a signal with multiple frequencies concurrently as this allows for quicker measurement. The main contribution of this work is the real-time implementation of a multi-sine broadband excitation via a bi-directional converter that can be used in a varying system. The results obtained were compared to results from an industry standard FRA and showed to produce Nyquist plots with a reasonable error.

# Contents

# LIST OF FIGURES

**List of Tables**

# LIST OF ABBREVIATIONS

This section describes some of the abbreviations used in this thesis

| | | |
|---|---|---|
| Li-Ion | - | Lithium Ion |
| EIS | - | Electrochemical Impedance Spectroscopy |
| SoH | - | State of Health |
| BMS | - | Battery Management System |
| RUL | - | Remaining Useful Life |
| CC/CV | - | Constant Current Constant Voltage |
| SEI | - | Solid Electrolyte Interface |
| EEC | - | Electrical Equivalent Circuit |
| OCV | - | Open Circuit Voltage |
| SNR | - | Signal to Noise Ratio |
| THD | - | Total Harmonic Distortion |

# Chapter 1. INTRODUCTION

## 1.1 BACKGROUND TO STUDY

Battery technologies have become a major research area in recent years. This is driven by the increasing need for energy storage in portable devices, the rapid deployment of renewable sources which often require storage, and the high energy demand required by electric vehicles.

Lithium Ion (Li-Ion) batteries are at the forefront of the conversation and are regarded by many to be the most prominent technology due to its high energy density and high power capabilities [1]. The choice of battery technology developed and utilized in the industry, extends beyond the energy and power considerations. The cycle life, cost, safety and reliability during usage are also key factors that require attention. Presently, Li-Ion cells are deemed to be expensive when compared to other battery technologies and have a few safety issues associated with their usage. Therefore, there is a need to effectively monitor the health of the Li-Ion batteries to maximise their usage and life span.

There is research focused on improving the electrochemistry of the cell, as well as research targeted at improving the power electronic interface to the battery in attempt to increase efficiency and introduce advanced battery monitoring techniques into the Battery Management System (BMS). Most BMS systems monitor the voltage, current and temperature, however, they may not always provide sufficient information about the battery as they are based on overly simplistic models [2]. There are a variety of tests that can be conducted on Li-Ion cells to monitor various aspects of the cell, such as State of Charge (SoC), State of Health (SoH) and Remaining Useful Life (RUL) however many of these tests found in literature tend to be offline tests conducted with expensive Frequency Response Analysers (FRA) while the battery is out of operation. This makes continual monitoring of the battery difficult.

This work is based on the application of Electrochemical Impedance Spectroscopy (EIS) for battery condition monitoring systems. EIS is a very common offline technique for modelling the impedance associated with a cell. It is conducted by injecting small sinusoidal perturbations at varying frequencies into an electrochemical system and measuring the response. This allows more information on the internal parameters of the cell to be obtained as compared to only the passive monitoring of the voltage and current. It has been shown in literature that EIS can be used to obtain the SoC, SoH, temperature and RUL of the battery system. It is also useful to know how the

impedance of the battery system's internal impedance directly impacts efficiency; output power and heat being generated in the batteries.

In recent years, a lot of attention has been placed on implementing EIS on an online system. This enables EIS to perform continual state monitoring of batteries and thus reduce the cost associated with taking the batteries out of service. Impedance Spectroscopy has been demonstrated on online systems by using the power converters (linear converters and switched mode power converters) to inject the measurement signal. However little emphasis is given to the variability of the load and other variable sources connected to the converter such as a wind generator. Renewable sources pose an issue due to their variability in generation.

Another limitation for online EIS is the long procedural duration, which is derived as the sum of the period of all the perturbation signals required. This limitation has however, been successfully addressed in recent years using Broadband Impedance Spectroscopy (BIS) techniques which inject multiple frequencies in a single instance instead of injecting each frequency separately [3] [4] [5].

The ultimate purpose of this thesis is to explore the use of BIS techniques in a switching converter to monitor the states of a battery in the presence of variable conditions.

## 1.2 RESEARCH QUESTIONS

The research question in focus of this dissertation is:

*"Can Broadband Impedance Spectroscopy be performed on an electrochemical cell in a switching converter to monitor the impedance of a Li-Ion battery"*

This question is answered in this thesis by the sequential addressing of the of the following individual questions:

- What are the common battery technologies used in industry?
- How is EIS implemented and what information can it provide about a battery cell?
- What converter topologies are currently being used in industry to interface with batteries?
- How can these current configurations and control methods be modified to accommodate impedance spectroscopy in the electrochemical cell?
- Can broadband signals be injected into the Li-Ion cell and be reliably measured via signal analysis techniques?
- Can BIS be conducted during charging and discharging in a switching converter?

- Can broadband impedance spectroscopy be effectively conducted on a Li-ion battery under a varying system such as wind generator?

## 1.3 RESEARCH APPROACH AND OBJECTIVES

The research question will be answered by meeting the following objectives:

- Conduct a literature review on electrochemical cells and determine the cells that are currently being used for high power and high energy applications.
- Conduct a literature review on current condition monitoring techniques for batteries with an emphasis on EIS and BIS techniques.
- Investigate different battery modelling techniques that can be used with EIS techniques.
- Design, simulate and build a switch mode converter to interface with a battery for use in a standalone power system connected to a varying load and small wind generator.
- Design the control system for implementing BIS and EIS using the converter and evaluate its performance.

## 1.4 RESEARCH METHODOLOGY

This project makes use of 2 types of methodologies, analytical and experimental. The analytical section deals with theory and modelling of the converter and BIS signals. Simulations were performed on a combination of MATLAB, Simulink and LTSPICE. Results were obtained from a running system and were verified against an industry standard FRA (NOVA AUTOLAB PGSTAT302N).

## 1.5 SCOPE AND LIMITATIONS

This study is focussed on achieving impedance spectroscopy results for Li-Ion cells using a DC electronic load and a custom-built DC-DC switching converter. The use of these impedance results to infer SoC, SoH or any other electrochemistry characteristic of the cell is out of scope in this thesis and this thesis solely demonstrates the converters ability to deliver reliable impedance results.

## 1.6 CONTRIBUTION OF WORK AND PUBLICATIONS

The major contribution of this work is to demonstrate broadband impedance spectroscopy on a Li-Ion battery pack using a switching converter while it is connected to a varying system. A conference paper from this work has already been published in IEEE regarding the use of BIS in a switching converter. This is given as reference [6].

## 1.7 PLAN OF DEVELOPMENT

**Chapter 2** provides the literature review of the various commercially available battery technologies with emphasis on Li-Ion batteries. This is followed by a review of the most common online battery monitoring techniques, specifically focusing on Impedance Spectroscopy (IS) methods. This is followed by a review of DC-DC converters and how Impedance Spectroscopy methods have been applied using switching converters, as found in literature.

**Chapter 3** contains the analytical modelling of the converter and BIS techniques. It starts off with the signal design of the BIS signals that are used in simulations and experimentation. The chapter then develops the mathematical description of the converter and state-space averaging techniques are performed to determine the required transfer function. This transfer function is used to create a closed loop control for the power converter and to determine the relationship between the current and duty cycle for injecting the BIS signal. The chapter ends by describing the injection of the perturbation signals into the converter while also performing simulations.

**Chapter 4** describes the experimental setup and methodology. It begins by discussing the implementation of EIS and BIS using the controllable electronic load. The chapter then proceeds to describe the construction of the DC-DC converter and then the implementation of BIS on the switching converter.

**Chapter 5** presents and discusses the results obtained from the experiments described in Chapter 4. The chapter concludes with by evaluating the proposed BIS scheme on a system with a varying emulated wind generator source and load.

**Chapter 6** presents the conclusions and gives recommendations for future research.

# Chapter 2. LITERATURE REVIEW

This chapter presents an overview of the current battery technology and battery testing landscape. It also reviews EIS and BIS techniques as well as online Impedance Spectroscopy techniques, as found in literature.

## 2.1 BATTERIES

There are 3 types of electrochemical battery technologies, primary, secondary (reversible) and reserve batteries. Primary batteries can only be discharged once and then are disposed of. Their popularity exists due to their excellent shelf life and ease of use as they require very little maintenance during their lifetime. They have a higher specific energy and can be stored for longer. The most popular primary battery is the Alkaline battery [7]. They are often used in consumer products, where it is inconvenient to charge the battery. Reserve batteries are also single-use batteries; however the anode and cathode are separated until activation. This means the battery suffers no self-discharge and thus can be kept for prolonged periods. Secondary batteries are rechargeable batteries which have a higher initial cost than primary cells but have a lower life cycle cost. They require regular maintenance as well as monitoring [8].

It should be noted that, the word "cell" and "battery" are often used interchangeably, however, there is a difference between these 2 terms. Battery refers to a connection of cells, whether it be in a parallel or series configuration and this would be the representation used in this research. In many applications, the potential and current requirements need cells to be connected in series and parallel.

### 2.1.1 Secondary Batteries

The research into secondary batteries has been increasing due to the increased use of portable electronics and electric vehicles, thus creating the need for cheaper and more reliable energy storage devices. Also, low-medium scaled power systems such as residential and aerospace applications have resulted in a rise in popularity of renewable energy systems, which require durable and reliable energy storage. Secondary cells consist of an anode (oxidized during a discharge), a cathode (reduced during a discharge), a separator (allows ions to flow through but is not electrically conductive) and an electrolyte (a medium that allows the ions to migrate between electrodes) [9]. An example of this in a Li-Ion battery is shown in Figure 2-1.

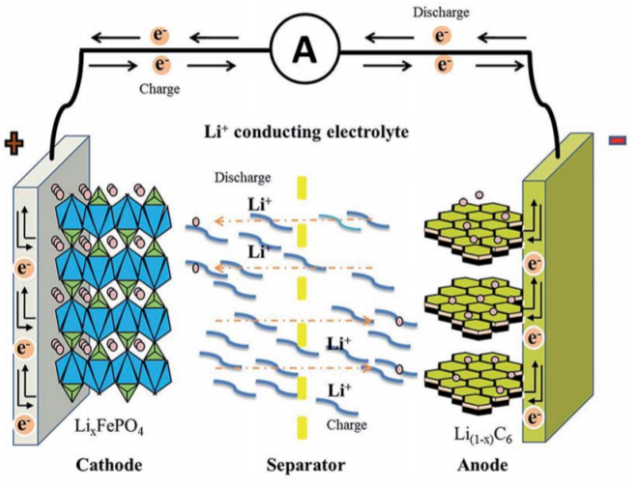


*Figure 2-1. Li-Ion Ion flow for discharging/charging* [10]

The main types of secondary battery chemistries that have a significant market share are broadly categorized in this thesis as Lead Acid, Li-Ion, Nickel based batteries and Sodium based batteries [1]. The secondary battery market is largely dominated by Li-ion batteries, followed by Lead Acid (LA) batteries. The major types of secondary batteries that are being used in the industry are further briefly discussed.

### *I. Lead Acid batteries*

LA batteries are mainly used for starter motors in combustion vehicles, however, they have found uses in renewable energy storage, emergency power systems and off grid storage. The popularity of these batteries stems from their low cost and ruggedness [1]. The negative electrode is constructed from lead (Pb). $Pb0_2$ is used as the positive electrode and it is bathed in a $H_2SO_4$ electrolyte (Figure 2-2).

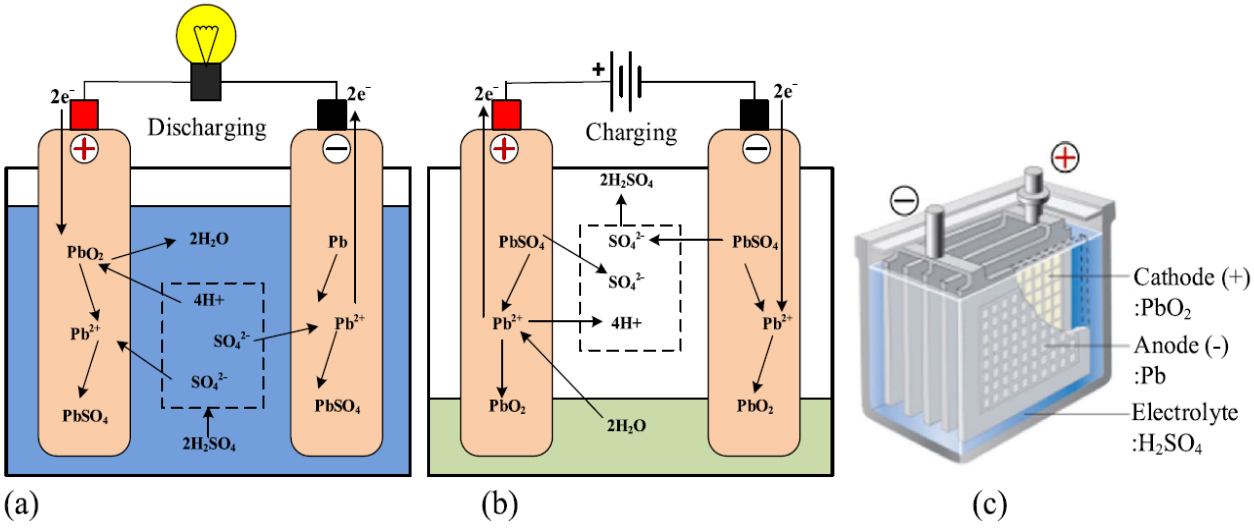


*Figure 2-2. Lead acid battery (a) discharging chemical processes (b) charging chemical processes (c)* [1]

The equation that governs this relationship is given by (2-1) below [1]. The equation shows that during a discharge, PbSO4 is produced while during charging water is produced. Lead acid batteries differ from other electrochemical devices as it does not have a separator between the anode and cathode.

$$Pb + 2\ PbO_2 + 2H_2SO_4 \rightarrow 2PbSO_4 + 2H_2O \quad (2\text{-}1)$$

### *II. Nickel-based batteries*

Nickel-based batteries consist of a positive electrode consisting of nickel hydroxide. The batteries are differentiated using different negative electrode materials. The negative electrodes can consist of iron (Ni-Fe), zinc (Ni-Zn), cadmium (Ni-Cd), metal hydride (Ni-MH) and hydrogen (Ni-$H_2$) [1]. The iron and zinc-based electrodes are not considered in this thesis due to their low specific power, high cost and low cycle life. Although the Ni-Cadmium battery has a good cycle life (>2000), good energy density it is highly toxic, expensive and suffers from the memory effect, therefore it is not a suitable candidate for EV applications. The Ni-$H_2$ battery has decent energy density and a good cycle rate but is very costly. The metal hydride-based battery has a good cycle life (>2000), decent energy density and a low memory effect. It is considered the best nickel-based battery for EV applications [1]. This Metal hydride battery was used in the Toyota RAV4 [11].

### *III. Sodium based batteries*

Sodium based batteries are largely classified into two categories, sodium-sulphur (Na-S) and sodium metal halide. Na-S was originally designed for EVs, but it became common for grid storage [1]. The battery has good energy and power density, great cycle life and high efficiencies, low cost as well as safe operation. The battery does require hot temperatures to operate as it uses a solid electrolyte that must be maintained in a molten state. The battery also suffers from high internal resistance. The NaS battery is shown in *Figure 2-3* (a). The second type of sodium-based batteries is the Zero Emission Battery Research Activity (ZEBRA). These batteries are a sodium-metal halide and are characterized by high energy density, good cycle life and lower cost. The main disadvantage of these cells is low specific power and self-discharge. [1]. The ZEBRA battery is shown in *Figure 2-3* (b).

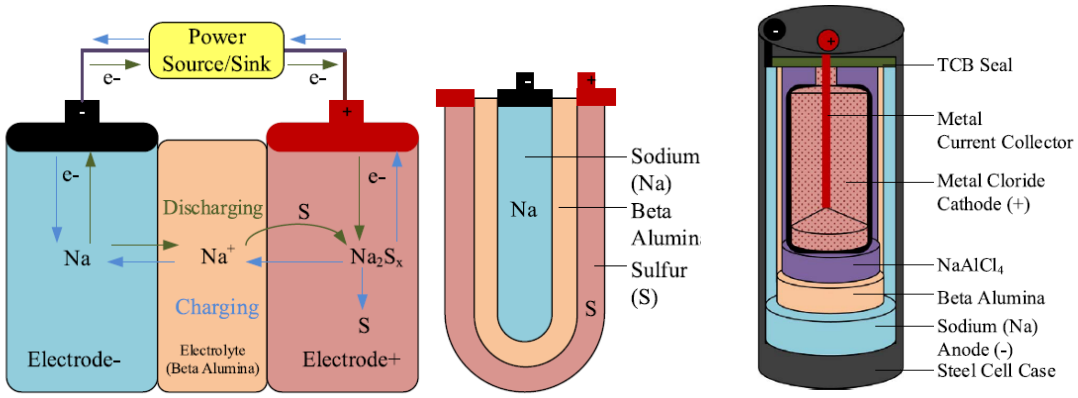


(a) (b)

*Figure 2-3. (a) NaS battery (b) ZEBRA battery* [1]

### *IV. Lithium Ion batteries*

Lithium based batteries are generally characterised by high specific power and energy, good energy density and do not suffer the memory effect. They generally fall into 2 categories, Lithium polymer (Li-poly) and Lithium Ion batteries (Li-Ion). Li-Ion batteries are generally more popular due to its low weight, small size, and high cell potential [1]. It already powers most laptops and smartphones as well as EVs [11]. The major benefits of Li-Ion battery technologies are a high cycle life, excellent coulombic efficiency, and low self-discharge [11]. The reaction in Li-Ion batteries differ from the normal battery "molecule to molecule" chemical reaction, Li-Ion transfers electrons by migrating back and forth in an "intercalation-based" reaction [11]. Referring to Figure 2-4, the green lines represent the flow of electron's and ions during a discharge and the purple lines shows the flow of electrons/ions during a charge.

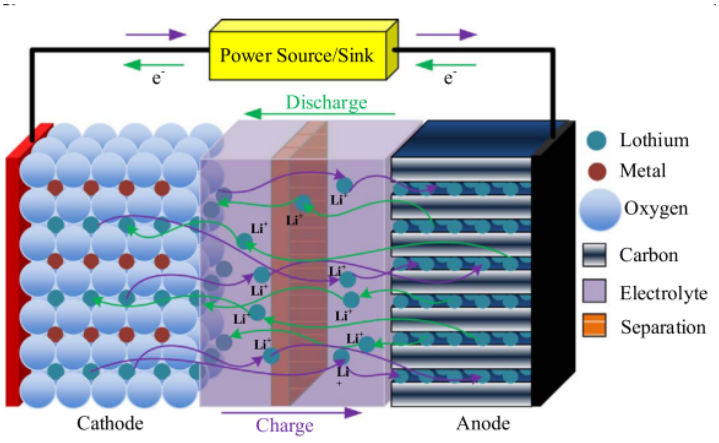


*Figure 2-4 Lithium-ion battery chemistry* [1]

Li-Ion differs from other Lithium based batteries by the fact that it does not make use of metallic lithium. There are several types of Li-Ion cells that are used, and they are generally differentiated by the chemistries of the cathode. Graphite is usually the material that is used in the anode [11].

The cathode usually consists of lithium and another metal. The major types of secondary Li-Ion cells are given below in Table 2.1 [11].

Table 2-1. Common Li-Ion cells

| Type | Chemical Formula | Common Name |
|---|---|---|
| Lithium Cobalt Oxide | $LiCoO_2$ | LCO |
| Lithium Manganese Oxide | $LiMn_2O_4$ | LMO |
| Lithium Iron-Phosphate | $LiFePO_4$ | LFP |
| Lithium Nickel Manganese Cobalt Oxide | $LiNiMnCoO_2$ | NMC |
| Lithium Nickel Cobalt Aluminium Oxide | $LiNiCoAlO_2$ | NCA |
| Lithium Titanate | $Li_4Ti_5O_{12}$ | LTO |

The chemical reaction of Li-Ion cells is given by (2-2) below. Where 'Me' represents 'Metal' and is any one of the Li-Ion chemistries mentioned above [1].

$$LiMeO_2 + C \leftrightarrow Li_{1-x}MeO_2 + Li_xC \tag{2-2}$$

Li-Ion also has a high voltage potential difference of between 3.2V and 3.8V. This gives the batteries very high energy and power densities [11]. Li-Ion NCA, NMC and LFP cell types are being extensively used in the EV industry [11].

### 2.1.2 Secondary Battery Comparison

The current research on batteries is focussed on reducing the cost, increasing specific energy and increase the number of cycles of use [11]. The U.S Advanced Battery Consortium (USABC) has created several standards that EV battery packs should meet by the year 2020. These are listed in Table 2-2. These values are used as a benchmark for the batteries discussed in the rest of this chapter.

*Table 2-2. USABC 2020 EV Battery Requirements [11]*

| Checkpoint | Value |
|---|---|
| Specific Power | 750 W/ Kg |
| Specific Energy | 350 Wh /Kg |
| Energy Density | 750 Wh/L |
| Cycle Life | 1000 cycles |
| Cost | 100 $/ kWh[1] |
| Self-Discharge | 0.03% /day |

[1] Dollars quoted in 2012

The batteries above were compared to the USABC 2020 EV battery requirements. The tables are split into 2 different tables, Table 2-3 and Table 2-4 which represent the worst and best performance given in literature based in the review by [11]. They are colour coded, based on their performance against the USABC requirements, with green representing values that are meeting or exceeding the requirement, moving towards red which are values that are far away from meeting the requirement. In both tables, the Li-Ion based batteries outperformed the other types of electrochemical cells in almost every category other than cost. The Li-Ion NMC and NCA chemistries had the best performance in most categories.

*Table 2-3 Battery performance based on literature (worst performing)* [11]

| | **Specific Power (W/ Kg)** | **Specific Energy (Wh /Kg)** | **Energy Density (Wh/L)** | **Cycle Life (cycles)** | **Cost ($/kWh)** | **Self-discharge (% /day)** |
|---|---|---|---|---|---|---|
| Lead Acid | 75 | 30 | 50 | 500 | 150 | 0.57 |
| Nickel Metal Hydride | 80 | 45 | 60 | 1200 | 250 | 1.43 |
| Zebra | 150 | 100 | 135 | 2500 | 200 | 15 |
| **Lithium** | | | | | | |
| LiFeP04 | 250 | 80 | 250 | 1000 | 600 | 1.29 |
| LiNiMnCo | 500 | 126 | 230 | 1200 | 600 | 0.71 |
| LiNiCoAl02 | 700 | 145 | 500 | 1000 | 600 | 0.57 |

*Table 2-4 Battery performance based on literature (best performing)* [11]

| | **Specific Power (W/ Kg)** | **Specific Energy (Wh /Kg)** | **Energy Density (Wh/L)** | **Cycle Life (cycles)** | **Cost ($/kWh)** | **Self-discharge (% /day)** |
|---|---|---|---|---|---|---|
| Lead Acid | 150 | 50 | 80 | 1000 | 100 | 0.29 |
| Nickel Metal Hydride | 400 | 80 | 150 | 2000 | 150 | 1 |
| Zebra | 200 | 120 | 200 | 2500 | 100 | 15 |
| **Lithium** | | | | | | |
| LiFeP04 | 1600 | 140 | 500 | 2000 | 300 | 0.1 |
| LiNiMnCo | 2400 | 210 | 550 | 1950 | 300 | 0.1 |
| LiNiCoAl02 | 800 | 240 | 670 | 1280 | 300 | 0.1 |

Li-Ion NMC type cells were chosen for research in this thesis. The following section investigates Li-Ion cells more in depth.

## 2.2 LITHIUM ION CHARACTERISTICS

The development of Li-Ion battery chemistries is targeted at maximizing energy density, increasing cycle life, and improving safety. Increase in its cycle life has not been a major issue since most consumer electronics have only a typical life requirement of 3 years. However, with the advent of EVs, life cycle rating has become a greater concern, because an EV manufacturer will generally favour a battery that has a high cycle life, over a battery with only high energy density [12]. The 2 best performing Li-Ion cells from the review conducted by [11] are shown in a spider diagram in Figure 2-5 [11] . The spider diagram compares the requirements of the USABC and the best and worst performing Li-Ion batteries in many categories. The figure shows that the requirements are not met in many areas.

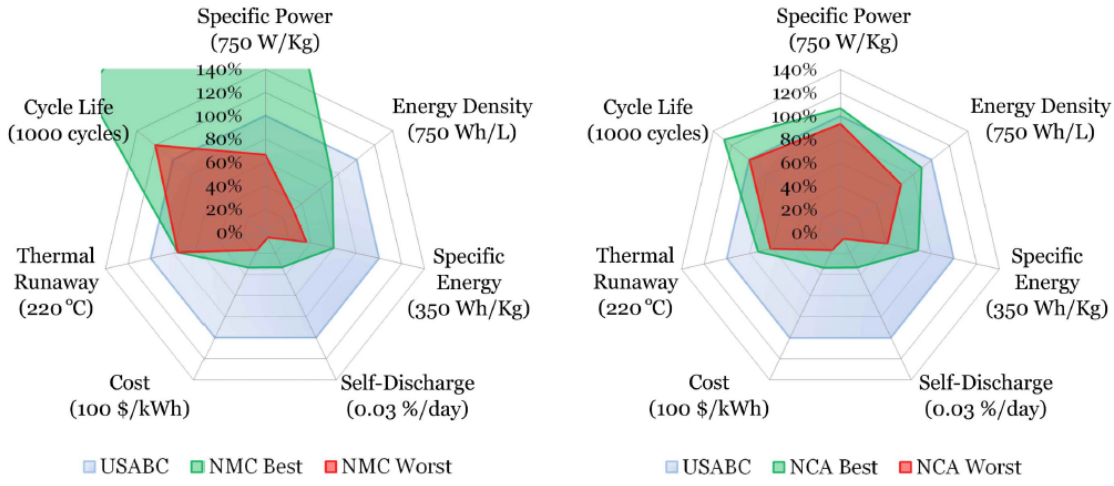


*Figure 2-5 Li-Ion performance comparison. (a) NMC (b) NCA* [11]

One other issue that Li-Ion batteries face is that, it requires protection against over-charge and over-discharge, since deep discharges shorten the life span and its performance is heavily affected by temperature [1]. If the battery is exposed to highly dynamic load profiles for a long-time frame, the cell can begin to degrade over time causing an increase in internal resistance and capacity fading [11].

### 2.2.1 Discharging and Charging Li-Ion cells

Li-Ion batteries are most commonly charged by the Constant Current/ Constant Voltage Method (CC/CV) method [13]. This is where the current is kept constant until a certain voltage threshold is achieved, then the voltage is kept constant until the current reaches a certain lower threshold. Figure 2-6 describes this process.

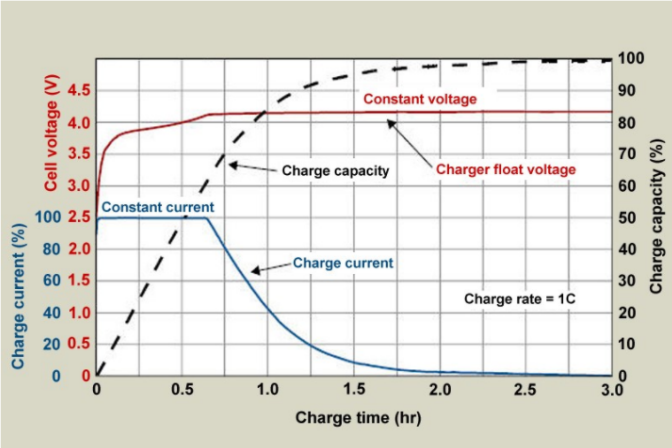


*Figure 2-6. CC/CV charging method for Li-Ion cells* [13]

The rate at which a Li-Ion cell can be charged and discharged is dependent on the chemistry of the cell. Table 2-5 shows the recommended discharging and charging current requirements in terms of C-rates as well as the nominal, minimum and maximum voltages of the different cell types. Most of the Li-Ion cells should be charged with a current of 0.7-1C and a maximum continuous discharge of 1C. Except for LTO and LFP, the Li-Ion cells have an operating voltage range of between 3 to 4.2 V.

*Table 2-5. Recommended Li-Ion Charging/Discharging [14]*

| Li-Ion Cell Type | Charging | Discharging | Nominal Voltage | Min Voltage | Max Voltage |
|---|---|---|---|---|---|
| LCO | 0.7-1C | 1C | 3.6 | 3 | 4.2 |
| LMO | 0.7-1C, max =3C | 1C, max = 10C | 3.7 | 3 | 4.2 |
| NMC | 0.7-1C | 1-2C | 3.6-3.7 | 3 | 4.2 |
| LFP | 1C | 1C, max = 25C | 3.20, 3.30 | 2.5 | 3.65 |
| LTO | 1C, max = 5C | 10C | 2.4 | 1.8 | 2.85 |
| NCA | 0.7C | 1C | 3.6 | 3 | 4.2 |

### 2.2.2 Degradation Mechanisms

Normally, the first part of a Li-Ion cell to degrade is the electrodes. The negative electrode in Li-Ion batteries are generally made of carbon (or graphite), silicone or titanate [15]. The main aging effect that occurs on the graphite electrode is the development of a Solid Electrolyte Interphase (SEI) layer [15]. As this layer develops over time, there is a loss of Li-Ions that can migrate across as well as a decomposition of electrolyte [15]. This layer consists of lithium oxide and lithium carbonate [12]. The more the cell is used, the larger this interface grows, and it can create a barrier that can completely obstruct interaction with the graphite [12].

The cathode also develops a layer that behaves similarly to the SEI layer, known as electrolyte oxidation [4]. This is mainly caused by high charging voltages. The SEI layers result in a higher resistance experienced by the cell. The SEI layers are shown in Figure 2-7 below. There is less alteration at the positive electrode, however, there is a small SEI layer that forms over time [15].

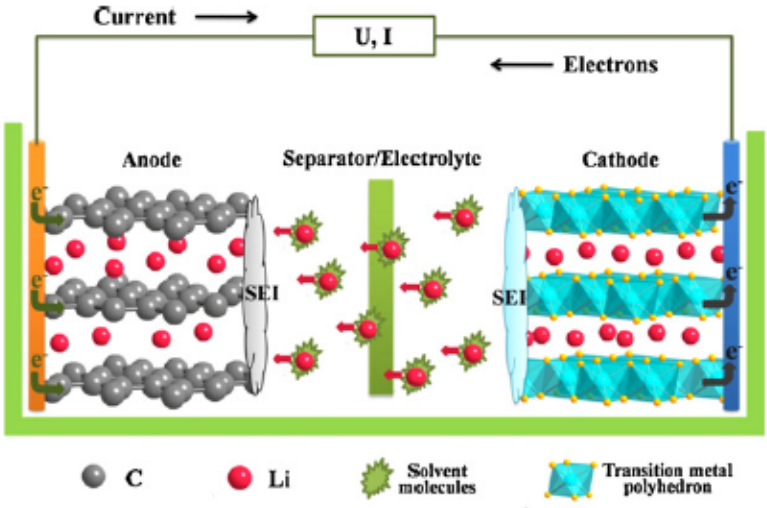


*Figure 2-7 SEI layer* [16]

Battery aging impacts the Li-Ion cells in 2 major ways; the first is capacity fade, which is a loss of the capacity of the cell, while the second is a rise in internal impedance [15]. These performance losses are a result of physical mechanisms which are mainly influenced by the materials of the electrodes [15]. These mechanisms of degradation can be chemical or mechanical in nature. It is important to monitor how the battery degrades over time. The next section investigates how the States of the battery system is obtained.

## 2.3 BATTERY STATES AND MODELS

There has been extensive research into characterizing cells at a particular point in time. This can be inherent characteristics such as the operating/charging voltage due to the chemistry or operating state characteristics such as the battery's State of Charge and available power at a time. There is a variety of information that is useful to know about in predicting its performance and operation. Regardless of the information specified by the battery's manufacturer, a battery changes over time due to degradation and operating conditions and it is important to understand how the parameters of the battery will change, so that its performance can be optimized. This is not trivial, as a battery behaves non-linearly due to complex internal electrochemical processes as well as external operating conditions, thus, monitoring of the battery states can pose a challenging task. The most important states to monitor for the continued operation of the secondary battery are listed below [17].

1. Capacity - The capacity of the cell is the amount of energy that can be stored. It is measured in Amp hours (Ah)
2. State of Charge (SoC) – The SOC is simply the relationship between the battery capacity at a given state ($C_r$) and its total capacity ($C_{bat}$). This relationship is given by the following equation:

$$SoC = \frac{C_r}{C_{bat}} \times 100\% \tag{2-3}$$

3. State of Function (SoF) – This state represents the battery's capability to perform a task. i.e. to deliver a certain amount of energy over a certain time frame. Prediction of available power at a given time would fall into this state. This state is very dependent on the internal impedance of the battery.
4. State of Health (SoH) – This state is directly related to the capacity and it is used as an indicator of how much a battery has deteriorated during its life time. As a battery decreases, its ability to deliver power as well as capacity decreases. Reference [18] states that the relationship between SoH is given by the ratio of the current capacity to the capacity of the battery when it was new. This is shown in the following equation.

$$SoH = \frac{C_{bat}}{C_{new}} \times 100\% \tag{2-4}$$

5. Remaining Useful Life (RUL) – This gives a prediction of how much time or cycles the battery has left before it is no longer useful for the application.

These states are not directly measurable and thus other parameters such as voltage, current, impedance and temperature are used to estimate these states. To estimate the states from the directly measurable parameters, it is important that a proper model is defined for the electrochemical system. Modelling of the battery broadly fall into 3 categories. electrochemical models, mathematical models and electrical models [19]. Mathematical battery models are usually analytical models that consist of many equations that describe properties of the battery. Electrochemical models use physics-based methods to describe the internal electrochemical processes of the battery. These models are made up of differential equations and are the most accurate [20]. These 2 types of models can be computationally expensive and thus this thesis focusses on the use of electrical models often referred to as Equivalent Electrical Circuit (EEC). An EEC is a type of electrical model that is used to determine the battery states using passive electronic components representation for parameter estimation. Solving these models can be done using microcontrollers thus, enable accessibility of results in real time [20]. To optimize accuracy and complexity of the model, EEC models are being used to model parameters online [20].

EECs make use of circuit elements such as resistors, voltage sources, capacitors and inductors. Because of their ease of use they have been extensively applied to batteries in the EV space. The simplest form of an EEC is the internal resistance model, as shown in Figure 2-8 (a) [20]. It simply models the battery as a dc voltage source and a resistor. The Thevenin model in (b) expands on this by adding a RC element to represent the polarization of the battery which is observed as an exponential decay in transients [20]. The RC element represents the charge transfer effect.

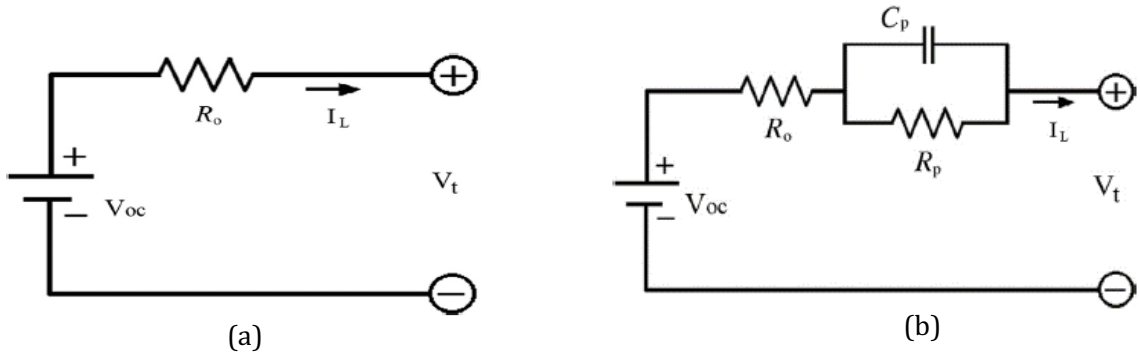


*Figure 2-8. (a) Internal Resistance Model (b) Thevenin Model* [20]

Although there are numerous variations of the EEC model, these two represent the most basic structures for a battery. After an appropriate EEC model is selected, tests should be

conducted on the battery to fit parameters to the model. These tests will be discussed in the next section.

## 2.4 BATTERY TESTING TECHNIQUES

There are a variety of battery testing methods that are used to determine the battery states. This section investigates a few of the most common techniques found in literature.

### 2.4.1 Static Capacity Test

The static capacity test is an offline test that measures the total capacity of a cell. The procedure involves discharging the cell from a fully charged state until the voltage drops below a minimum threshold. The static capacity test was carried out in [19] during charging and discharging on LFP types cells. Figure 2-9 shows the results of a capacity test that was performed by [19] on a LFP type cell. This illustrates the non-linear relationship between capacity/SoC and the voltage of the cell. The total capacity of a cell is specified by the manufacturer, however, this changes over time due to operating conditions such as temperature and discharge rate. The overall capacity of the battery is dependent on factors such as cell temperature, the load current and aging [19].

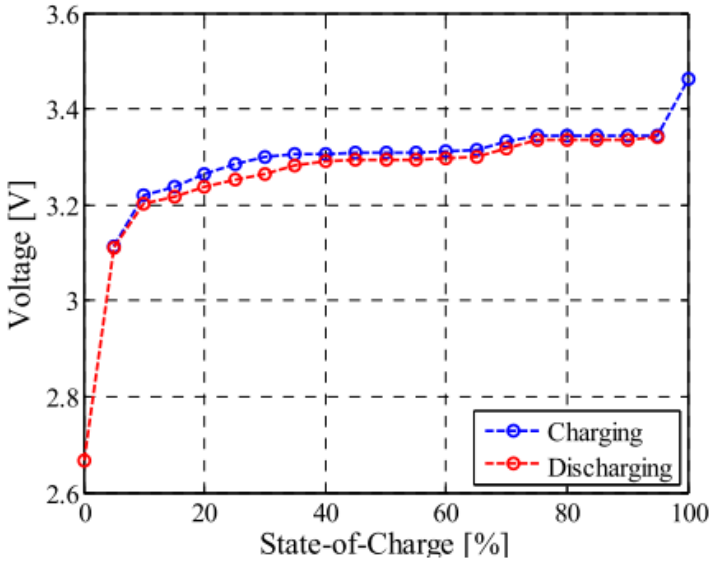


*Figure 2-9. Static Capacity Test* [19]

### 2.4.2 Open Circuit Voltage SoC estimation Method

Determining a battery's SoC is critical in most applications, as it is important to know how much more energy the battery system can still deliver before a recharge is required. The SoC is analogous to the fuel gauge in a vehicle [21]. It is a non-trivial task as batteries are non-linear and have time-varying features, which make SoC not directly observable.

A common method to determine the SoC of a battery system, is to infer the SoC from the Open Circuit Voltage (OCV). If there is knowledge of the relationship between the OCV curve and SoC, the SoC can be determined at any given time by looking up the value of SoC for a OCV [21]. This is a very simple method that has high accuracy however, it has a major draw-back in that the battery must rest for a long time before the OCV can be measured accurately[21]. For a LFP cell at low temperature, this can take up to 2 hours, making it only practical to measure after the system is offline for a significant amount of time [21]. Some literature suggests that a settling time of at least 2 – 6 hours should be allowed after usage for accurate measurement [22]. The Electromotive Force (EMF) method is used to solve the issue with OCV estimation by observing the relaxation time of the OCV method and predicting the OCV by measuring the voltage at any point in operation [21]. This is shown in Figure 2-10.

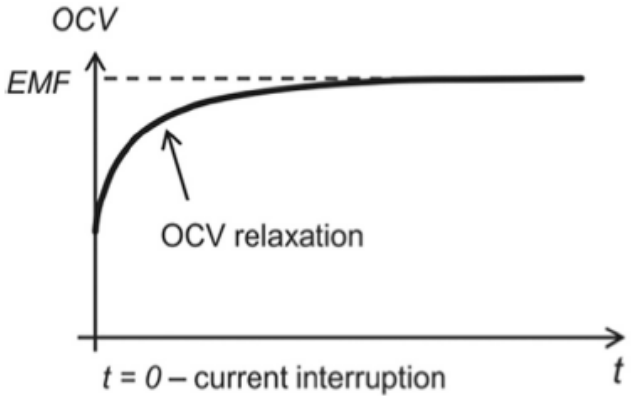


*Figure 2-10. OCV relaxation after current interrupt* [21]

### 2.4.3 Coulomb Counting

Coulomb counting is regarded as the simplest method to estimate the SoC of a battery system. It has a major benefit of being computationally simple for a microcontroller [21]. It works by integrating the current of a battery over a particular time frame during a charge or discharge of the battery [21]. The equation is given below,[2] and $C_n$ is the nominal capacity.

$$SoC = 1 - \frac{\int i \ dt}{C_n} \tag{2-5}$$

Coulomb counting involves measuring the output current of the battery and by using prior knowledge of the battery's capacity, estimates the SoC by subtracting the amount of current measured from the previous known SoC [21]. It is also an open-loop algorithm, therefore any

[2] As mentioned above this is not the only definition of SoC, however, this is one of the most popular ones that is used in literature.

inaccuracies in measurement result in an accumulative inaccuracy over time. Coulomb counting assumes nominal temperature without compensating any variations in temperature or system disturbances [21] [23].

### 2.4.4 Impedance Testing Methods for Battery Characterization

Impedance is an important parameter as it is directly related to the power capability of the cell, and therefore the SoF [19]. Impedance is often used to obtain a model of the electrochemical systems. Impedance is not a directly measurable characteristic of the battery and must be estimated by other means (i.e. from voltage and current measurements). The impedance of electrochemical systems, however, demonstrates a non-linear behaviour as it is dependent on the SoH, temperature and the discharge rate of the cell [19]. There are a variety of tests that are used to classify the impedance at various operating points. The impedance of a cell can be used to obtain other state information. Using impedance, it is possible to detect faults in the battery packs, as well as determine the SoC and SoH [24]. The ability of batteries to deliver high current from a "cold" state is directly related to the impedance [24]. Assuming the system is operating within a linear region, the response of a cell to a current input $i(t)$ can be simplified as shown in Figure 2-11 from reference [24].

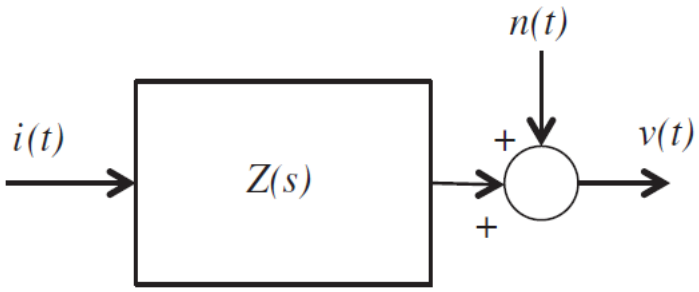


*Figure 2-11. Transfer function of the impedance of a battery/cell* [24]

It is very important that the disturbance signal $i(t)$ is chosen correctly to fully characterise the system. In general, when performing impedance measurements on electrochemical cells, the input signal is a current signal, and the response is voltage. The simplest parameter that can be derived from the pulse test is the DC resistance. By measuring the change in voltage of the cell, and the change in current, the DC resistance can be calculated by (2-6) below.

$$R_i = \frac{\Delta V_i}{\Delta I_i} \tag{2-6}$$

This DC pulse method can be adapted slightly by measuring the transient decay of the applied step. This is where a load discharge current is applied to a battery for a period, and then

stopped. The test can also be applied to a regenerative charging current pulse. Most battery test stations can perform variations of step responses or current interrupt tests Figure 2-12 below shows how the cell voltage changes with a current step [19].

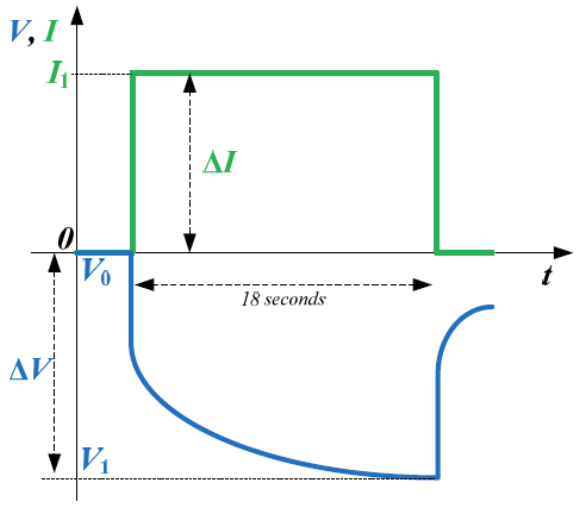


*Figure 2-12. Step test* [19]

This response has a very similar response to that of a resistor capacitive (RC) decay. Therefore, a common circuit that is used to classify this transient response is a Thevenin circuit which is a model made up of a series resistance and several parallel RC branches. A disadvantage of this technique is that the parameters that are determined with this technique do not provide sufficient physiochemical information, however it is still useful to obtain a simple model of the battery [19].

The voltage relaxation time can be used to estimate the EEC parameters such at equivalent resistance and capacitance. The step response procedure functions in an analogous way by stepping the currents between DC setpoints. The DC pulse test works by applying a DC current to the battery and measuring the voltage response of the battery [19]. The current interrupt is similar, and the procedure is as follows. The cell should be operating at a steady state condition. At a time $T_1$, the load should be disconnected from the battery. Reference [25] mentions 3 ways in which to find the transient response of an electrochemical cell.

1. Remove load resistor ($R_L$) – Current interrupt
2. Apply a load $R_L$ to a cell at rest – Start Current
3. Changing load current from $I_1$ *to* $I_2$– Step response

Reference [24] mentions that step responses have a disadvantage that for a decent Signal to Noise Ratio (SNR) of the measured signal, large inputs currents are required which results in non-linear behaviour. Reference [24] also states that their method can be applied to series connected cells, as the cell voltages are measured across each cell. It is not possible however to decouple cell voltage measurements if the cells are connected in parallel, but an average impedance can be assumed.

### 2.4.5 Electrochemical Impedance Spectroscopy (EIS)

Electrochemical Impedance Spectroscopy (EIS) is a method of characterizing the battery's impedance at various frequencies. The impedance at 1kHz is often specified by the manufacturer of the battery, EIS expands on this by calculating impedance over a range of frequencies. EIS is a method which applies a sinusoidal current or voltage to a cell and records its response which is a sinusoid of an amplitude as well as phase shift [3].

EIS techniques have been extensively researched in literature, and it has been found to be a useful tool for measuring the SoH, SoC and SoF of electrochemical cells. There are generally 2 ways that EIS is applied to electrochemical systems, galvano-static and potentio-static mode. In galvano-static mode, a current signal is injected, and the voltage response is measured. In potentio-static mode, a voltage perturbation signal is used, and the current response is measured. Galvano-static mode is more commonly used in for electrochemical systems. If we assume that an Li-Ion cell can be represented by its OCV potential and an impedance $Z_{battery}$ , the EIS measurement can be simplified to Figure 2-13 below.

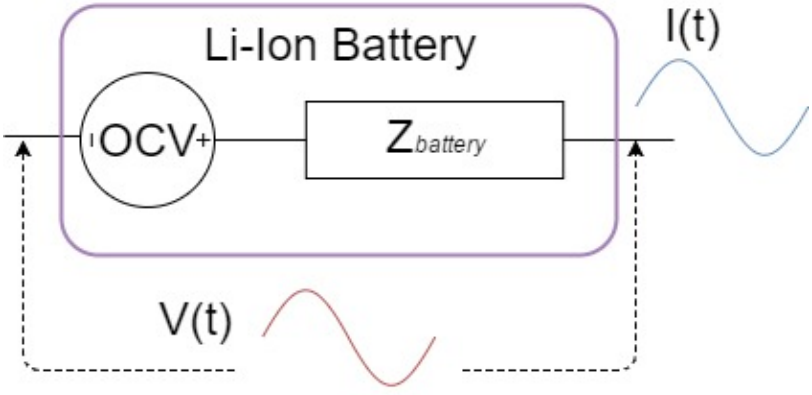


*Figure 2-13. Simplified linear representation of an EIS measurement with a sinusoidal current injection and voltage response*

The current and voltage is given by the equations below. The current sinusoid perturbation (2-7) will result in a voltage sinusoid response with an amplitude and phase shift (2-8). The impedance is then calculated using (2-9).

$$I(t)_{Injected} = I_{pp}\, sin(\omega t) \tag{2-7}$$

$$V(t)_{Response} = V_{pp}\, sin(\omega t - \emptyset) \tag{2-8}$$

$$Z(\omega t) = \frac{V(t)_{Response}}{I(t)_{Injected}} \tag{2-9}$$

The obtained impedance response from an EIS test is resolved using a Nyquist plot which is then used to obtain a model of the cell. Figure 2-14 shows a simplified Nyquist plot from an EIS measurement of a Li-Ion cell. The internal electrochemical reactions for a Li-Ion cell are the ohmic loss, charge transfer loss and the diffusion loss [26]. The ohmic effect is the part where the impedance crosses the real axis. This represents the ohmic resistances of the battery contacts and electrolyte. The charge transfer effect is shown by the large semi-circle region in the high frequency region [26]. This represents the positive Li+ transfer through the film interface [27]. The diffusion effect is shown by the straight line at a slope, in the low-frequency region [26]. It is shown on the diagram that the diffusion process occurs where frequencies are less than $1Hz$. The charge transfer effect occurs at middle range frequencies while the conduction effect occurs at high frequencies.

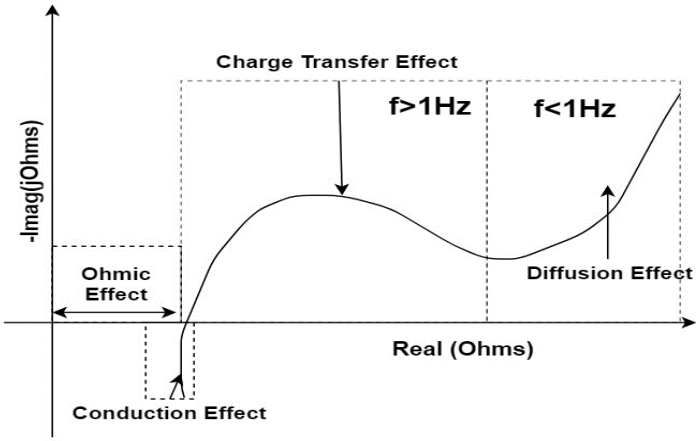


*Figure 2-14. Simplified Nyquist plot of an EIS measurement of a Li-Ion cell*

It is important that the selection of frequencies for EIS is adequate to produce a Nyquist plot that fully represents the characteristics of the cell at different operating conditions. The goal is to obtain the maximum information from the cell with the least amount of frequencies.

## 2.5 ELECTRICAL EQUIVALENT CIRCUITS FOR EIS MEASUREMENT

Obtaining an EEC starts by analysing the Nyquist plot, and determining the combination of circuit elements that would produce a similar voltage response, while considering the basic electrochemical reactions that occurs in the battery cells. The shape of the Nyquist plot can be used to produce an equivalent circuit that would yield a similar shape if those frequencies were applied to it. Various impedance models can be used, depending on how close the electrical elements can get to represent the impedance of the battery.

Figure 2-15 shows how each section of the Nyquist plot was modelled by reference [26]. The circuit element models from (a) – (d) do not fully represent the electrical response of the cell, thus reference [26] needed to introduce a new type of element to fully map the diffusion region which is shown by the straight line in the Nyquist plot. In literature, there are generally 2 components that represent this region. The Warburg element, and the Constant Phase Element (CPE).

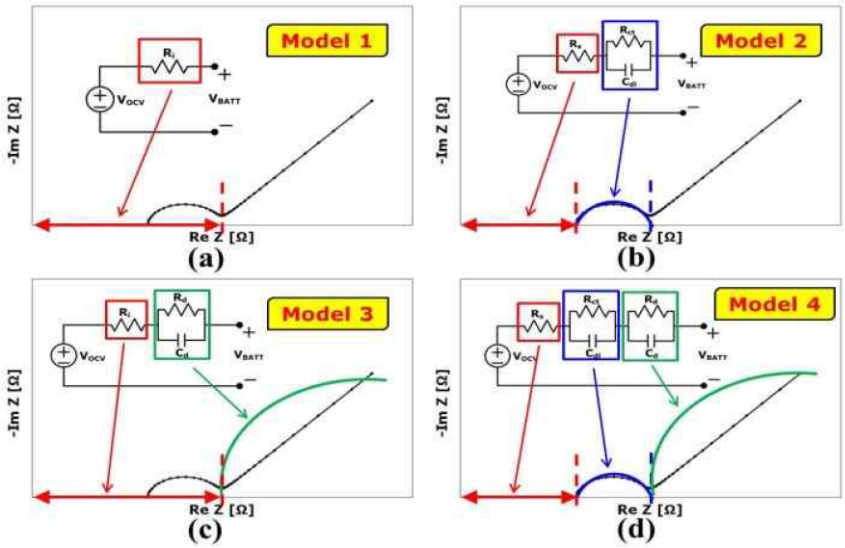


*Figure 2-15. EEC Modelling using Nyquist plot* [26]

The Warburg Element is a circuit component that has a response of a 45-degree slope on the Nyquist plot. A Constant Phase Element (CPE) is very similar, however, it can have a slope between 0 and 90 degrees. This is illustrated in Figure 2-16.

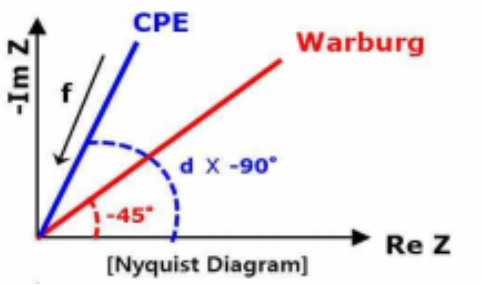


*Figure 2-16. Difference between Warburg Element and CPE* [26]

The most common EEC that is used for electrochemical systems is Randles circuit. This considers the diffusion effect that occurs in the battery. Reference [18] used this model to represent a lead acid battery.

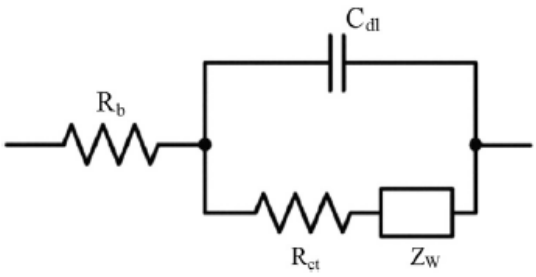


*Figure 2-17. Randles Circuit* [20]

A typical EEC for a Li-Ion cell consists of an inductor L, a pure ohmic resistance $R_s$, a double - layer capacitance of $C_{dl}$, charge transfer resistance $R_{ct}$ and a diffusion element (Warburg) $Z_w$ [28]. Simpler battery models are also used. An example of this is the use of the Thevenin EEC circuit as done by [23]. Another circuit proposed by [24] for LFP cells is shown in Figure 2-18. This circuit contains 2 CPE elements and a Warburg element.

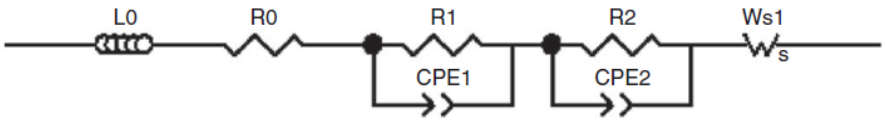


*Figure 2-18. EEC for LFP cell* [24]

Parameters are extracted from the Nyquist plot by using a non-linear least squares algorithm at different states of system operation [21], [29]. In some EIS procedures, a reference electrode is inserted into the cell so that the impedance contributions of the anode and cathode can be assessed separately [30]. Due to this being very invasive and damaging to the battery system, this will not be considered as part of this work.

## 2.6 STATE INFORMATION FROM IMPEDANCE TESTING

The aim of impedance testing is to obtain information about the state of the battery system. The following are examples from literature on how batteries can be characterized by impedance measurements.

### 2.6.1 SoC

Traditional SoC measuring techniques such as coulomb counting and OCV estimation are commonly used, and have issues associated with them as mentioned in Section 2.4. Referring to Figure 2-19 below, SoC can easily be estimated by using the impedance spectra of the Nyquist plot [24]. There is a general trend that shifts the spectra to the upper right side. [31] was able to determine the SoC of Lead Acid batteries accurately using this approach.

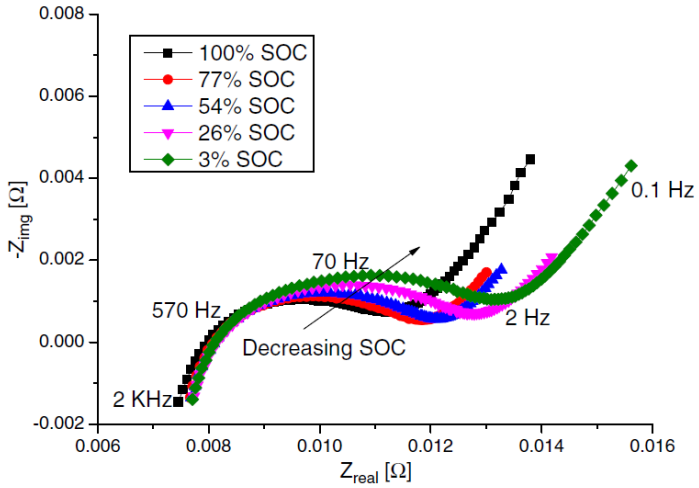


*Figure 2-19. Impedance variation of a LFP cell with SoC* [24]

[23] also showed that the OCV voltage could be estimated accurately if the impedance is known using equation (2-10). This is useful if OCV lookup tables are used to determine the SoC. By knowing the impedance $z_{bat}$ and measuring the battery voltage and current, OCV can be determined and SoC can be calculated using a lookup table. This implies that the battery does need to rest before SoC can be measured.

$$OCV_{est} = V_{battery\_dc} + I_{battery\_dc} \times |z_{battery}| \tag{2-10}$$

### 2.6.2 State of Health

Impedance of a Li-Ion battery increases with age. The measured impedance can be compared against the impedance of the cell when it was new, or other benchmarked data sets. Figure 2-20 shows how the impedance differs for a battery at the Beginning of Life (BOL) and a battery at the End of Life (EOL). There is a general shift to the right in the Nyquist plot as the battery ages, which is consistent between the different cells that were measured. EIS can observe this trend and estimate the SoH based on the Nyquist plot [32].

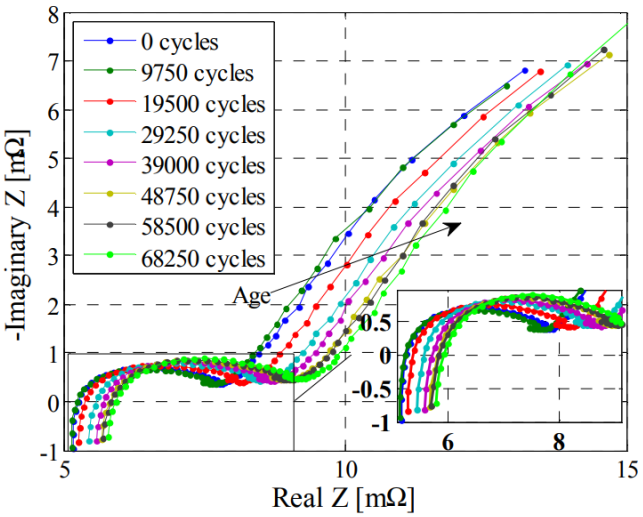


*Figure 2-20. Measured Impedance at BOL and EOL* [32]

## 2.7 TESTING CONSIDERATIONS FOR EIS MEASUREMENTS

There are issues with simplifying the battery to a purely impedance model as was done in Figure 2-13. Firstly, electrochemical systems such as Li-Ion cells do not behave linearly. Impedance is only defined for a linear system. The impedance is also a function of other states of the battery such as the SoC, SoH operating temperature and discharge current. For an impedance measurement to be conducted, the system must be approximated as being linear and time invariant (LTI) [33].

For an electrochemical system, an EIS measurement is usually conducted in galvano-static mode. The choice of the DC bias that the perturbation signal will be superimposed onto is important to ensure linearity. A Li-Ion battery is a non-linear system, however if operated within certain limits, it can be assumed to be linear. This is illustrated in Figure 2-21 below. The current-voltage relationship can be seen to be non-linear. However, at the zoomed in portion of the graph, the relationship can be considered pseudo-linear. For a system to be

considered linear, the following should apply: The response to an input $x(t)_1 + x(t)_2$ is equal to $y(t)_1 + y(t)_2$ ; and the response to the input $ax(t)$ is equal to a $ay(t)$.

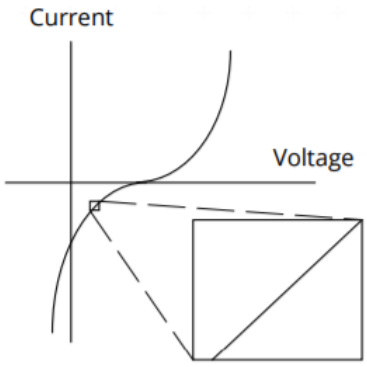


*Figure 2-21. Diagram showing Pseudo Linearity* [34]

An EIS measurement should only be conducted in a region of linearity. Therefore, measurement should be done by small excitation signals on a fixed operating point [18]. The excitation current $I_{bat(\mathrm{f})}$ and voltage response $V_{bat(\mathrm{f})}$ should be much smaller in amplitude in comparison to the mean voltage and current values [18]. There are 3 conditions that should be met for a EIS measurement to be valid. These are causality, stability and linearity as required for the Kramers-Kronig relationship [5] [35]. For this to be met, the following requirements should be met to achieve a useful EIS plot:

- The inner resistance of the cells acts linearly at the point of measurement [33].
- The current should also be kept constant during the entire measurement and the excitation signals should be done around a fixed operating point and be small in magnitude [18].
- Temperature remains constant. Temperature is a major factor that influences how accurate a EIS measurement will be [23].
- Ensuring a sufficiently fast measurement so that time invariance can be assumed and that the SoC of the cell does not change significantly during measurement [24] [33].
- The amplitudes of the injected signal are large enough to achieve a good SNR and measurement accuracy, without putting the cell in a non-linear mode of operation [24].

There are also other practical issues such as the measurement of the actual voltage and current. [24] states that obtaining impedance of high power cells is challenging because of its low resistive values, therefore the voltage response is in the order of a few milliohm/ micro-ohms. In general, the larger the amplitude of the injected signal, the greater the response and

SNR obtained [5]. This therefore represents a trade-off between measurement accuracy and linearity. This trade-off was investigated by [35] and it was found that if an EIS measurement perturbation operates outside its linear region, it will result in non-fundamental harmonics in the frequency domain. This lends itself to the idea that the perturbation signals must be small in magnitude to remain within a linear region. This however is problematic as the response signal is often quite small and there is a large amount of noise present in the system which results in a small SNR for the measurement. For instance, the Li-Ion NCM battery that is investigated in this thesis, has an internal impedance of about $3mOhm$ at $1kHz$. If a $100mA$ perturbation current is applied, this will result in a voltage response of $300\mu V$. This is a small value to be measured accurately and can lead to measurement errors [35]. There is thus a trade-off between having a decent SNR for a measurement and ensuring linearity [35]. Reference [35] defines the optimum perturbation of a system to be:

*"the maximum perturbation amplitude that ensures a linear response to the system"*

This optimal perturbation across different frequencies was obtained by measuring the Total Harmonic Distortion (THD) associated with the measurement. If the system is behaving non-linearly to a sinusoidal frequency, this will result in a superposition of the fundamental frequency and non-fundamental frequency components. The THD measures the amount of non-fundamental frequencies in the response. The following equation represents the THD for a signal $X$ [35].

$$THDX = \frac{1}{ABS(\hat{X}_1)} \sqrt{\sum_{i=2}^{\infty} \hat{X}_i^{\,2}} \tag{2-11}$$

Where $\hat{X}$ is the Fourier transform of the signal $X$. [35] applied this technique to a fuel cell system in galvano-static mode. A FFT was applied to the voltage response signal and the harmonic distortion was calculated for each individual applied frequency. It was found that an increase in the amplitude of the perturbation signal increased the SNR therefore decreasing the THD of the response, however, if the increase in amplitude was too large, more harmonics were generated thereby increasing the THD. This relationship is shown in Figure 2-22.

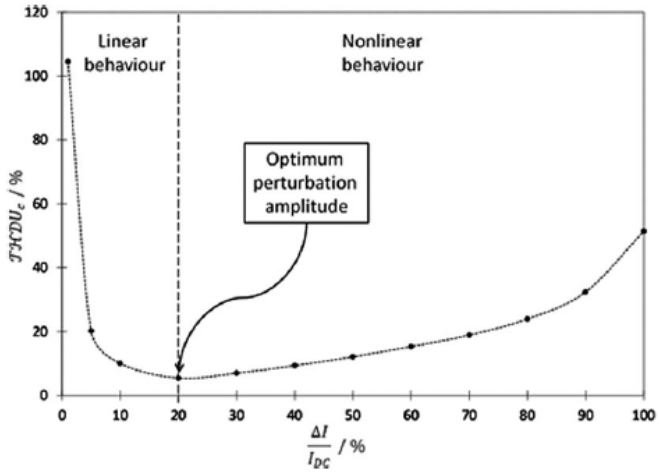


*Figure 2-22. Example of a fuel cell experiment to find optimal perturbation amplitude* [35]

Another aspect that should be accounted for is the size of the DC current on which the perturbation signal is superimposed. EIS measurements are dependent on the offset DC current used in the measurements. It was shown by [23], that the impedance for the same SoC differs for different discharge currents. Considering Figure 2-23 , the impedance at 1kHz changes for different C rates (discharge rates).

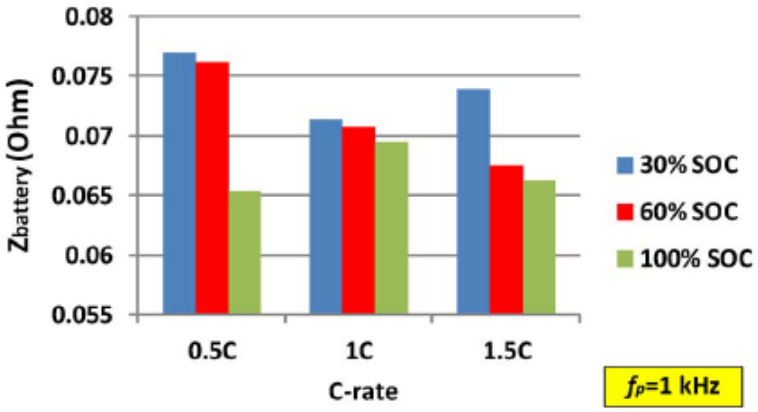


*Figure 2-23. Relationship between impedance and discharge rate* [23].

This section investigated the measurement considerations required to perform an accurate EIS measurement. The next section expands on the use of EIS by discussing the more advanced ways that it can be applied to a system.

## 2.8 ADVANCED EIS TECHNIQUES

The previous chapter showed how EIS is generally applied to a system. Conventionally, EIS is applied to a cell using standard FRAs for accuracy and precision in measurement, while the cell is not connected to a running system (i.e. the cell is not under real-time operation). This poses a limitation to real time condition monitoring of a battery, since the battery must be taken out of operation for the impedance variation to be determined. Another issue with the general EIS approach is that, it takes long to perform as each perturbation sinusoid is injected and measured separately. This results in a lengthy testing time, which limits the use of EIS for online systems as it is impractical for many applications. This section investigates the implementation of broadband signals and various converter topologies as found in literature, to address the issues associated with implementing Impedance Spectroscopy in situ.

## 2.9 BROADBAND IMPEDANCE SPECTROSCOPY

As previously discussed, the major disadvantage of conventional EIS is that it takes long to perform, especially if many of the frequencies of interest are in the sub-hertz range. This becomes a challenge for in situ condition monitoring, as there may be a major difference in operating conditions between the first and last measurement; specifically, in terms of changes which may have occurred in the SoC, operating temperature and DC current. If the battery is charging/discharging with a high C rate, the 'state' will vary too much over an EIS measurement, making the results invalid. Broadband Impedance Spectroscopy (BIS) is referred to as the use of broadband signals, which contain multiple frequency components for an Impedance Spectroscopy (IS) procedure. This reduces overall measurement times as the multiple frequency responses of the battery is measured in the same time frame instead of one after each other. The most common broadband signals that have been used on electrochemical devices are:

- Multi-sine
- Chirp (Swept Sine)
- Swept Square
- Random white noise and Pseudo Random Binary Sequences [36]

Each of these BIS signals have differences which make them suitable for different test applications in IS. The Swept sine or Chirp signal, is a sinusoidal signal whose frequencies vary with time. This produces a near flat amplitude spectrum over the frequencies of interest. Both Swept sine and Swept square signals, use a square wave instead of a sinusoidal wave as demonstrated in [36].

BIS measurements have also been done by using naturally present noise in the system to determine the impedance of lead acid batteries, but it requires a standard laboratory impedance analyser [24] for accuracy. Pseudo Random Binary Sequence (PRBS) can be considered as an approximate for band limited white noise. It was implemented and compared to the multi-sine in [24] using a motor controller to perform the BIS measurements. Figure 2-24 shows the comparison of the multi-sine (a) and the PRBS (b) results compared to a standard FRA. The figure compares the amplitude and phase. It was shown that the multi-sine approach gives more accurate results compared to the PRBS noise approach due to the higher signal-to-noise ratio achievable using the multi-sine.

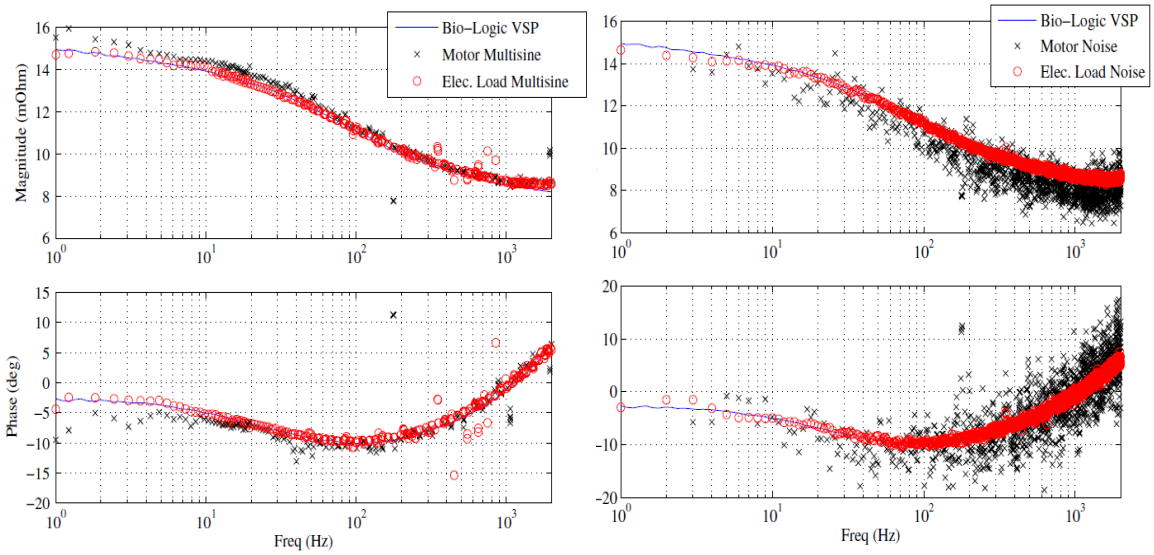


(a) (b)

*Figure 2-24 Comparison of Multi-Sine Signals and PRBS Signals* [24]

Multi-sine BIS signals are designed by summing different sinusoidal signals. Multi-sine signals have been used at length for bio-medical studies, and only in recent years have been applied to electrochemical systems [3]. The equation below from [3] and [24] describes how a multi-sine signal is created. The equation contains 3 variables, the amplitude matrix $a_n$, frequency matrix $f_n$, and phase matrix $\theta_n$ which specify the parameters of each sine that is being summed.

$$I_{BIS}(t) = \sum_{n}^{N-1} a_n \, sin(2\pi f_n + \theta_n) \qquad (2\text{-}12)$$

An example of a multi-sine current signal and voltage response is given in Figure 2-25 below. By applying a Fast Fourier Transform (FFT) to both the current perturbation and voltage response, the impedance at each frequency can be calculated.

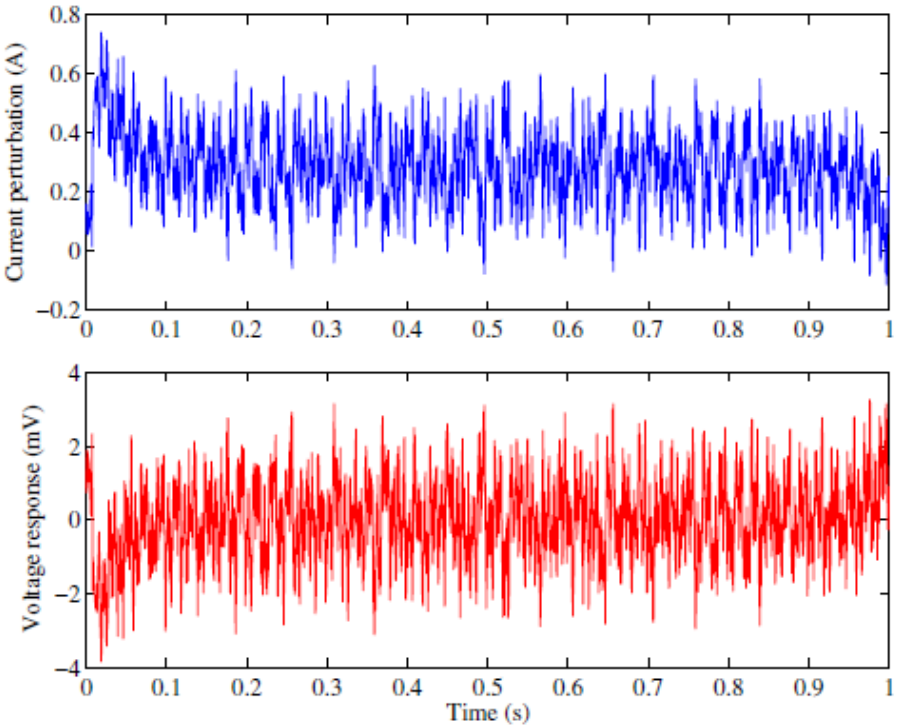


*Figure 2-25 Multi-sine current signal and voltage response* [24].

Multi-sine signals reduce the time issue associated with EIS at an expense of a larger perturbation signal and therefore larger disturbance.

## 2.10 ONLINE BATTERY MONITORING USING IMPEDANCE SPECTROSCOPY

The aim of this dissertation is to perform impedance spectroscopy measurements without disconnecting the battery from the system or interrupting the system operation. This will enable the Battery Management System (BMS) to use the results from the online impedance measurements to determine the state of the battery in situ and adapt the battery power management system accordingly. If batteries fail, information from EIS measurements can be obtained to determine the failure patterns [33] and cause of the failure. For example, battery aging can also be monitored by looking at the changes in the model parameters.

Online EIS can either be implemented using linear amplifiers for injecting the AC perturbations or using the associated power converter that interfaces the battery and the load to inject signals via duty cycle perturbations. These methods are illustrated by [23] as shown in Figure 2-26 with (a) showing the EIS via linear amplifier injection and (b) showing EIS by duty cycle perturbation.

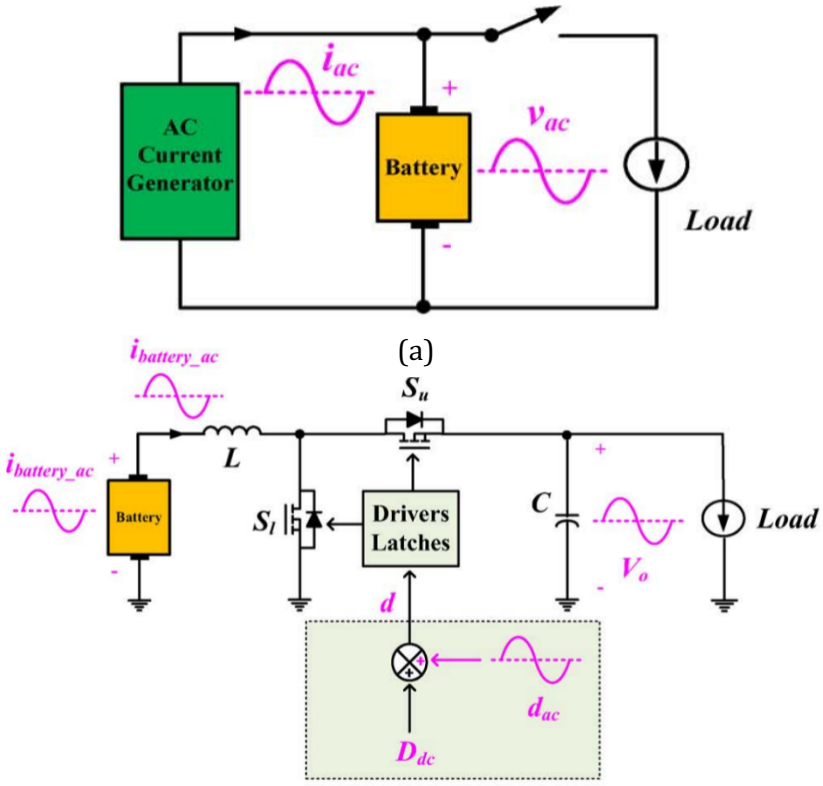


*Figure 2-26. (a) Linear EIS injection (b) EIS on a power converter* [23]

Linear amplifiers are often used in a test bench set up using a potentio-stat/galvano-stat and FRA. They can be implemented online by including additional signal amplification circuitry

into the BMS so that the current signal is injected into the battery directly. A voltage controlled load can also be used to inject the signal as was done in [3] and [5], this however can only inject the signal while the battery is discharging.

A major disadvantage of using a linear signal amplifier is that depending on the size of the battery bank, also the power required by the linear amplifier to produce the current stimuli can be very large [33]. This requires additional large circuitry to be included online and can have high power loss due to heat in the linear amplifier. This additional circuitry required for a signal to be added to the batteries will increase cost and add unnecessary weight if included in an electric vehicle. The advantage of this approach however is that the signal that is injected has less noise than a switched mode amplifier [33].

EIS can be performed on a switching converter by superimposing a sinusoidal perturbation onto the duty cycle. [23] uses a conventional non-isolated bidirectional dc–dc boost/buck allowing the perturbation to be superimposed during charging and discharging of the Li-Ion battery. The duty cycle is varied sinusoidally instead of using an external linear signal generator. Therefore, the duty cycle at time *t* is a function of the steady state duty cycle *D* and the sinusoidal EIS perturbation [23]. This is illustrated by Figure 2-27.

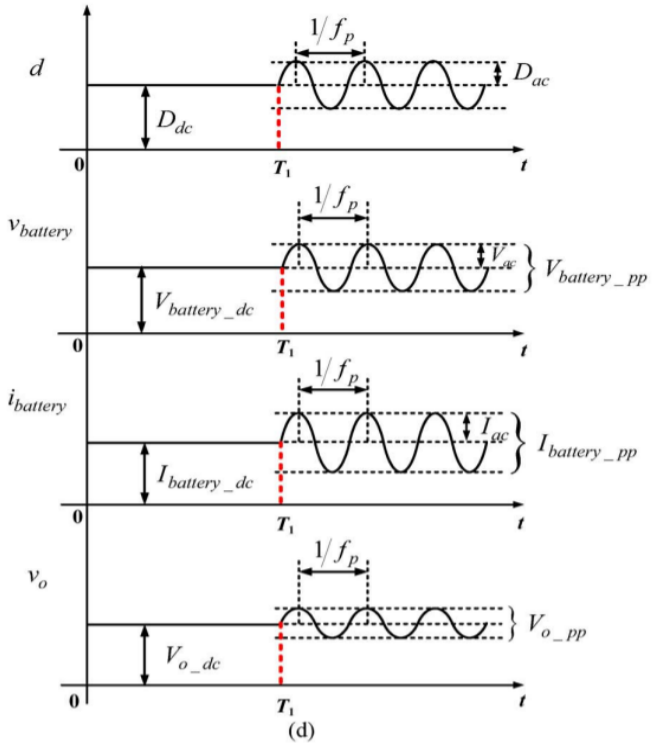


*Figure 2-27. Principle of operation of EIS on switching DC-DC converter* [23]

## 2.11 REVIEW OF ONLINE EIS FOUND IN LITERATURE

Impedance Spectroscopy (IS) has been performed in literature for a variety of electrochemical cells and converter circuit topologies. This section reviews some of the literature which performs IS on a switching converter by varying the duty cycle.

[23] uses a conventional non-isolated bidirectional dc–dc boost/buck. This allows the voltage to be boosted during a discharge and bucked during a charge of the Li-Ion battery pack and allowed EIS measurements to be taken during charging and discharging. This was performed on Li-Ion cells. They only used frequency values from 100 Hz to 10kHz and did not mention lower frequency signal injection. Reference [29] created a lead acid battery charger that could perform EIS. They used the impedance information to estimate the battery's SoH.

Reference [37] created a power converter that injects EIS perturbation signals into a switching converter during cell balancing. The type of switching converter that was used to perform the cell balancing is the switched-inductor ladder converter. This is shown in *Figure 2-28*.

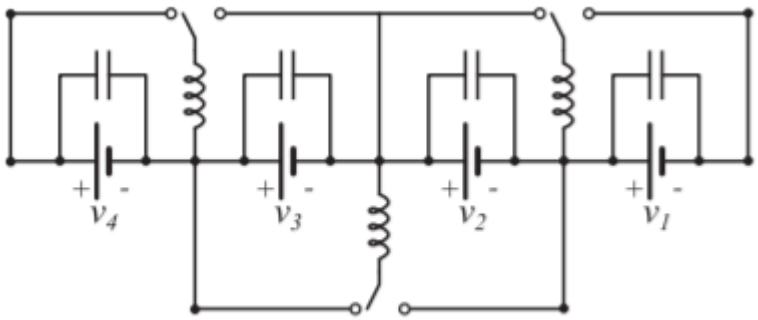


*Figure 2-28. Switched-inductor ladder converter* [37]

Reference [38] used 2 parallel boost converters to connect a PEM Fuel Cell stack to a load and inject AC signals to achieve EIS. The responsibilities of each of the converters is different. The one is used to control the output of the fuel cell stack and the other is to inject the EIS signals. They used closed loop PI converters to control each converter. The findings of this thesis are that the EIS signals could be injected with a low THD as well as produced highly accurate EIS measurements, however, it was only simulated on Simulink. This work successfully demonstrated that the EIS signal generation can be decoupled from the power conversion process.

Reference [39] presented a DC-DC converter for a PEM fuel cell stack which injected BIS perturbation signals and allowed each cell in the stack to be measured which allowed for

advanced condition monitoring. The BIS signal that was injected was a PRBS signal. A step-down buck topology was used [39].

Reference [40] presented an online fuel cell diagnostics controller. The fuel cell stack supplied the load via a DC-DC converter. The system makes use of an inner current controller and an outer voltage controller. The AC perturbation signal is injected into the inner current controller, this however was only done in simulation.

Reference [41] presented online multi-sine impedance spectroscopy. This involved summing multiple sinusoidal perturbations up and injecting it into the duty cycle. This is shown in Figure 2-29. This was only achieved in simulation. Reference [4], however, was able to implement a multi-sine signal on a switched mode bi-directional boost/buck converter on a small stack of Li-Ion Phosphate batteries. Reference [42] created a bi-directional converter that could diagnose PEM fuel cells using BIS. This topology also makes use of a multi-sine signal in a switched mode DC-DC chopper circuit

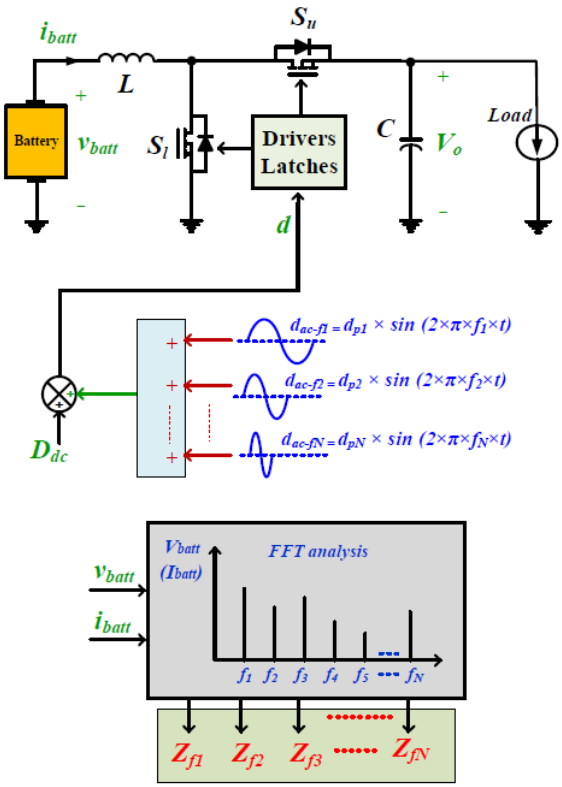


*Figure 2-29. Multi-sine boost converter* [41]

Reference [33] created a battery charger to perform EIS. The charging circuit was a switching chopper circuit. They were also able to obtain the THD analytically. Results obtained were

very close to commercially available EIS devices. Reference [31] also used a buck converter to charge a lead acid battery using the CC/CV method and performed EIS during charging.

Reference [18] used the bi-directional boost/buck topology and performed an EIS measurement strategy to perform the EIS online with regards to the control of the DC bus. The DC bus is controlled under threshold values. During an EIS measurement, the control of the bus is suspended. EIS can be performed if the voltage on the bus remains within the threshold values. If the threshold is exceeded, voltage control is immediately reinstated
The control strategy that was implemented by [18] is shown below in Figure 2-30.

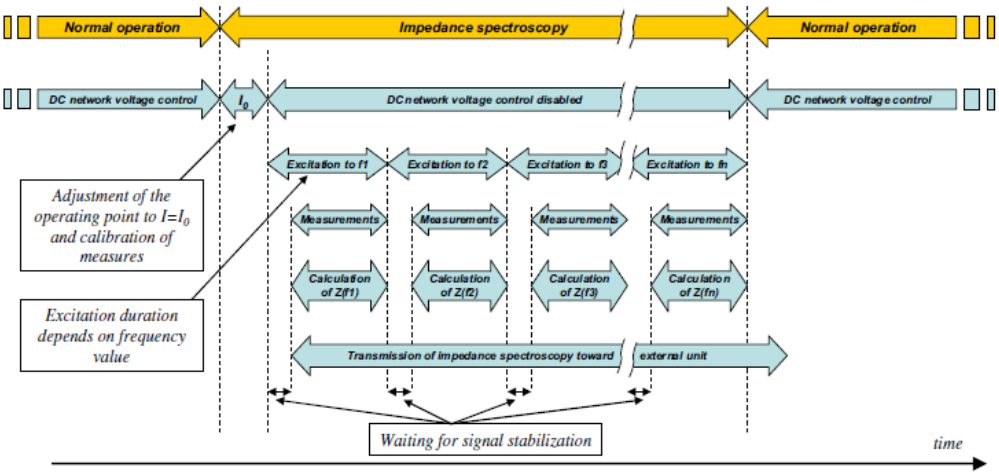


*Figure 2-30. EIS Control strategy implemented by [18]*

Reference [23] developed a practical online system to determine the SoC of a battery system using EIS. Reference [43] used a DC-AC-DC Converter on a PEM fuel cell which makes use of a PLANAR transformer which has very high efficiencies. It makes use of a full bridge inverter connected to the transformer and then another full bridge transformer. The circuit is shown below in *Figure 2-31*.

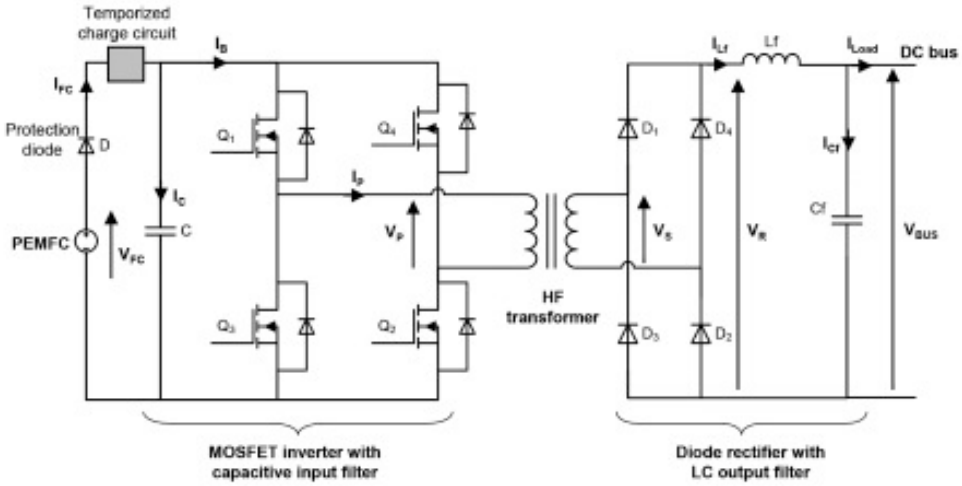


*Figure 2-31. DC-AC-DC Converter topology* [43]

Previous work had explored implementing EIS in the DC-DC converter, either during charging [33], [31] or during a discharging [18], [43], [23]. The major advantage of placing an EIS measurement configuration in the charger is that, there will be less disturbance to the measurements. It should also be noted that for previous work found literature, online IS is carried out with the battery connected to a test load which is well regulated and not an actual running system [23]. The purpose of this project is to implement BIS on a converter for charge and discharge conditions and to consider conditions of variability as per typical field operation. A wind energy conversion system will be considered as a case study to examine its effectiveness. *Table 2-6* below summarizes the online converter Impedance Spectroscopy techniques found in literature and arranges it by converter type, IS signal that was used, the battery/cell that was in test and the EEC that was used to extract the cell's parameters.

*Table 2-6. Overview of selected works*

| Ref | Description | Converter Topology | Impedance Spectroscopy Type | Battery | EEC |
|---|---|---|---|---|---|
| [18] | Online impedance spectroscopy of lead acid batteries for storage management of a standalone power plant | Bi-direction boost/buck converter | Single sinusoid injection (0.32 Hz – 1024 Hz) | Lead Acid | Randles |
| [23] | An Online Battery Impedance Measurement Method Using DC–DC Power Converter Control | Bi-directional boost/buck converter | Single sinusoid injection (100Hz - 10kHz) | Li-Ion | Thevin R RC |
| [31] | Determining battery SoC using Electrochemical Impedance Spectroscopy and the Extreme Learning Machine | Buck converter (CC/CV) charger | Single sinusoid injection | Lead acid battery | N/A |
| [33] | Impedance spectroscopy for battery monitoring with switched mode amplifiers | DC Chopper (Stepped down bidirectional charging circuit) | Single-sinusoid (10 mHz – 5kHz) | Li-Ion Phosphate batteries | N/A |
| [42] | Real-Time Electrochemical Impedance Diagnosis for Fuel Cells Using a DC–DC Converter | DC Chopper | Multi-sine | PEM Fuel cell | RC-R-RC |
| [37] | A Scalable Active Battery Management System with Embedded Real-Time Electrochemical Impedance Spectroscopy | Switched Inductor ladder converter | Sine signal 25 mHz to 7.66 kHz | Li-Ion | Thevenin R-RC with virtual inductor |
| [38] | Modelling and simulation of parallel DC/DC converters for online AC impedance estimation of PEM fuel cell stack | Parallel DC-DC topology (bi-directional boost/buck) | Single sinusoid injections (0.1Hz to 1000 Hz) | PEM Fuel cell | Randles model |
| [39] | Fuel Cell Condition Monitoring System Based on Interconnected DC-DC Converter and Voltage Monitor | Bi-directional buck converter | PRBS | PEM Fuel cell | N/A |
| [40] | A new on-line state-of-health monitoring technique dedicated to PEM fuel cell | Boost converter | Multi sine [1Hz-1kHz] | PEM Fuel cell | N/A |
| [41] | Online Battery Impedance Spectrum Measurement Method | Bi-directional boost/buck converter | Multi-sine [1kHz, 5kHz, 10kHz] (simulated) | Li-Ion | N/A |
| [43] | Integration of electrochemical impedance spectroscopy functionality in proton exchange membrane fuel cell power converter | DC-AC-DC converter | Single sinusoid injection | PEM Fuel cell | N/A |

## 2.12 REMARKS AND CONCLUSION

This chapter explored different battery technologies as well as introduced the concept of monitoring the states of the battery. A few techniques for assessing the states of batteries were discussed with an emphasis placed on Impedance Spectroscopy. Two major online techniques were presented for online IS signal injection, the first being the inclusion of a linear amplifier in the BMS and the second is to superimpose the EIS/BIS signal onto the duty cycle of the converter. A literature review was conducted on online IS techniques. It was found that there is a variety of converter topologies and IS signals used in literature.

For this dissertation, the chosen converter is the bi-directional boost/buck converter, due to its ability to charge and discharge a battery. This will allow IS methods to be tested during charging conditions. The IS signal that was chosen is the multi-sine signal due to it being shown to have high accuracy in literature.

# Chapter 3. Design of the BIS Signal And Simulation of DC-DC Converter For Impedance Spectroscopy

As was discussed in the Chapter 2, there are 2 general methods in literature where impedance spectroscopy (IS) is performed on a running system (online). The first being the inclusion of a controllable linear amplifier into the BMS, and the second method is by injecting the IS perturbations using the power converter. The latter is the method that is in focus in this dissertation as it possible to perform this method by adapting the power converter, without additional power electronics. To test this method, a DC-DC switching converter is required. This section details the analytical design of the BIS signal and the design of the DC-DC converter to perform IS measurements with its associated control, which will enable the converter to perform the IS measurements and regulate its DC bus voltage. This test converter is also bi-directional and can charge the battery from a DC supply connected to the DC Bus. These enables IS methods to be tested in charging and discharging mode. A simplified systems diagram is shown in Figure 3-1. The battery system is made up a Li-Ion battery pack. The purpose of this section is to analytically model and simulate the proposed system shown in Figure 3-1.

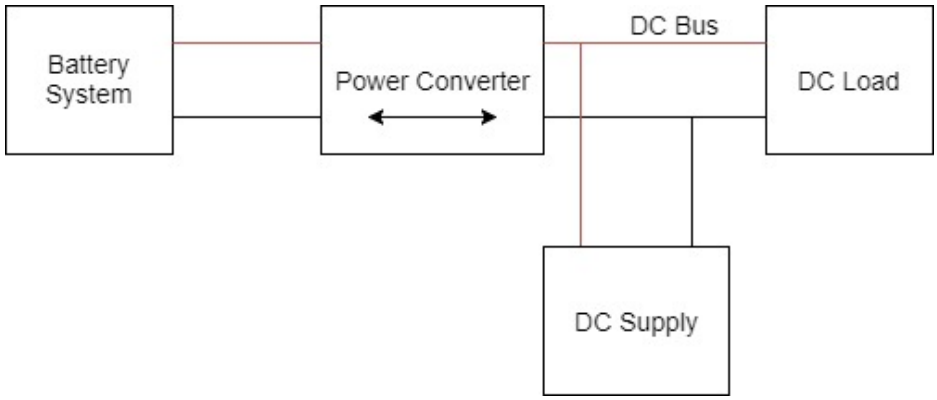


*Figure 3-1 Simplified Power System Prototype*

The Chapter starts off with the design of the BIS signals followed by the design of the DC-DC converter prototype that will be used in experimentation. The Chapter concludes by simulating the proposed system using MATLAB Simulink.

## 3.1 IMPEDANCE SPECTROSCOPY SIGNAL DESIGN

The multi-sine BIS signal is designed using a similar procedure to the methods performed in [3], [4] , [5]. For a multi-sine signal, the injected signal is given by (3-1). This represents a current dc offset and a BIS signal perturbation.

$$I_{bat}(t) = \ I_{dc} + I_{BIS}(t) \tag{3-1}$$

The BIS multi-sine perturbation signal ($I_{BIS}(t)$), can be represented as (3-2).

$$I_{BIS}(t) = \sum_{n}^{n-1} a_n \, sin(2\pi f_n t + \theta_n) \tag{3-2}$$

Where, $a_n$ is the amplitude matrix, $f_n$ is the frequency matrix and $\theta_n$ is the phase matrix. The values must be carefully selected because by summing multiple sinusoids together, the injected signal can become quite large and could cause the battery to operate in a non-linear region. Thus, the BIS signal should be optimized to produce a signal with a low crest factor (CF). The CF gives an indication of the ratio of the peaks of the waveform to the actual RMS value of the waveform as described in (3-3), with the optimal CF value being 1.

$$CF = \frac{\sqrt{2}\times max|i(t)|}{\sqrt{\sum_{n=0}^{N-1} {a_n}^2}}, t \in [0, T] \tag{3-3}$$

The signal needed to be optimized to ensure linear and stable operation. There are 3 variables of the BIS signal given in (3-2) that can be optimized. They are the frequency distribution ($f_n$), the amplitudes ($a_n$) and phase ($\theta_n$) of the injected current signal.

### 3.1.1 Choice of Frequencies

The first variable that must be chosen are the frequencies that are to be injected. The choice of frequencies should be based on what frequencies would yield the most impedance information that can be used to extract electrochemical information from the Nyquist plot. However, multi-sine signals have the disadvantage of harmonics interfering with other injected frequencies. This can be observed using an FFT on a multi-sine signal. Each perturbation frequency produces '*sinc*' function around each injected frequency in the frequency domain and creates signal overlap causing crosstalk errors [44]. Therefore, the same frequency distribution used for an EIS measurement might not be suitable for a multi-sine signal. Reference [3] used a harmonic distribution frequency spread to avoid this crosstalk error using a distribution is given by (3-4).

$$f_n = f_0 \times 2^n \quad n = 0 : N-1 \tag{3-4}$$

Where $f_0$ is the lowest frequency of interest, and determines the how long the measurement will take. This harmonic distribution, eliminates the crosstalk error and ascertains that, for the designed frequency spectrum, all frequencies are integer multiples of the lowest frequency to ensure periodicity [24]. The disadvantage of this method however, is that frequency resolution is lower at higher frequencies.

This harmonically spaced frequency distribution was chosen for this research. The frequencies that were chosen for the full spectrum was $f_0 = 0.02\,Hz$ and $N = 18$. This provided impedance information between $0.02\,Hz$ and $2621.44\,Hz$. Another issue that had to be addressed is the length of measurement time. If the current on the DC-bus is varying significantly, it may be inappropriate to perform a 50 second IS measurement. Therefore, a shorter BIS signal was chosen with $f_0 = 1$ Hz and $N = 11$ for when the current is varying considerably. This signal provided impedance information between 1Hz and 2048 Hz. This frequency range was determined experimentally and was found to be a good trade-off between a fast measurement time and impedance information. This range was chosen similarly to [41]. The disadvantage is that sub-hertz frequency information is lost, however, it allows for significantly shorter measurement times.

### 3.1.2 Amplitude Optimization

A common value in literature for the amplitude of the sinusoid is 10% of the DC current, $I_{dc}$. Although this is suitable for EIS measurements, it can introduce a large Crest Factor for BIS. Therefore, the amplitude matrix, $a_n$ , must be optimized. This can be done by adjusting the value of $a_n$ for each frequency so that the voltage response is the same for each frequency [3] [42]. This is achieved by taking an initial BIS measurement with $a = 10\%\ of\ I_{dc}$ ,and then calculating the current for each frequency that would be required to produce the same voltage response for all frequencies in that measurement, this is shown in (3-5), where $Z_n$ is the impedance from the initial impedance measurement.

$$optimized\ a_n = a \times \frac{\frac{1}{|Z_n|}}{max\ (|Z_n|^{-1})} \tag{3-5}$$

### 3.1.3 Phase Optimization

The last variable that can be optimized in the multi-sine signal is the phase matrix $\theta_n$. To optimize the phase values, the Crest Factor (CF) of the BIS current signal $i_{BIS}(t)$ was minimized with phase being the controlled variable as given in (3-6) [5].

$$min(CF) = min_{\theta}\left(\frac{\sqrt{2}max|i(t)|}{\sqrt{\sum_{n=0}^{N-1} {a_n}^2}}\right) \tag{3-6}$$

### 3.1.4 Final Injected Signals

For the longer BIS signal where, $f_o = 0.02\ Hz$. The optimization techniques described above were used to reduce the CF of the injected signal from an unoptimized values of 1.875 to a suitable value of 1.44. The results from the amplitude and phase optimization is shown in Figure 3-2 where $i_{dc} = 0.5A$.[3]

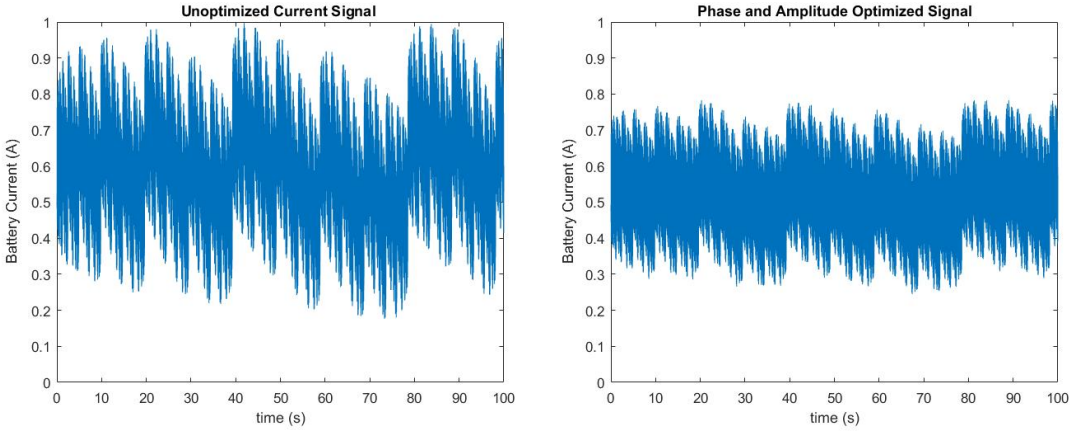


(a) (b)

*Figure 3-2. (a) Unoptimized multi-sine BIS signal. (b) Phase and amplitude optimized BIS signal*

The values chosen for $I_{dc}$ was between 0.5A and 2A. The amplitude was set initially to 10% of $I_{dc}$ (before the amplitude and phase optimization procedure was performed). The frequency array used the harmonic distribution discussed. The values that were used are given in Appendix A4. The shorter BIS signal was also optimized this is shown in Figure 3-3 below. The optimization reduced the signal's crest factor from 1.56 to 1.35.

[3] Refer to MATLAB optimization code in the Appendix A3.

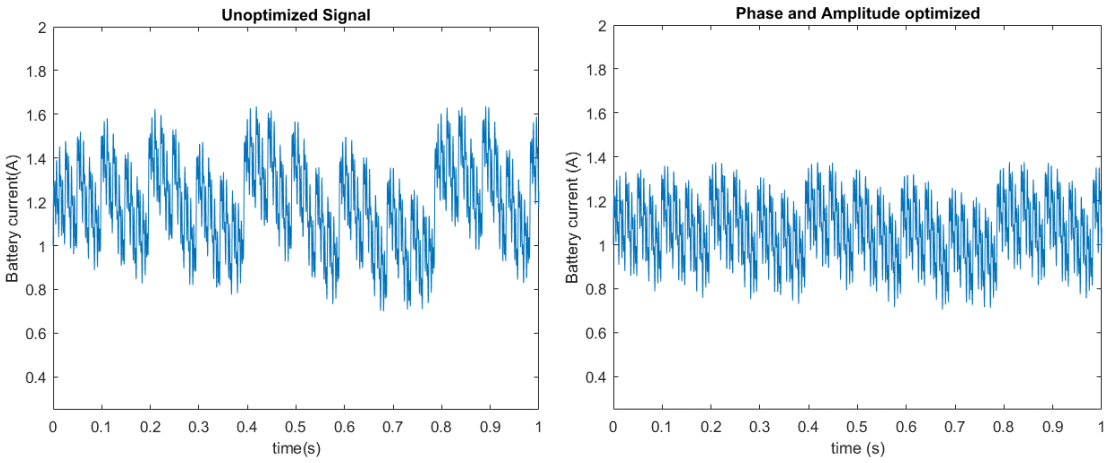


(a) (b)

*Figure 3-3. Unoptimized multi-sine BIS signal. (b) Phase and amplitude optimized BIS signal*

## 3.2 ANALYTICAL DESIGN OF THE DC-DC CONVERTER

The Li-Ion battery system is connected to the load and current supply via a DC-DC power converter, which regulates the voltage on the DC bus (Figure 3-4). For the proposed system, it is assumed that the voltage of the Li-Ion battery system is lower than that required by the DC bus. The bi-directional boost/buck converter was selected as it allows forward and reverse current operation. This topology was used by [45] to regulate bi-directional flow on the DC bus and was also used by [18], [38] to perform single sinusoid EIS measurements.

In the forward current operation mode, the battery voltage is boosted and supplies current to the DC bus, while in the reverse current operation mode, the DC bus voltage is bucked to a lower value to charge the battery. A schematic of the bi-directional boos/buck converter is shown in Figure 3-4. The DC Supply, follows the bus voltage and can thus be modelled as a current source $I_{supply}$ and the DC Load is modelled as a constant resistance $R_{load}$.

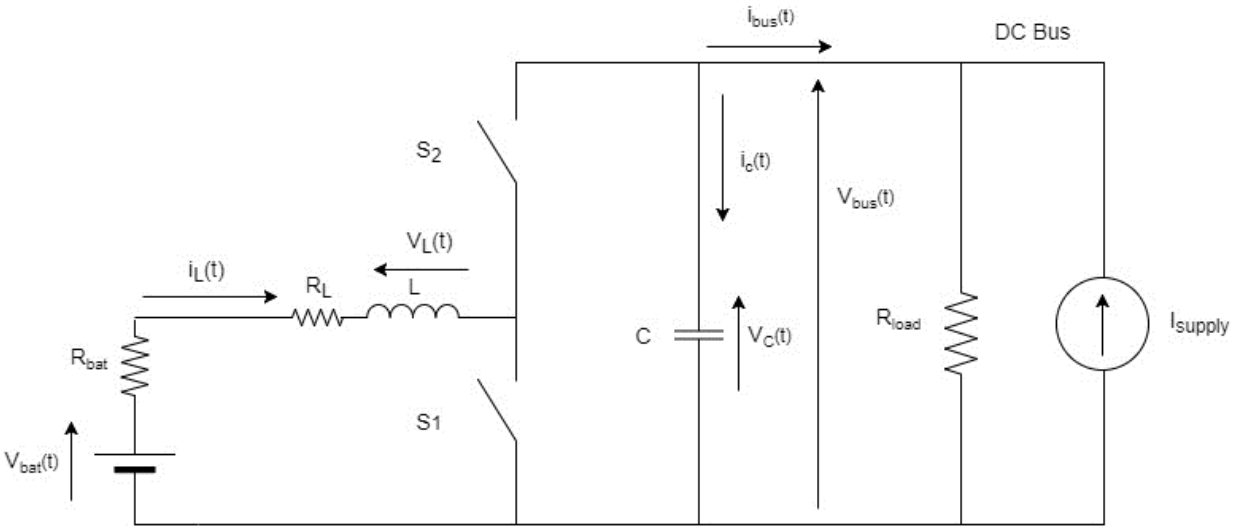


*Figure 3-4. Bi-directional Buck/boost Converter*

The switches are controlled synchronously. Synchronous rectification is a method by which the MOSFETs are controlled together. Each of the MOSFETs are controlled with a PWM waveform that is 180 degrees out of phase, i.e. when S1 is on, then S2 is off and vice versa. Synchronous rectification is simpler to control as it does not need to determine the direction of current flow, as would have to be done if the MOSFETs were controlled independently. Therefore, synchronous rectification of the MOSFETs will be used in this dissertation.

## 3.3 MODELLING THE DC-DC CONVERTER

The converter is initially modelled analytically by obtaining a mathematical description of the circuit. This is done to determine the suitable transfer function for design of the controller which injects current perturbations required for IS as well as controls the DC bus voltage, $V_{BUS}$. The first section describes the basic operation for the converter.

### 3.3.1 Operating Principle of the Converter

The circuit is taken as a non-linear time variant circuit, due to the inclusion of semiconductors switching elements. Figure 3-5[4] below shows the circuit during $T_{on}$, where $S1$ is on and $S2$ is closed. When $S1$ is on, it connects the output of the inductor to ground. This causes a voltage $V_L$ to be established across the inductor[5]. $V_L$ steadily decreases, while the inductor current $I_L$ rises. The capacitor discharges through the load resistor, which causes $V_C$ to steadily decrease.

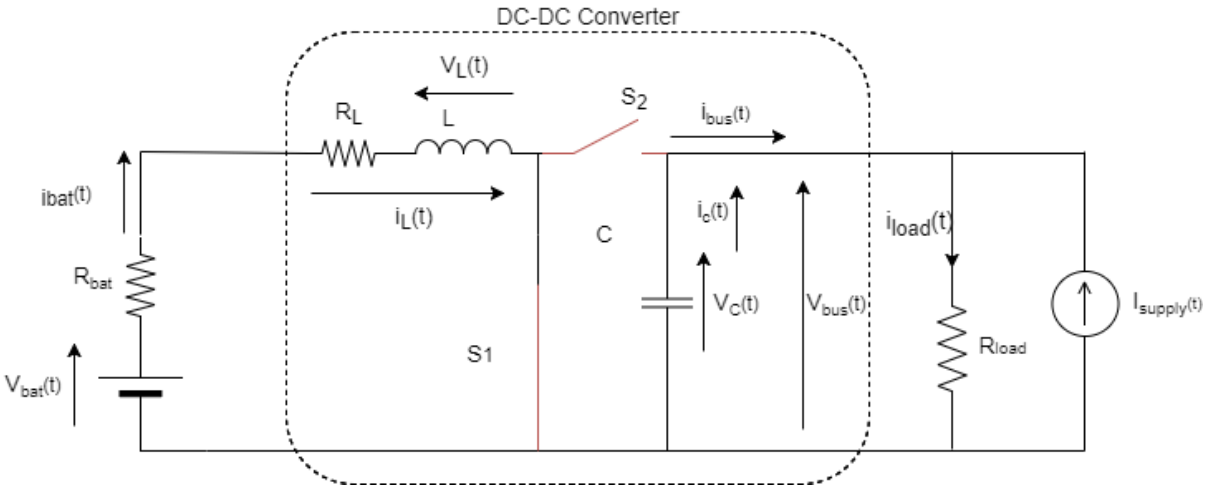


*Figure 3-5. Boost Converter with S1 ON and S2 OFF*

Equations are obtained by using Kirchhoff's' Voltage Law (KVL) and Kirchhoff's Current Law (KCL) for the circuit in Figure 3-5, where S1 is ON and S2 is OFF, the circuit can be represented analytically as from (3-7) and (3-8):

[4] For this analytical section, the voltage drop of the diodes and MOSFETs are not considered, and are considered to be ideal switches.
[5] This assumes that the inductor is operating in constant conduction mode and that *ibus* is positive

$$V_{bat} - i_L(t)(R_L + R_{bat}) - v_L(t) = 0 \tag{3-7}$$

$$i_c(t) + \frac{v_c(t)}{R_{LOAD}} - i_{supply}(t) = 0 \tag{3-8}$$

When, S1 is off and S2 is on (Figure 3-6), the inductor is connected to the output capacitor, $V_L$ steadily decreases and the capacitor is charged during this time, causing $V_C$ to rise. Using KVL and KCL, the circuit is represented by (3-9) and (3-10).

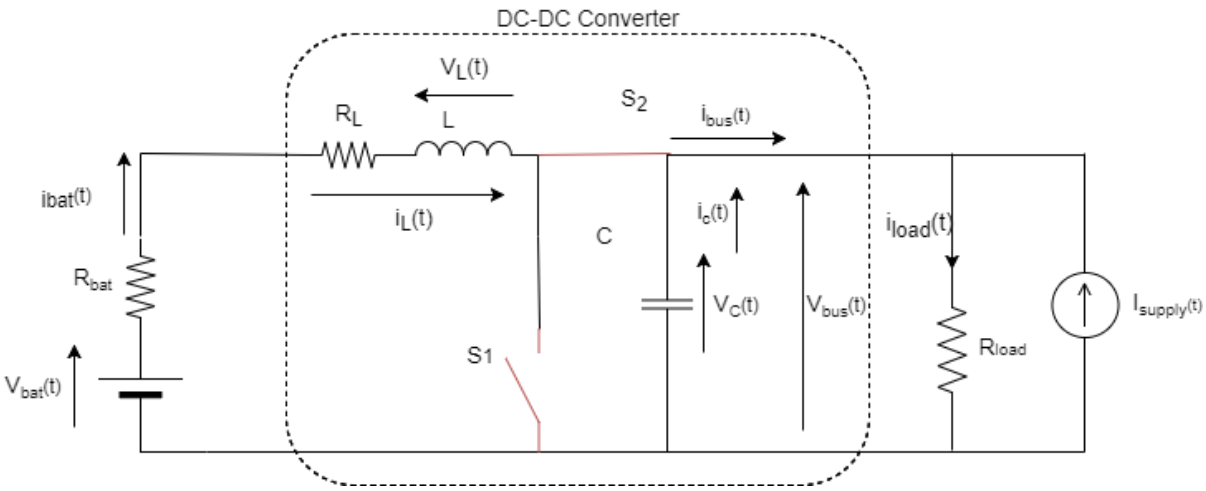


*Figure 3-6. Boost converter with S1 OFF and S2 ON*

$$V_{bat} - i_L(t)(R_L + R_{bat}) - v_L(t) - v_c(t) = 0 \tag{3-9}$$

$$i_c(t) - i_L(t) + \frac{v_c(t)}{R_{LOAD}} - i_{supply}(t) = 0 \tag{3-10}$$

For both cases illustrated in Figure 3-5 and Figure 3-6, the voltage across the inductor and current flowing into the capacitor are given by (3.11) and (3.12) respectively.

$$v_L(t) = -L\frac{di_L(t)}{dt} \tag{3-11}$$

$$i_c(t) = -C\frac{dv_c(t)}{dt} \tag{3-12}$$

Figure 3-7 illustrates example waveforms for $i_L(t)$ and $v_c(t)$.

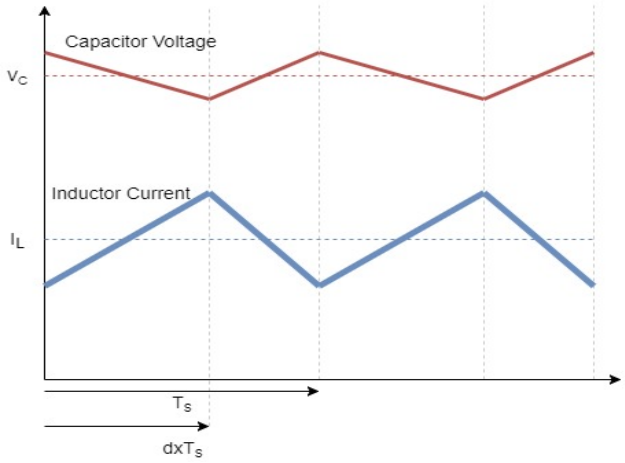


*Figure 3-7. Capacitor voltage and inductor current waveforms*

During steady state operation, the average voltage across the inductor and the average current of the output capacitor is 0. Therefore, by equating these to 0 and realising that S1 is closed and S2 is open for $dT_s$ and S1 is open and S2 is closed for $(1-d)T_s$, the DC equations can be rewritten as (3-13) and (3-14).

$$(D)(V_{bat} - I_L(R_L + R_{bat})) + (1-D)(V_{bat} - I_L(R_L + R_{bat}) - V_c) = 0 \tag{3-13}$$

$$(D)\left(I_{supply} - \frac{V_c}{R_{LOAD}}\right) + (1-D)\left(I_L + I_{supply} - \frac{V_c}{R_{LOAD}}\right) = 0 \tag{3-14}$$

Solving for $V_c$ and $I_L$

$$I_L = \left(\frac{V_{bat}}{R_{LOAD}(1-D)^2}\frac{1}{\frac{(R_L + R_{bat})}{R_{LOAD}(1-D)^2} + 1}\right) - \left(\frac{I_{supply}}{(1-D) + \frac{R_L + R_{bat}}{R_{LOAD}(1-D)}}\right) \tag{3-15}$$

$$V_c = \left(\frac{V_{bat}}{(1-D)}\frac{1}{\frac{(R_L + R_{bat})}{(1-D)^2 R_{LOAD}} + 1}\right) + \left(\frac{I_{supply}}{(1-D)^2 + \frac{R_L + R_{bat}}{R_{LOAD}}}\right) \tag{3-16}$$

For an ideal converter, the inductor and battery resistance are negligible ($R_L = 0, R_{bat} = 0$). The equations for capacitor voltage and inductor current are then given by the equations below. There is a non-linear relationship between inductor current $I_L$, output voltage $V_c$ and the duty cycle D.

$$I_L = \frac{V_{bat}}{R_{LOAD}(1-D)^2} - \frac{I_{supply}}{(1-D)} \tag{3-17}$$

$$V_c = \frac{V_{bat}}{(1-D)} + \frac{I_{supply}}{(1-D)^2} \tag{3-18}$$

From (3-17), if we assume that $V_{bat}$ is positive and that the duty cycle $D$ lies between 0 and 1, then the direction of the inductor current $I_L$ is determined by the magnitude of the current input on the DC bus $I_{supply}$. Note that $I_{supply}$ is assumed to be a purely generative source and thus is always positive. If $I_L$<0 the battery is charging, and if $I_L$ > 0 the battery is discharging There are 4 possible modes of operation that can occur depending on the loading condition and inductor current, as shown in Table 3-1.

Table 3-1. Converter modes of operation

| Mode | $I_L$ | $I_{supply}$ | $R_{LOAD}$ |
|---|---|---|---|
| 1 | >0 | =0 | $0 < R_{LOAD} < \infty$ |
| 2 | >0 | >0 | $0 < R_{LOAD} < \infty$ |
| 3 | <0 | >0 | $R_{LOAD} = \infty$ , Disconnected |
| 4 | <0 | >0 | $0 < R_{LOAD} < \infty$ |

### 3.3.2 State Space modelling

To define the desired linear controller for the converter, a state space averaged model is required [46]. If a system is time-invariant, it can be represented by a state space model. This takes the form of the equations below where $x$ is a state vector, $u$ is the input vector and $y$ is the output vector. The matrices A, B, C, D describe the system dynamics [47].

$$\dot{x} = Ax + Bu \tag{3-19}$$

$$y = Cx + Du \tag{3-20}$$

For both the forward boost and the reverse buck operation of the circuit, the state vector consists of the derivatives of the inductor current and the capacitor voltage. These are the inductor current $i_L$ and capacitor voltage $v_c$ respectively. $\dot{x}$ is the state vector and has the same dimensions as the number of storage elements in the circuit.

$$\dot{x} = \begin{bmatrix} \frac{di_L(t)}{dt} \\ \frac{dv_c(t)}{dt} \end{bmatrix} \tag{3-21}$$

The operation of boost and buck converters are non-linear and time variant, due to the switching components. The converter can however be represented in state space form by averaging out the operation in both states of operation. To obtain the state matrix representation, the equations should have the form [47]:

$$\dot{x} = A_1 x + B_1 u \quad during\ d \cdot T_s \tag{3-22}$$

$$\dot{x} = A_2 x + B_2 u \quad during\ (1-d) \cdot T_s \tag{3-23}$$

Over an interval of $T_s$, the system is in state 1 for $d$ and in state 2 for $(1-d)$. Therefore, by averaging out the equations the system can be rewritten as:

$$A = A_1 d + A_2 (1-d) \tag{3-24}$$

$$B = B_1 d + B_2 (1-d) \tag{3-25}$$

During $d \cdot T_s$, where S1 is open and S1 is closed (Figure 3-5), the state equations can be written as:

$$V_{bat} - i_L(t)(R_L + R_{bat}) - L\frac{di_L(t)}{dt} = 0 \tag{3-26}$$

$$C\frac{dv_c(t)}{dt} + \frac{v_c(t)}{R_{Load}} - i_{supply} = 0 \tag{3-27}$$

Converting this to matrix form results in the equations below:

$$\begin{bmatrix} i_L \\ \dot{v}_c \end{bmatrix} = \begin{bmatrix} \frac{-(R_L + R_{bat})}{L} & 0 \\ 0 & \frac{-1}{R_{Load}C} \end{bmatrix} \begin{bmatrix} I_L \\ V_c \end{bmatrix} + \begin{bmatrix} \frac{1}{L} & 0 \\ 0 & \frac{1}{C} \end{bmatrix} \begin{bmatrix} v_{bat} \\ i_{supply} \end{bmatrix} \tag{3-28}$$

$$A_1 = \begin{bmatrix} \frac{-(R_L + R_{bat})}{L} & 0 \\ 0 & \frac{-1}{R_{Load}C} \end{bmatrix}, \qquad B_1 = \begin{bmatrix} \frac{1}{L} & 0 \\ 0 & \frac{1}{C} \end{bmatrix} \tag{3-29}$$

During $(1-d)\cdot T_s$, where S1 is open and S2 is closed. The state equations can be written as:

$$v_{bat} - i_L(t)(R_L + R_{bat}) - L\frac{di_L(t)}{dt} - v_c(t) = 0 \tag{3-30}$$

$$-i_L(t) + C\frac{dv_c(t)}{dt} + \frac{v_c(t)}{R_{LOAD}} - i_{supply} = 0 \tag{3-31}$$

Converting this to matrix form results in:

$$\begin{bmatrix} \frac{di_L}{dt} \\ \frac{dv_c}{dt} \end{bmatrix} = \begin{bmatrix} \frac{-(R_L+R_{bat})}{L} & -\frac{1}{L} \\ \frac{1}{C} & -\frac{1}{R_{LOAD}C} \end{bmatrix} \begin{bmatrix} I_L \\ V_c \end{bmatrix} + \begin{bmatrix} \frac{1}{L} & 0 \\ 0 & \frac{1}{C} \end{bmatrix} \begin{bmatrix} v_{bat} \\ i_{supply} \end{bmatrix} \tag{3-32}$$

$$A_2 = \begin{bmatrix} \frac{-(R_L+R_{bat})}{L} & -\frac{1}{L} \\ \frac{1}{C} & -\frac{1}{R_{LOAD}C} \end{bmatrix}, \qquad B_2 = \begin{bmatrix} \frac{1}{L} \\ \frac{1}{C} \end{bmatrix} \tag{3-33}$$

The next step is to average out the equations over switching cycle $T_s$[6] using (3-24) and (3-25)

$$A = d\begin{bmatrix} \frac{-(R_L+R_{bat})}{L} & 0 \\ 0 & \frac{-1}{R_{Loaa}C} \end{bmatrix} + (1-d)\begin{bmatrix} \frac{-(R_L+R_{bat})}{L} & -\frac{1}{L} \\ \frac{1}{C} & -\frac{1}{R_{LOAD}C} \end{bmatrix} = \begin{bmatrix} \frac{-(R_L+R_{bat})}{L} & -\frac{(1-d)}{L} \\ \frac{(1-d)}{C} & -\frac{1}{R_{LOAD}C} \end{bmatrix}$$

$$B = \begin{bmatrix} \frac{1}{L} & 0 \\ 0 & \frac{1}{C} \end{bmatrix} d + \begin{bmatrix} \frac{1}{L} & 0 \\ 0 & \frac{1}{C} \end{bmatrix} (1-d) = \begin{bmatrix} \frac{1}{L} & 0 \\ 0 & \frac{1}{C} \end{bmatrix}$$

The final state representation for the converter is given by (3-34).

$$\begin{bmatrix} \frac{di_L}{dt} \\ \frac{dv_c}{dt} \end{bmatrix} = \begin{bmatrix} \frac{-(R_L+R_{bat})}{L} & -\frac{(1-d)}{L} \\ \frac{(1-d)}{C} & -\frac{1}{R_{LOAD}C} \end{bmatrix} \begin{bmatrix} I_L \\ V_c \end{bmatrix} + \begin{bmatrix} \frac{1}{L} & 0 \\ 0 & \frac{1}{C} \end{bmatrix} \begin{bmatrix} v_{bat} \\ i_{supply} \end{bmatrix} \tag{3-34}$$

[6] The converter is operating in CCM therefore, the state space averaging technique can be used.

### 3.3.3 Deriving Transfer Function

The circuit averaging technique performed in the section above gives a state model which is time invariant, but it is still non-linear. Although the converter is a non-linear system, it is possible to derive a transfer function using small signal approximation [48] [47]. It has been conducted successfully in reference [29] and [38]. Small signal analysis assumes that the input signal is small in magnitude thus the system can be assumed to be pseudo linear as it is operating about a small linear point. This technique of small signal analysis is a common technique to obtain a transfer function on converters and gives a linear time-invariant approximation of a non-linear time-variant system which allows for simpler analysis and control. The first step is to substitute the variables in the converter state equations, by their DC and AC counterparts as shown by the equations below.

$$\begin{aligned} u &= U + \tilde{u} \\ x &= X + \tilde{x} \\ d &= D + \tilde{d} \end{aligned} \tag{3-35}$$

Inserting the DC and AC signals into the State equation results in [47]:

$$\dot{X} + \dot{x} = (A_1(D + \tilde{d}) + A_2(1 - D - \tilde{d}))(X + \tilde{x}) + (B_1(D + \tilde{d}) + B_2(1 - D - \tilde{d}))(U + \tilde{u}) \tag{3-36}$$

The DC components in the AC model can be easily deduced and are therefore known quantities. There are two assumptions which are then made to linearize (3-36):

1. The second order terms are neglected as they are considered very small [47] [48]. i.e. the product of $\tilde{d}$ $and$ $\tilde{v}_c$ $or$ $\tilde{\imath}_L$ will be very small so it can be neglected. This assumption allows for the removal of all second order terms, effectively linearizing the equations.
2. The input vector $U$ which consists of $v_{bus}$ and $i_{supply}$, has a negligible AC perturbation component, and thus only the DC component of $U$ will be considered [48].

The circuit is also assumed to be at steady state therefore $\dot{X} = 0$. Equation (3-36) can therefore be rewritten as (3-37).

$$\dot{\tilde{x}} = A\tilde{x} + \lfloor (A_1 - A_2)X + (B_1 - B_2)\,U \rfloor \tilde{d} \tag{3-37}$$

To obtain the transfer function, the Laplace transform must be taken. This is shown by the equations below.

$$s\tilde{x} = A\tilde{x} + [(A_1 - A_2)X + ((B_1 - B_2)U]\tilde{d}$$

$$\tilde{x}(s) = [sI - A]^{-1}[(A_1 - A_2)X + ((B_1 - B_2)U]\tilde{d}(s) \tag{3-38}$$

The final transfer function is given by (3-39) below.

$$\begin{bmatrix} \tilde{\imath}_L(s) \\ \tilde{v}_C(s) \end{bmatrix}$$

$$= \frac{1}{s^2 + \left(\frac{(R_L + R_{bat})}{L} + \frac{1}{R_{LOAD}C}\right)s + \frac{(R_L + R_{bat})}{R_{LOAD}LC} + \frac{(1-D)^2}{LC}} \begin{bmatrix} s + \frac{1}{R_{LOAD}C} & -\frac{(1-D)}{L} \\ \frac{(1-D)}{C} & s + \frac{(R_L + R_{bat})}{L} \end{bmatrix} \begin{bmatrix} \frac{1}{L}V_c \\ -\frac{1}{C}I_L \end{bmatrix} \tilde{d}(s) \tag{3-39}$$

Finally, the small signal transfer function for the capacitor voltage $V_c$, and the inductor current $I_L$ is given by (3-40) and (3-41) respectively.

$$G_{Vc} = \frac{\tilde{v}_C(s)}{\tilde{d}(s)} = \frac{-\frac{1}{C}I_L s - I_L\frac{(R_L + R_{bat})}{LC} + V_c\frac{(1-D)}{LC}}{s^2 + \left(\frac{(R_L + R_{bat})}{L} + \frac{1}{R_{LOAD}C}\right)s + \frac{(R_L + R_{bat})}{R_{LOAD}LC} + \frac{(1-D)^2}{LC}} \tag{3-40}$$

$$G_{IL} = \frac{\tilde{\imath}_L(s)}{\tilde{d}(s)} = \frac{\frac{1}{L}V_c s + \frac{V_c}{R_{LOAD}LC} + \frac{(1-D)}{LC}I_L}{s^2 + \left(\frac{(R_L + R_{bat})}{L} + \frac{1}{R_{LOAD}C}\right)s + \frac{(R_L + R_{bat})}{R_{LOAD}LC} + \frac{(1-D)^2}{LC}} \tag{3-41}$$

The $G_{Vc}$ transfer function will be used by the controller to control the output bus voltage $V_c$. An important part of this dissertation is to establish the relationship between the current perturbation $\tilde{\imath}_L$ and the duty cycle $d$, as it is the duty cycle that is varied to produce the current perturbation in the battery for a BIS measurement, thus the transfer function for $I_L$ will be used to calculate the duty cycle perturbations required for EIS measurements.

## 3.4 CONVERTER SPECIFICATIONS

A mathematical model of the bi-directional buck/boost converter has been established from Sections 4.1 – 4.2. Next, we determine suitable component values, filter specifications and control parameters for the converter simulation.

### 3.4.1 Input and outputs

The desired input and output voltages ratings of the prototype converter, or the $V_{bat}$ and $V_{bus}$ requirements of the device are chosen such that; $V_{bus}$ voltage would be 20 $V$, $V_{bat\_MAX}$ = 12 V, which can be made up of 3 Li-Ion cells connected in series at 4V each and the minimum battery voltage is $V_{bat\_MIN}$ at 9V. The estimated power throughput of the converter at rated conditions will be 40W.

### 3.4.2 Inductor Selection

The selection of an adequate inductor is crucial for proper buck and boost operation. The choice of the inductor (and switching frequency), determines the ripple current in the battery. The switching frequency, $f_s$ of the circuit was chosen to be 20kHz**.** This frequency is deemed sufficient for generating up to 2kHz sinusoid for EIS implementation as applicable in various literature, such as in [33]. Thus, the ripple current ($\Delta I_L$) can be obtained using Equation (3-42).

$$\Delta I_L = \frac{V_{IN} D}{L f s} \tag{3-42}$$

There is an inversely proportional relationship between the peak to peak ripple current and inductance. It is important to ascertain the reduction of inductor ripple current as much as possible. It would ensure that the inductor continues to operate in Continuous Conduction Mode (CCM) and reduce the ripple current waveform in the battery, since the impedance spectroscopy signals are modulated onto the inductor current as stated in 2.8. The inductor ripple current was chosen to be $\Delta I_L = 1.5A$. Therefore, an inductor of 160 uH was required.

The requirement of CCM, is that the inductor current never falls below 0. The boundary condition between discontinuous conduction mode (DCM) and CCM, occurs when the inductor current is half of the inductor ripple current. Therefore, the boundary condition occurs when $I_L = \frac{\Delta I_L}{2}$. The

boundary condition occurs when the inductor current goes below 0. This is given by the following equation from [47].

$$I_{L\_boundary} = \frac{V_{bus}D}{2Lfs}(1-D)$$

$$I_{o_{boundary}} = \frac{V_{bus}D}{2Lfs}(1-D)^2 \tag{3-43}$$

These boundary conditions are graphed in Figure 3-8. Above the boundary lines, the converter is operating in CCM.

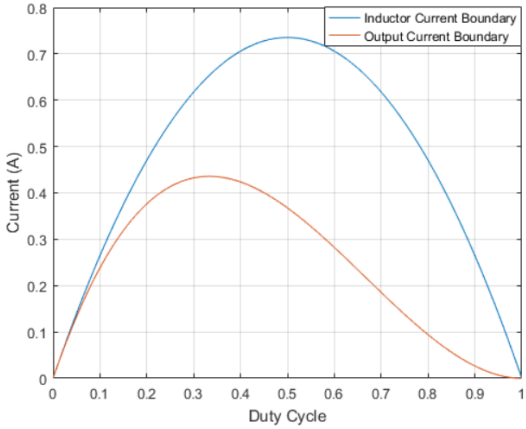


*Figure 3-8. Current Boundary Conditions for CCM*

The equations in (3-46) would be used to determine the duty cycle limitations during control, as well as, while performing online impedance spectroscopy.

### 3.4.3 Filter Capacitor on V_BUS

An output filter capacitor is required to reduce the output voltage ripple on the voltage bus during a boost mode operation. The minimum required capacitor value is estimated as $C_{out,min} = 440\mu F$. It was estimated using (3-44).

$$C_{OUT(min)} = \frac{I_{OUT(MAX)} \times D}{f_s \times \Delta V_{out}} \tag{3-44}$$

Where, $I_{OUT(MAX)}$ to the load is 5A at a duty cycle of 0.5 and the acceptable voltage ripple, $\Delta V_{out}$ is 0.3 V which represents a less than a 1.5% voltage ripple.

## 3.5 CONVERTER CONTROL

The converter can be considered open-loop, if it does not have a feedback loop from the output. i.e., the input has no "knowledge" of the output signal. In open-loop control, the converter can be modelled as shown in Figure 3-9. Open loop analysis was conducted on the transfer functions $G_{V_c}(s)$ and $G_{I_L}(s)$ (derived from Section 3.2) using MATLAB. These are discussed below.

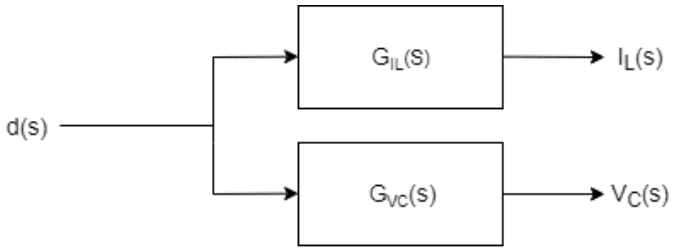


*Figure 3-9. Open loop DC-DC converter*

### 3.5.1 Frequency and Time domain analysis of Open-loop converter

The first aspect that was investigated was the frequency response of the open-loop converter. The bode plot was plotted for different values of $R_{LOAD}$ and duty cycle. Figure 3-10 below shows the frequency response of the capacitor voltage $V_C$ inductor current $I_L$.

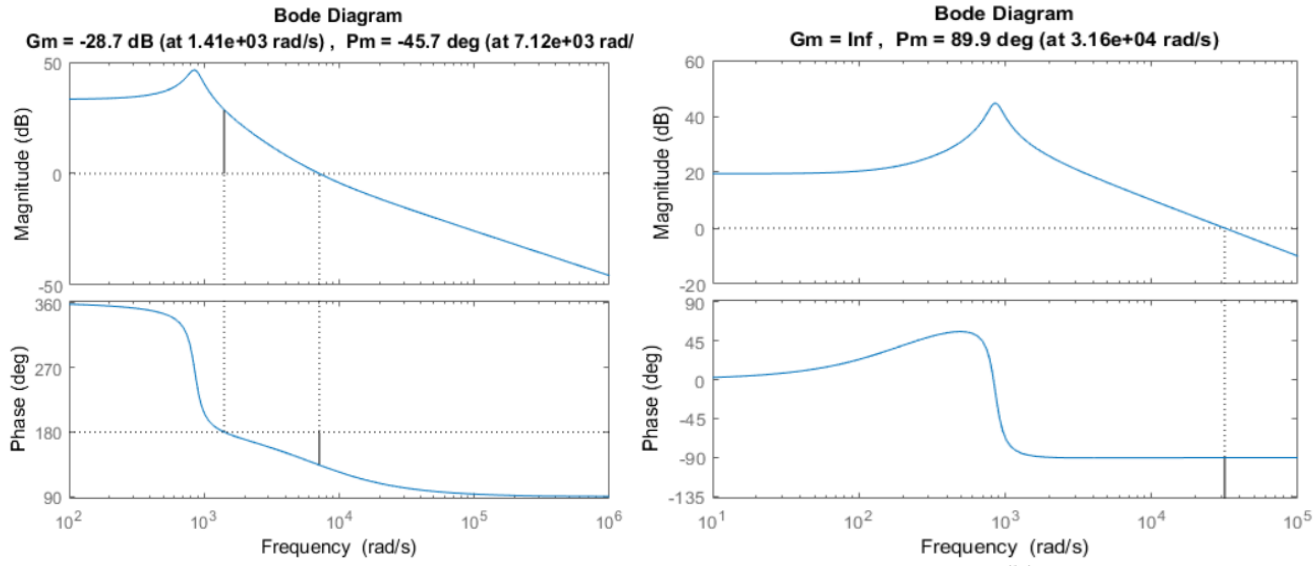


(a) (b)

*Figure 3-10. Gain and Phase margins illustrated for (a) Capacitor Voltage and (b) Inductor Current*

The gain and phase margin characteristics for the frequency response of $V_C$ and $I_{L.}$ are shown in Table 3-2 below. These are given for different values of $R_{load}$. The gain margin and phase margin indicate the stability of the system. $I_L$ has an infinite gain margin whereas $V_c$ has a negative gain margin.

Table 3-2. Frequency response of inductor

| *Inductor Current $I_{L.}$* | | | | |
|---|---|---|---|---|
| Load resistor | Gain Margin (dB) | Phase Margin | Gain Crossover frequency | Phase crossover frequency |
| 5 | Inf | 89.98 | NaN | 14.32 kHz |
| 10 | Inf | 90.06 | NaN | 14.65 kHz |
| 20 | Inf | 90.10 | NaN | 14.82 kHz |
| *Capacitor Voltage $V_{C.}$* | | | | |
| 5 | -31.73 | -83.99 | 199.83 Hz | 3184.37 Hz |
| 10 | -30.69 | -71.51 | 208.09 Hz | 1705.35 Hz |
| 20 | -28.65 | -45.70 | 223.98 Hz | 1134.14 Hz |

The time domain response was also investigated by observing the step response in MATLAB. Figure 3-11 below shows the step response to a 0.1 step in the duty cycle. In general, both capacitor voltage and inductor current have a settling time of 0.02 seconds to a 0.1 duty cycle step which is a fairly good settling time for regulating the voltage on the DC bus $V_{bus}$.

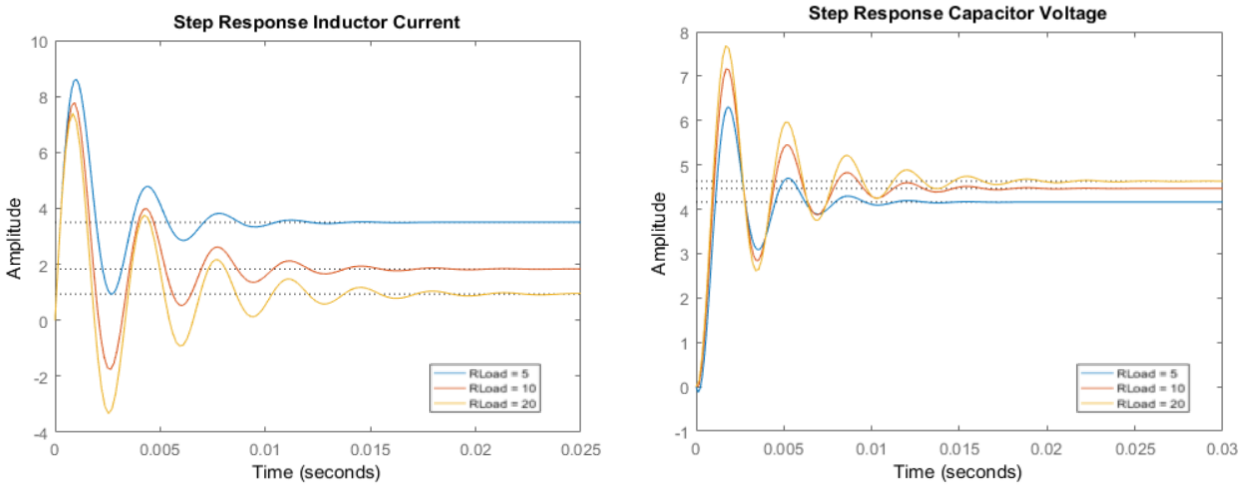


*Figure 3-11. Time domain Step Response*

Open-loop control has the major disadvantage of not being able to withstand disturbances, such as variation in loading condition. It also assumes that the output voltage will be constant and that the parameters of the converter will remain constant (such as inductor resistance). Therefore, feedback control is needed for voltage control. Current injection for impedance spectroscopy, however, only occurs when the system is stable, therefore, open-loop/feedforward control will be used to inject the IS current signals and will be discussed in the next section.

### 3.5.2 Voltage Control

As discussed in Section 3.3, it is possible to calculate the duty cycle required from the transfer function using equation (3-41), however, for open-loop control operation, the controller would be unable to effectively calculate the required duty cycle if there are any disturbances such as changes in temperature, load and input voltage changes, which would affect the value of $V_C$. A common control method to mitigate this is to establish a feedback path as shown in Figure 3-12. The output voltage $V_C$ is subtracted from the setpoint value $r(s)$. This serves as the error signal $e(s)$ supplied into the converter.

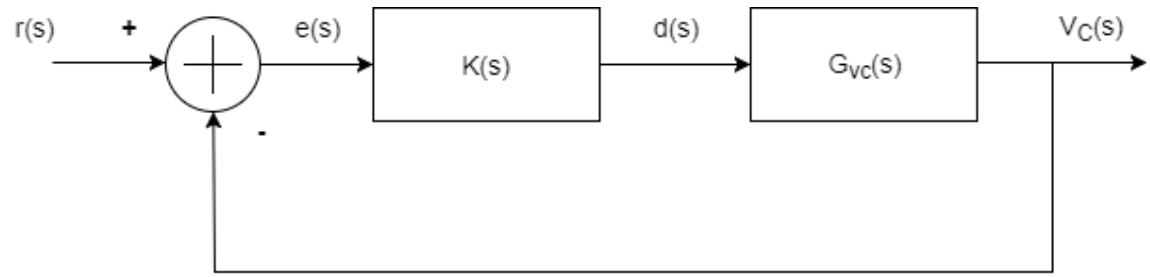


*Figure 3-12 Voltage Control Feedback loop*

The equation for the feedback loop is given by the following equation.

$$H_{Vc}(s) = \frac{V_c(s)}{r(s)} = \frac{1}{1 + K(s)G_{VC}} \tag{3-45}$$

### 3.5.3 Digital Voltage control

A digital controller is required and would be implemented with LABVIEW. MATLAB's continuous to digital function, using the Zero Order Hold (ZOH) method is initially used to convert the transfer function from the s domain to the z domain. The sample time was chosen to be $T_s = \frac{1}{400}$ seconds, as a limitation from real time sampling frequency of the LABVIEW controller. $G_{Vc}(s)$, thus becomes (3-46).

$$G_{Vc}(z) = \frac{37.33z + 0.3505}{z^2 + 0.1076z + 0.02502} \tag{3-46}$$

Using (3-47), MATLAB's PID tuner was used to parameterize the controller and the resultant parameter are shown in Figure 3-13.

Controller Parameters

| | Tuned |
|---|---|
| Kp | 0.00022638 |
| Ki | 0.1811 |
| Kd | n/a |
| Tf | n/a |
| | |
| | |

Performance and Robustness

| | Tuned |
|---|---|
| Rise time | 0.36 seconds |
| Settling time | 0.642 seconds |
| Overshoot | 0 % |
| Peak | 1 |
| Gain margin | 42 dB @ 667 rad/s |
| Phase margin | 89.2 deg @ 6.03 rad/s |
| Closed-loop stability | Stable |

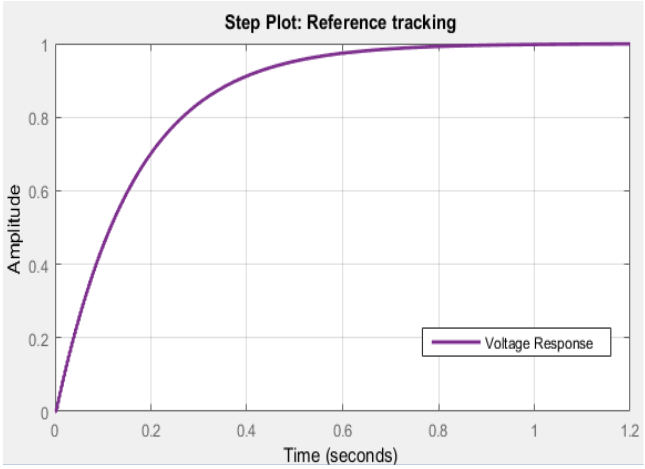


*Figure 3-13. Results of MATLAB controller tuning application for a discrete controller*

The *K(z)* is a Proportional Integral controller and is given by Equation (3-48). The integrator method used was the Forward Euler method.

$$K(z) = 0.00022638 + \frac{0.1811}{400}\frac{1}{z-1} \tag{3-48}$$

Figure 3-14 shows the DC Bus voltage and inductor current during start up for a purely resistive load (Mode 1) and charging with no load (Mode 3). The system can adequately control the voltage levels on the DC-Bus. Now that the system is able to control its output voltage, it must now be able to inject BIS perturbations. This is discussed in the next section.

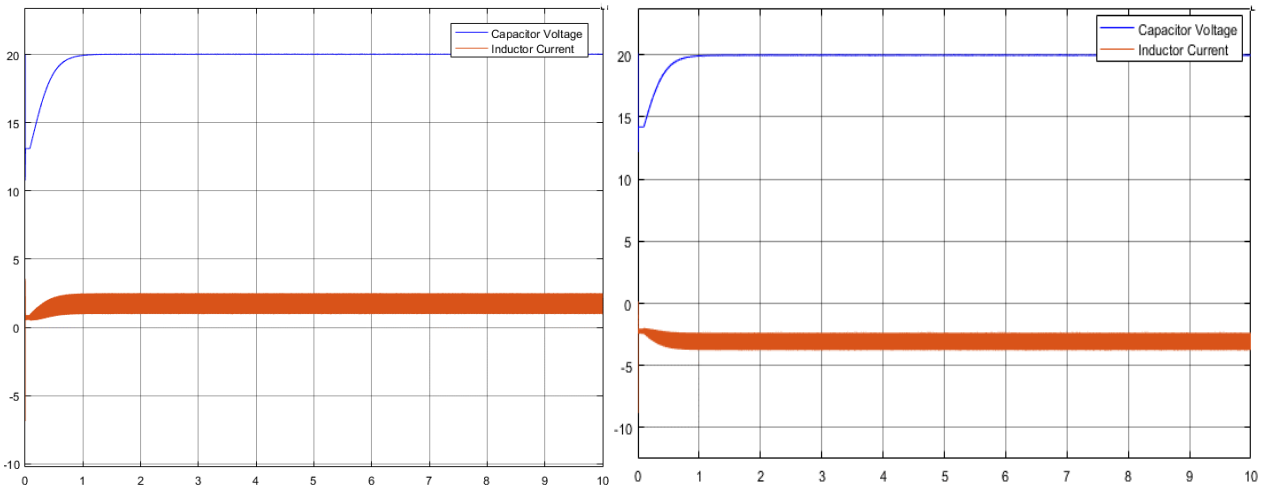


*Figure 3-14. Digital controller (a) Response to resistive load. (b) Response to DC supply*

## 3.6 APPLYING IMPEDANCE SPECTROSCOPY TO THE CONVERTER

The converter can now control the voltage levels on the DC bus. This section designs the control scheme that is used by the converter during BIS signal injection.

### 3.6.1 Condition of Stability

According to the Kramers-Kronig requirement, EIS/BIS should only be conducted periodically during a condition of stability. The condition of stability can be defined as threshold values of the output bus voltage $V_{BUS}$. A similar approach was used by [18]. This threshold value was chosen to be $\pm 10\%$ of the setpoint voltage. This is given by (3-49), where $V_{setpoint}$ is the intended voltage for $V_{BUS}$.

$$90\%\ V_{setpoint} \leq V_{BUS} \leq 110\%\ V_{setpoint} \tag{3-49}$$

If the voltage of $V_{BUS}$ is outside of the threshold limits, the BIS measurement should stop, and voltage control must be reinstated. The threshold voltage can be adjusted depending on how strict the voltage requirement is on $V_{BUS}$ During the suspension of voltage control there is only feedforward control of the inductor current $I_L$. The first section investigates how the BIS perturbations are injected when voltage control has been suspended.

### 3.6.2 Injecting Current Perturbations

Once voltage control of $V_{BUS}$ has been suspended, the converter needs to vary the duty cycle to inject the BIS signals. The relationship ($G_{IL}$) developed in Section 3.3 indicates how current signals relate to the duty cycle. Rearranging $G_{IL}$ in terms of duty cycle yields and substituting s = $2\pi fi$ results in equation (3-50).

$$\tilde{d}(f) = \tilde{\imath}_L(f)\frac{(2\pi fi)^2 + \left(\frac{(R_L + R_{bat})}{L} + \frac{1}{R_{LOAD}C}\right)(2\pi fi) + \frac{(R_L + R_{bat})}{R_{LOAD}LC} + \frac{(1-D)^2}{LC}}{\frac{1}{L}V_c(2\pi fi) + \frac{V_c}{R_{LOAD}LC} + \frac{(1-D)}{LC}I_L} \quad (3\text{-}50)$$

This equation can be used to calculate the duty cycle perturbation $\tilde{d}(f)$ required to produce the current perturbation $\tilde{\imath}_L(f)$. Assuming that $L, C, R_L, R_{bat}$ *and* $R_{LOAD}$ are known values, as well as, the list of required current perturbations ($\tilde{\imath}_L$) to inject, then, only the DC value of the output of the inverter $V_c$, the DC value of the inductor current $I_L$ and the DC value of the duty cycle (D) are required to be measured to produce the duty cycle perturbations required for the IS measurement.

For instance, after the stability condition on $V_{BUS}$ is met, if $V_c$ = 20, $I_L = 2A$ and $D = 0.5$, and the first frequency to be injected is 0.1A at 10Hz, the sinusoidal duty cycle perturbation required to produce this current perturbation is given by:

$$\tilde{d}(f) = 0.00882313 \ @ \ -0.168532\ rads$$

This was further investigated using simulation with frequencies between 1 and 2048Hz. Sub-hertz frequencies were not investigated in simulation to reduce simulation time of sub-hertz measurements in Matlab Simulink[7]. The multi-sine perturbation signal that was used was a BIS summation of sine signals that was developed at the beginning of this chapter. Where $f_n$ = [1,2,4,8,16,32,64,128,256,512,1024,2048]. The full $\tilde{\mathrm{d}}_{BIS}$ is given by the equation:

$$\tilde{\mathrm{d}}_{BIS} = \sum_{n}^{N-1} \tilde{d}(f_n)$$

In order to calculate the impedance of the injected perturbation, the inductor current and battery voltage response had to be measured. This is addressed in the following section.

[7] Note that the sub-hertz frequencies are tested on a running system in Chapter 5.

### 3.6.3 Measuring Injected Signals

It is important that voltage/current response is sampled adequately using an appropriate Analog to Digital Converter (ADC). The measured data are the voltage and current signals in the time domain. However, to get a Nyquist plot, we need to look at the frequency response of the system at various frequency points. Thus, a conversion from the time domain to the frequency domain must take place. This is achieved using a Fast Fourier Transform (FFT). The FFT is computed by taking the Discrete Fourier Transform (DFT), because the sampled signal is a set of discrete values of length $N$. This results in a set of frequencies of length $N$, in the frequency domain. It should be noted that, there are limitations with using the FFT. This is because a true Fourier Transform measures an infinite continuous signal, however it is only possible to measure a finite signal. This causes a discontinuity in the signal resulting in high frequency components that are not present in the original signal. This can be minimized by using a window function to minimize the amplitude of the discontinuities at the boundary of the signal. It works by multiplying the sampled signal by a finite-length window with an amplitude that, varies smoothly towards zero at the edges. The recommended window for a signal that contains multiple sine waves and where amplitude accuracy is essential is the Hann window function [49].

It is theoretically possible to obtain the EIS in one measurement cycle (M). However, it is practically better to measure over more than a single cycle to ensure the system is not in a transient condition [23]. Reference [23] found that M=5 gives an excellent cycle number to be used, when optimizing memory storage, accuracy, and speed, while, reference [3] used a lower value of M=3. From experimentation, M=2 was also found to produce satisfactory results. Therefore, when the lowest frequency was $f_0 = 0.02\ Hz$, the BIS measurement took 100 seconds, and when the lowest frequency was $f_0 = 1\ Hz$, the BIS measurement took 2 seconds.

### 3.6.4 Filters

Another issue to be addressed is the high switching frequency component in the frequency spectrum created by the $20kHz$ switching rate. A low pass filter is required to filter out the high switching frequency, while still allowing the frequencies of the injected BIS signal to pass through. Ideal filters, filter out all frequencies outside the cut-off frequency, and allows all other frequencies through the passband with no change in amplitude or phase. Practically, this is not achievable and thus, there are several types of filters to achieve required trade-offs

[50]. The most common filter configurations are given in Table 3-3 indicating the pros and cons of the different filter configurations.

Table 3-3. Filter types, Pros and Cons [50]

| Filter Type | Pros | Cons |
|---|---|---|
| **Butterworth** | Maximum-magnitude-response. | Slow Transient response<br>Moderate overshoot and ringing |
| **Bessel** | Excellent phase and transient response | Ripple in pass band<br>Rate of roll-off is reduced |
| **Chebyshev** | Steeper roll-off | Ripple in passband |

It is desired that the magnitude of the measured perturbation is as accurate as possible. Thus, a Butterworth filter was chosen due to its flat passband. The standard second-order low pass filter transfer function is shown in the equation below from [50]:

$$H_{LP}(f) = -\frac{K}{\left(\frac{f}{f_c}\right)^2 + \frac{1}{Q}\frac{jf}{f_c} + 1} \tag{3-51}$$

For a 2nd order Butterworth filter, the Q value = 0.7071. Therefore, for a unity gain Butterworth 2nd order low pass filter, fc = 8kHz. The equation reduces to the following second order transfer function:

$$H_{LP}(f) = -\frac{1}{-\left(\frac{f}{8000}\right)^2 + 1.414\frac{jf}{8000} + 1} \tag{3-52}$$

This filter will be applied to both $I_L$ and $V_{bat}$measurements.

### 3.6.5 Simulations of the DC-DC converter

Simulink was used to simulate BIS on the converter. This section describes how the simulation was achieved.

#### *I. Battery Model*

To produce, realistic results in simulation, a simple Thevenin battery model was used. The model contains a single Li-Ion cell modelled as a voltage source, a series resistor and a resistor capacitor in parallel, connected to another voltage source $V_{bat1}$, which represents the other batteries in the pack. Thus, the voltage is only measured across a single cell in the simulation. This was done to reduce computational effort for the simulation. Also, a simpler

model of the Li-Ion battery was used for the simulation for 2 reasons; firstly, Simulink does not contain more complicated components such as the Warburg Element or CPE elements as found in most Li-ion battery models and secondly, the inclusion of additional high time constant capacitors increases the simulation time considerably.

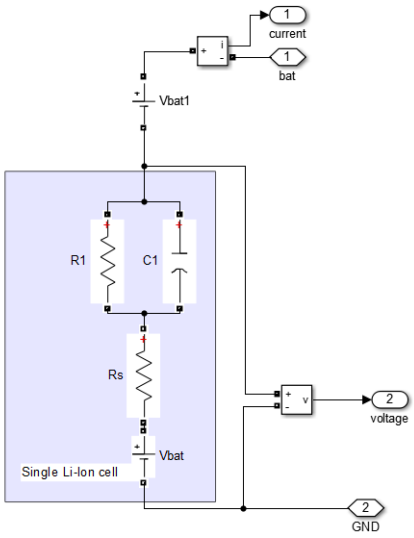


*Figure 3-15. Battery Model*

The values that were used for the components were taken from the step test performed on the Li-Ion cell[8]. These values are shown Table 3-4.

Table 3-4. Parameters obtained from Step Response

| Parameter | Value |
|---|---|
| $V_{bat}$ | 4V |
| $R_s$ | 0.002 |
| $R_1$ | 0.0012 |
| $C_1$ | 55.7 |

### *II. Controller*

To perform BIS using the converter, it is essential to be able to detect, if the converter was operating in a stable region and suspend voltage control as well as to inject and measure BIS signals, and then reinstate voltage control. If at any point, the voltage on the *DC Bus* is unacceptable, the measurement should be stopped, and voltage control should be reinstated. The controller performs voltage control using a PI controller.

[8] See Appendix A1 for step test performed on Li-Ion cell

The PI controller then feeds into a MATLAB function block. The function takes in the controller duty cycle, output bus voltage and the battery current. It uses these parameters to determine, if the converter is operating under stable conditions i.e. if the output voltage is within the thresholds for a certain amount of time. If a stable condition is detected, the required BIS signals will be calculated and superimposed onto the duty cycle. The voltage control is suspended during this time. The signals are measured using a ZOH, a buffer, a Hanning windowing function and then a FFT is performed. This is shown in Figure 3-16.

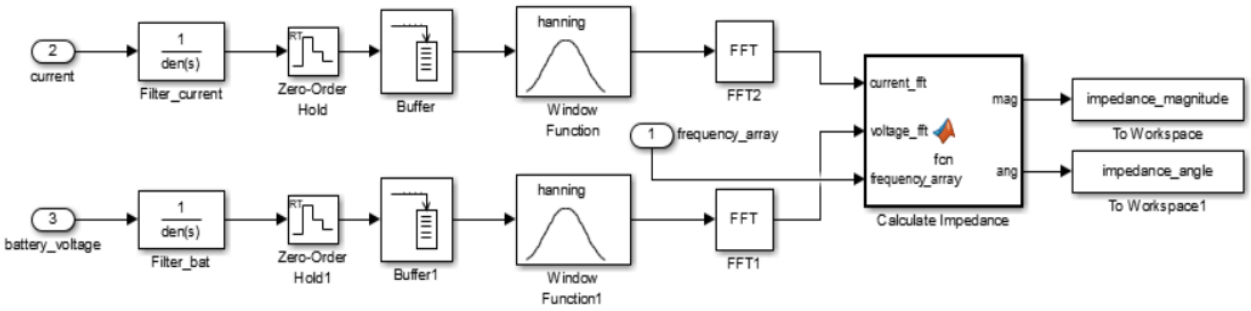


*Figure 3-16. Determining Impedance in SIMULINK*

The filters are effective at filtering out the high frequency signal as can be seen by the following simulation of the current in Figure 3-17, where the yellow signal is the unfiltered $I_L$ and the blue signal is $I_L$ after filtering.

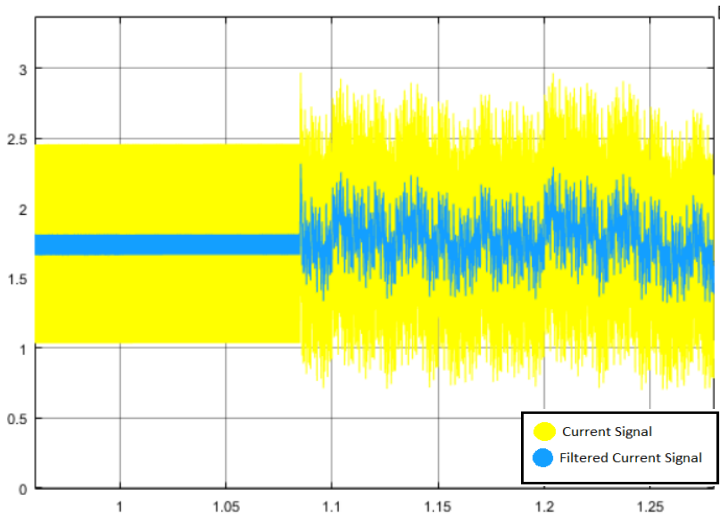


*Figure 3-17. Filtered current response.*

### *III. Impedance Spectroscopy Simulations*

The BIS signal that is being tested in the simulation is a simplified IS signal. The frequency array is created from frequencies between 1 and 2048 kHz. The BIS signal was measured over a period of 2 seconds. Figure 3-18 shows the injected BIS current signal and voltage response.

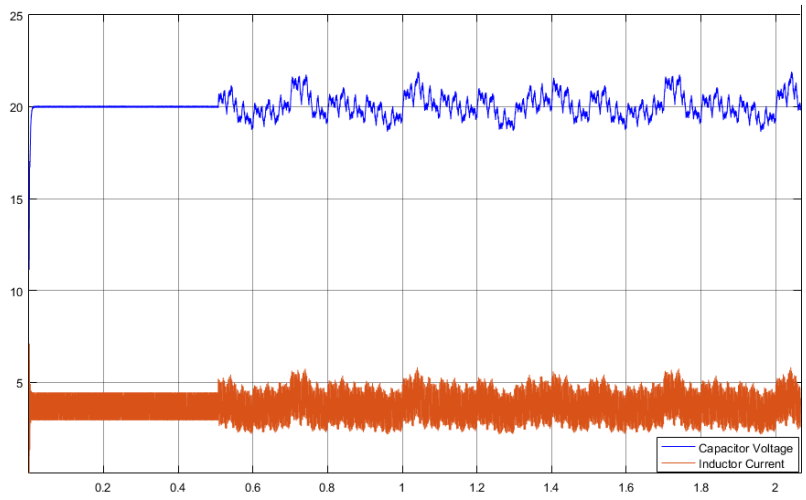


*Figure 3-18. BIS current injection Simulink simulation*

The current waveform is shown in Figure 3-19. The desired current signal is shown in orange, while the yellow is the actual current. The signal contains a lot of noise from the switching frequency. The inductor current is given in orange, the yellow signal is the intended injected current waveform. Figure 3-19 (a) shows the BIS signal and (b) shows the single sinusoid EIS for a 10 Hz signal.

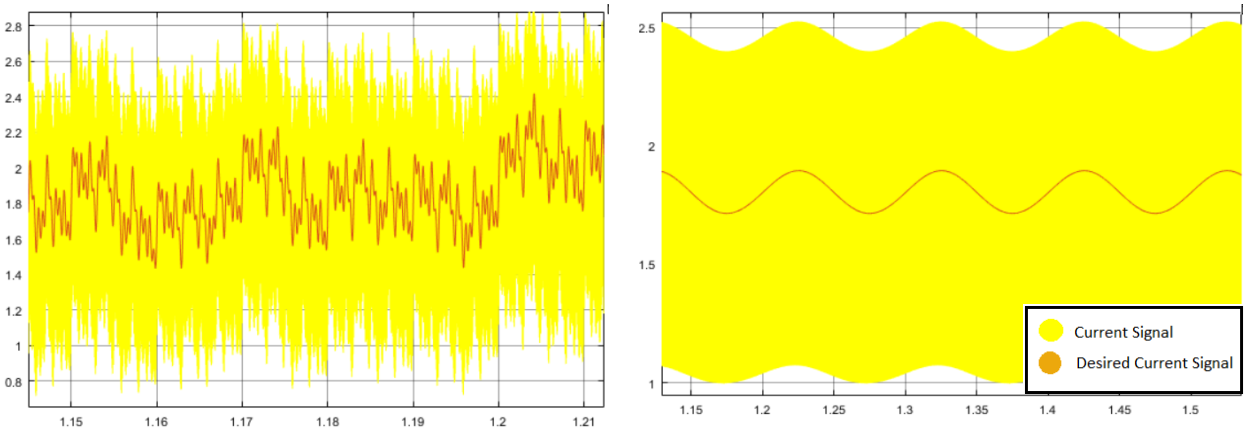


(a) (b)

*Figure 3-19. (a) BIS current injection Simulink simulation (b) EIS 10Hz Inductor Current*[9]

Figure 3-20 below shows the measured inductor current during a BIS perturbation vs the intended inductor current amplitudes. It can be seen they are almost identical. This shows that the feedforward calculation of the inductor currents performed in 3.6.2 works very well in simulations.

[9] Note Figure (a) shows a BIS signal during 1.15 and 1.21 seconds, and Figure (b) shows the EIS signal between 1.15 and 1.55 seconds.

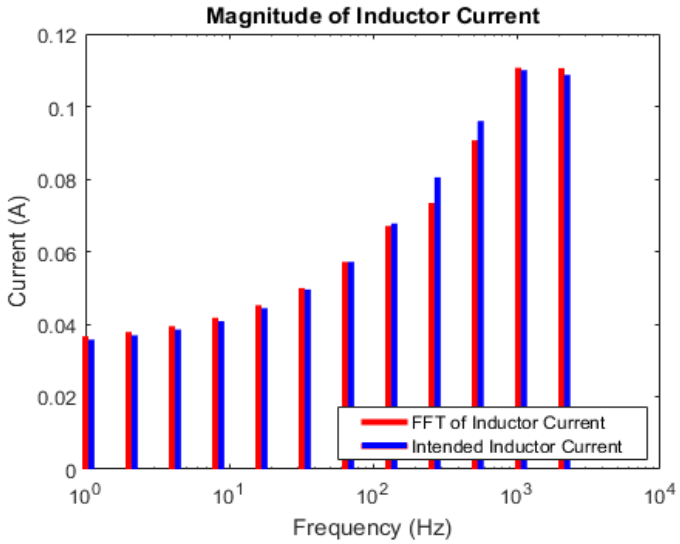


*Figure 3-20. Measured Inductor Current Amplitudes vs Intended Inductor Current*

Using the Get_Impedance block shown in Figure 3-16 on both $I_L$ and $V_{bat}$, a Nyquist and Bode plot of the battery's impedance was then created using the battery current and voltage response and is shown in Figure 3-21. The plots are compared to expected Thevenin equivalent model. The measured response is almost identical to the expected impedance results.

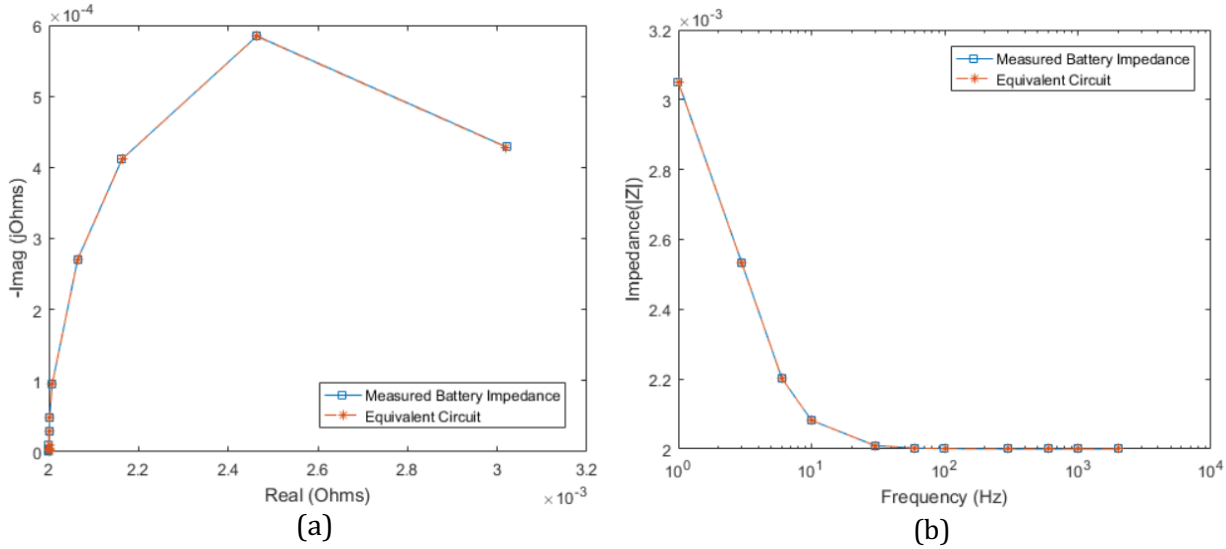


(a) (b)

*Figure 3-21. (a) Nyquist and (b) bode plot of impedance of simplified battery model*

The chapter has been able to demonstrate the analytical modelling, as well as a computer simulation to demonstrate how that the appropriate duty cycle perturbations are determined using small-signal analysis, as well as, a voltage control strategy for the $V_{bus}$. Chapter 5 deals with the experimental implementation of impedance spectroscopy on a running system.

# Chapter 4. EXPERIMENTAL SETUP

This chapter details the experimental setup and test protocols performed on the Li-Ion cells. There are two spectroscopy techniques that are considered in this chapter. The first is implementation of EIS/BIS using a linear amplifier by electronic load control (conventional method), and the second is the use of a switching converter developed in Chapter 3. In this thesis, these 2 major types of IS methods were tested with a focus on using the switching converter method.

The cells that were tested are EIG Lithium-Ion NCM cells.[10] They are 20Ah pouch cells, and have a nominal voltage of 3.65 V, with specifications given in Table 4-1. The cells were charged using a DC power supply and implementing the CC/CV method, first in constant current mode at 10A to a maximum voltage of 4.15 V. At this threshold voltage, the power supply was set to constant voltage until the current reached 0.3 A. The cell was left to rest for 1 hour after charging was performed. This is considered 100 % SoC. The SoC was tracked by using a Coulomb Counting described in Chapter 2.4.3.

Table 4-1 EIG Li-Ion NCM battery specifications

| **Parameter** | **Specification** |
|---|---|
| Cathode | Li[NiCoMn]O2 |
| Anode | Graphite Based |
| Nominal Capacity | 20Ah |
| Nominal Voltage | 3.65 V |
| Max Voltage | 4.15 V |
| Minimum Voltage | 3 V |
| AC Impedance (@ 1kHz) | <3mΩ |

[10] Battery specifications are included in Appendix A2.

## 4.1 IMPEDANCE SPECTROSCOPY USING AN ELECTRONIC CONTROLLABLE LOAD

This method was implemented using galvano-static mode via load variation, similar to the method that was used by [3], [5], [24]. This method used a TTI-LD300 voltage controlled electronic load in constant current mode, to vary the current of the battery via sinusoidal perturbations to obtain impedance measurements for the battery (Figure 4-1).

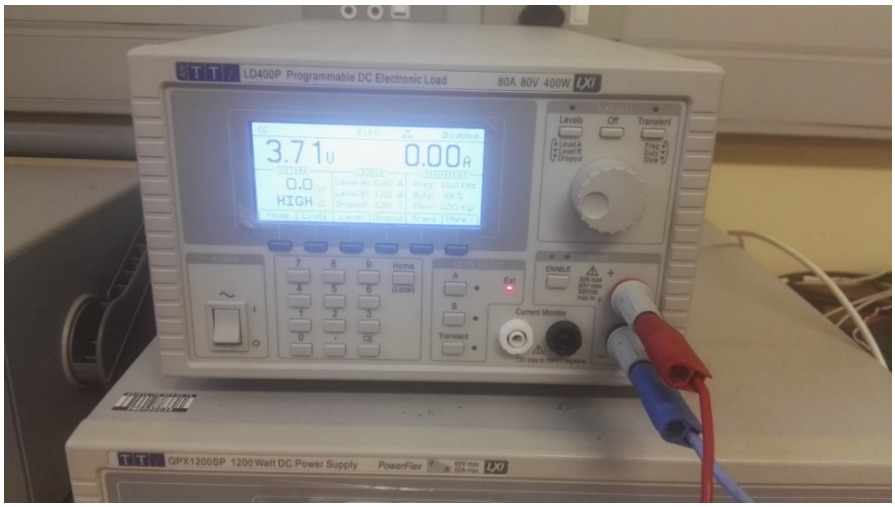


*Figure 4-1. Voltage controlled electronic load*

The electronic load can be operated in different controlled modes. The Constant Current (CC) mode can be used to set the current using a voltage-controlled input signal. It also measures the current at the output and provides a current measurement signal. Both the current setpoint signal and current output signal was connected to the NI-6366 USB device using BNC cables. The NI-6366 USB device is shown in Figure 4-2. Note that, the NI-6366 USB device will be referred to as NI-DAQ for the remainder of this dissertation. The NI-DAQ has an ADC resolution of 16 bits and a maximum sampling rate of 2MS/s.

The current drawn by the load is controlled by a current setpoint signal $i_{\_control}(t)$, which contains the DC setpoint and the frequencies that are superimposed. The $i_{\_control}(t)$ signal is produced on LABVIEW and interfaces the load via the NI DAQ device. This device acts as a digital to analogue converter (DAC) as well as an analogue to digital converter (ADC).

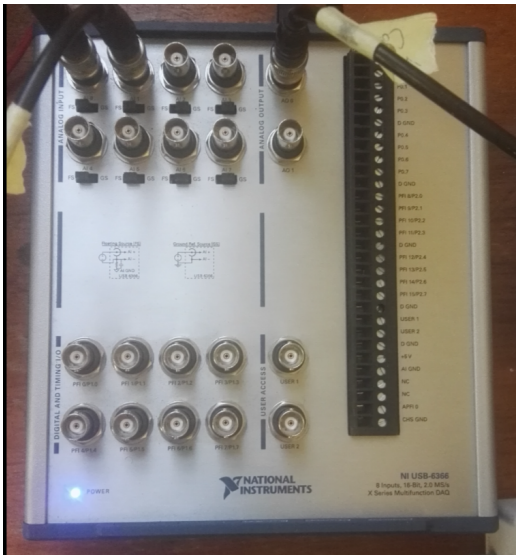


*Figure 4-2. NI-6366 USB data generation/acquisition device (NI-DAQ)*

$V_{bat}(t)$ was measured at the terminals of the Li-Ion cell and the current, $I_{bat}(t)$ was measured directly from the electronic load. A FFT was then performed on the $V_{bat}(t)$ and $I_{bat}(t)$ signals in LABVIEW and the impedance was calculated at each injected frequency. All signal processing was done in LABVIEW. A schematic of the experimental set-up is shown in Figure 4-3 and actual set-up in Figure 4-4. Note that, only one Li-Ion NCM cell was tested at a time, and this experiment tested IS through linear injection and not using a DC-DC converter. The setup for the single sinusoid EIS method and multi-sine BIS method is the same, the only difference is the LABVIEW code for the signal type and signal analysis.

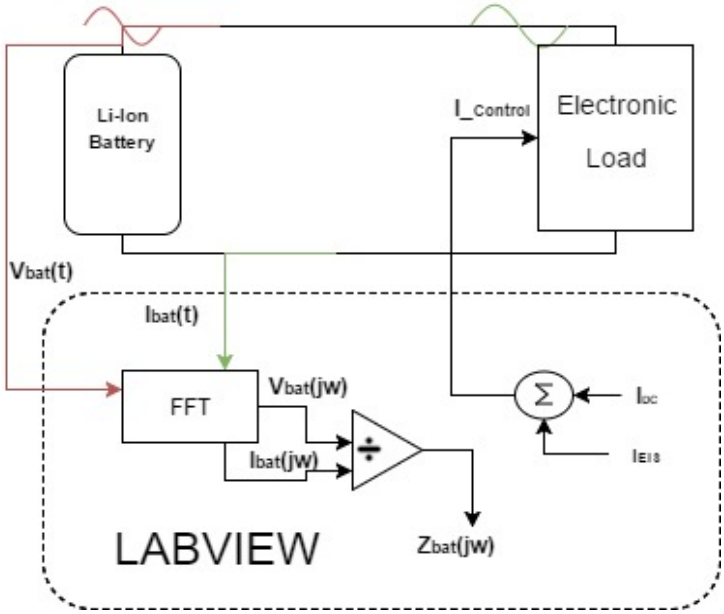


*Figure 4-3. Diagram of varying an electronic load to perform EIS/BIS*

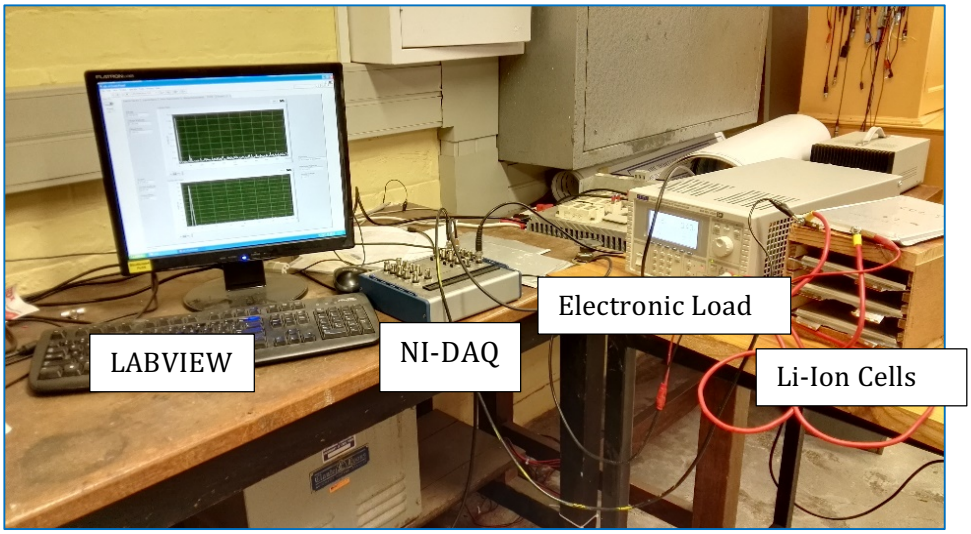


*Figure 4-4. Experimental setup for Impedance Spectroscopy using an electronic load*

### 4.1.1 EIS using an Electronic Load

In order to compare the BIS signal on the electronic load, a conventional EIS signal was also tested. A single sine EIS signal can be represented as given in (4-1). It contains a DC setpoint, $I_{dc}$ and a current perturbation at a frequency, $f_n$ which were the same values used for the BIS signal that was designed in Chapter 3.

$$I_{bat}(t) = I_{dc} + I_n sin(2\pi f_n t) \tag{4-1}$$

It is important that, the battery's SoC does not change significantly during measurement, therefore, the DC current set-point was maintained constant throughout the measurement at $I_{DC} = 0.5A$. The frequencies are between 0.02 Hz and 2kHz and the amplitude $I_n$ was chosen to be 10% of the batteries $I_{DC}$ for all frequencies ( $I_n = 0.05A$).

The NI-DAQ was controlled by LABVIEW. The LABIEW Code had 2 sections, signal generation and signal acquisition. To generate the sine wave required, the code uses a sine wave generator that takes in a value for frequency, offset and amplitude. The signal acquisition part of the code takes in 2 arguments from LABVIEW, the sample rate and sample number. This results in an array of samples from the DAQ. This array, represents discrete time points from the voltage and current measurement. A Discrete Fourier Transform (DFT) is then performed on the array and converts the time domain signal into the frequency domain for analysis. The amplitude and phase of the injected frequency are obtained from both the voltage and current measurements. The impedance is given by the division of the current from the voltage as given in (4-3).

$$Z_f = \frac{DFT(v(t))}{DFT(i(t))} \tag{4-2}$$

### 4.1.2 BIS using Electronic Load

The LABVIEW code that was used was similar to that used in the EIS procedure, except that, it uses a multi-tone generator in LABVIEW. The multi-tone generator takes in 3 inputs. A frequency array, amplitude array, phase array. The data acquisition was the same as for the EIS measurement, however, the analogue input sample rate range was set at 20 000 S/s and 2MS with a total measurement time of 100 seconds. Figure 4-5 shows an example of the output of the Nyquist and Bode plot on LABVIEW of the multi-sine BIS measurement.

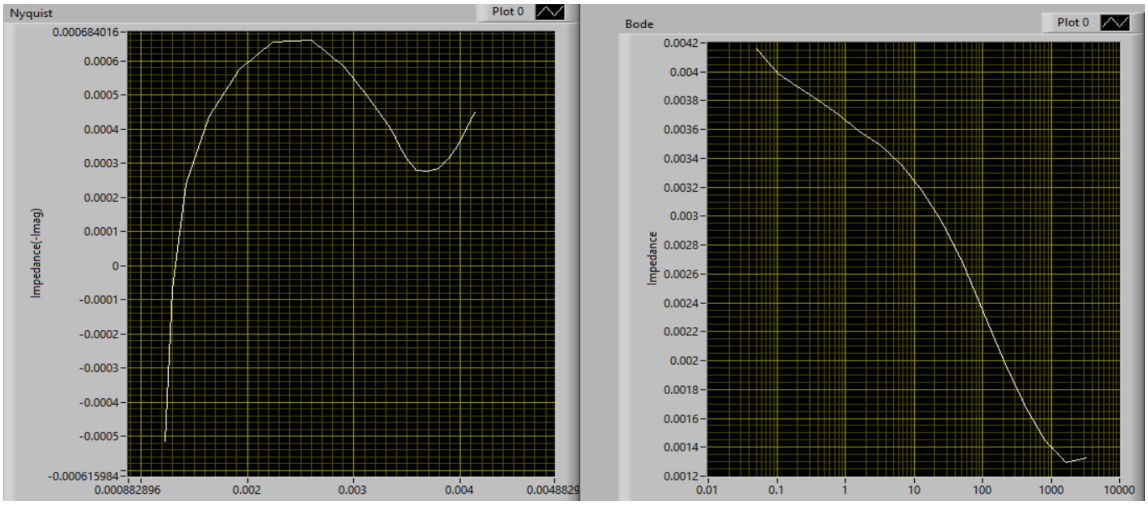


*Figure 4-5. Example Nyquist and Bode plot from BIS test on Li-Ion battery*

The procedure was carried out at different battery SoCs and DC bias currents. The Nyquist plot at 50% and 100% SoC was obtained in order to test the IS procedure. All measurements were taken at 0.5A. This was found to be a good DC bias current which was large enough to superimpose the BIS signal but small enough to not affect the cell's SoC significantly. This section detailed the experimental methodology used to obtain the Nyquist impedance plot of the Li-Ion cell using a controllable linear amplifier (load). The next section details the construction of the DC-DC converter that will be used in the switching converter IS measurements.

## 4.2 CONSTRUCTION OF SWITCHING CONVERTER

The converter had to be built using the specifications given in Chapter 3. This section details the construction of the DC-DC converter, PWM generation, control of the MOSFETs and the measurement circuitry for the current and voltage measurements.

### 4.2.1 DC-DC Converter

A very important component of the converter is the switches. The MOSFET that was chosen was the 5th generation IRFP260N International Rectifier Power MOSFET. This MOSFET has a low on-state resistance (0.04 Ohms) and high current capability of 50A (@ 25 degrees C). The MOSFET contains a body diode that has a forward voltage drop of 1.3V. [11]The bi-directional DC-DC converter was built onto a PCB. The PCB was placed on a heatsink to dissipate the heat from the MOSFETs (See Figure 4-6).

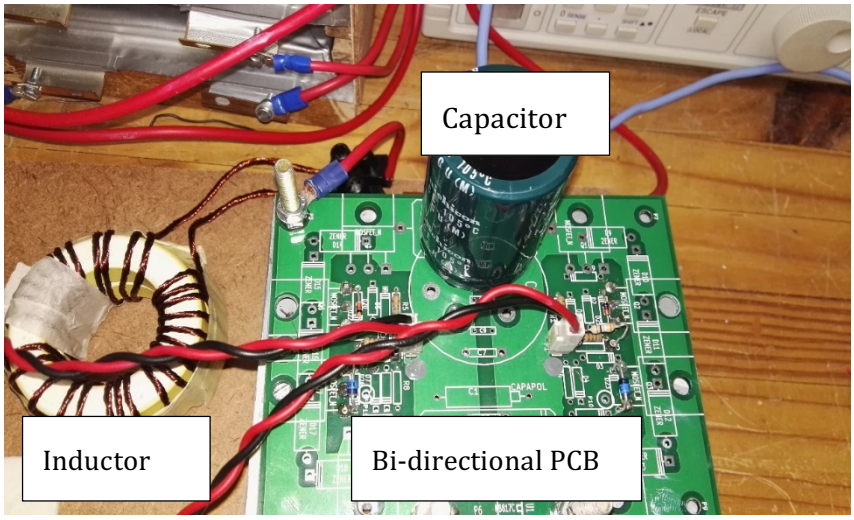


*Figure 4-6. Bi-directional boost/buck converter*

The inductor had a total resistance of 0.2 Ohms and an inductance of 170uH. The output filter capacitor that was used was 440uF.

### 4.2.2 Drive Circuitry

The drive circuitry is responsible for converting the duty cycle to a PWM switching signal, and then driving the MOSFETs S1 and S2 as shown by the block diagram in Figure 4-7. The system takes in the desired duty cycle signal, converts it to a PWM signal using a PWM generator, transmits this signal to the MOSFET driver, and then outputs the signal to the high switch and the low MOSFET switches.

[11] All MOSFET values come from the datasheet by International Rectifier in reference [57]

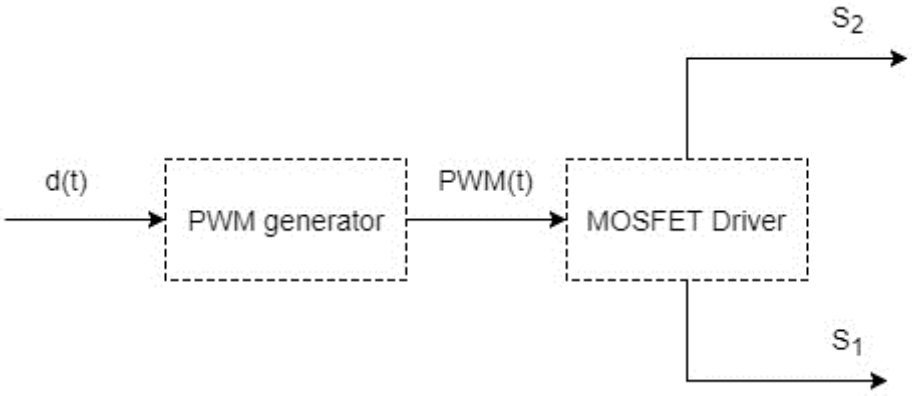


*Figure 4-7. Systems representation of the drive circuitry*

### *I. PWM Generator*

A PWM signal can be produced in 2 ways, either by analogue electronics or digitally using a microcontroller. Analogue PWM generation was chosen, since a considerably high output rate is required from the microcontroller to inject small perturbations into the converter using digital PWM generation. This increases the cost of the microcontroller. If the microcontroller is not responsible for PWM generation, then cheaper microcontrollers can be used. The microcontroller only needs to output a value for the duty cycle $d(t)$.

The PWM waveform is produced by comparing a triangular waveform, at the desired switching frequency $f_{sw}$, to a duty cycle setpoint. The microchip selected for generating the triangular wave was the XR-8038A precision waveform generator from EXAR. This has high triangle wave linearity and is used for precision waveform generation. It produces a triangular waveform that has a voltage peak to peak value which is a third of the supply voltage. The PWM waveform was generated by comparing the triangular waveform to a voltage setpoint which represents the duty cycle, to achieve this, a comparator was needed. The comparator that was chosen was the LM311. Figure 4-8 shows the schematic of the PWM generating scheme.

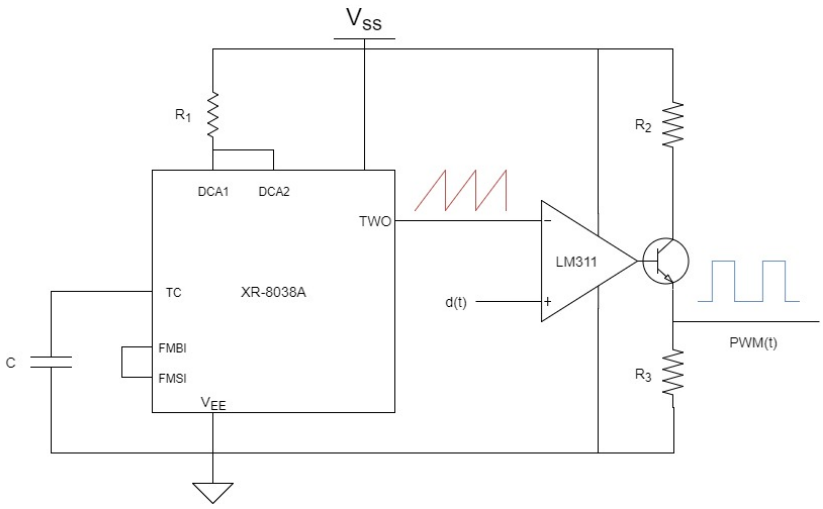


*Figure 4-8. Schematic of the PWM generating scheme*

The timing of the PWM waveform was set by adjusting $R_1$ and $C$ as given in (4-3)[12]:

$$f_{sw} = 20kHz = \frac{0.15}{R_1 C} \tag{4-3}$$

Therefore, the RC time constant would need to be:

$$R_1 C = \frac{0.15}{20000} = 7.5 \times 10^{-6} sec \tag{4-4}$$

Therefore, if $C = 10nF$ then $R_1 = 750\ ohms$ were chosen for the timing components. The triangular waveform has a peak value of 6.5 $V$ and a trough value of 3.5 $V$, therefore the duty cycle input was scaled between these two values, with % 0 duty cycle being at 3.5 V and 100% duty cycle being at 6.5 V.

### *II. MOSFET Driver*

The second part of the drive circuitry, is the circuit that interfaces the PWM waveform to the MOSFETs. The MOSFETs are being driven synchronously, such that the PWM waveform that is used for switching the 2 switches are inverted versions of each other. There are several challenges that are associated with this configuration. Firstly, it should be assured that $S_1$ and $S_2$ are not switched-on at the same time. This condition is known as "shoot through" and thus there must be a certain amount of "dead time" between switching. The second issue is that, the high-side switch ($S_2$) drive needs to be turned on with a voltage greater than the source. To achieve both requirements, a standard MOSFET driver IRS2108 chip by International Rectifier was used. It can supply up to a 20V gate driving signal for both the high switch and

[12] Equation obtained from the XR-8038A datasheet from EXAR

low switch using a bootstrap capacitor. A dead-time was set using a timing resistor (See Figure 4-9).

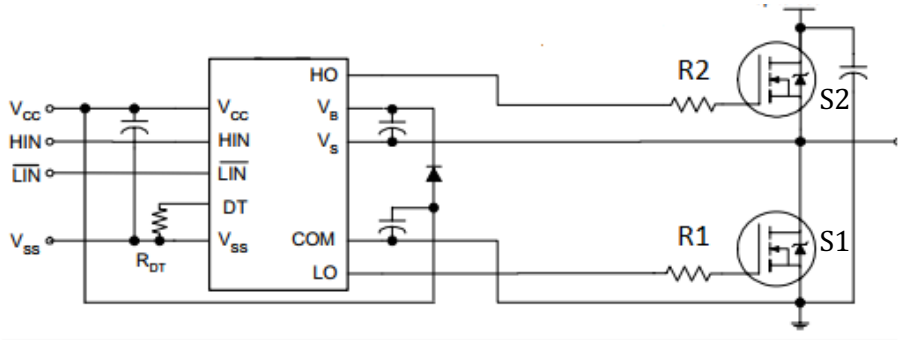


*Figure 4-9. IRS21084 Connection diagram [51]*

It is also common to isolate the signal circuitry to the MOSFET driving circuitry. Therefore, an isolated power supply was used to power the IRS21084 chip and an opto-isolator was used to inject the high and low signals. The 6N137 was selected as the opto-isolator. The MOSFET driver board used was a standard development board from the Power Engineering Laboratory of the University of Cape Town.

### 4.2.3 Current and Voltage Measurement

Current and voltage are measured by the controller for 2 reasons, (i) converter voltage control, and (ii) impedance measurements. For a complete IS procedure using the switching converter, 3 system variables must be measured, the output voltage $V_c$, inductor current $I_L$ and each battery voltage $V_{bat}$. This section details the circuitry designed for these measurements.

#### *I. Filters*

For Impedance Spectroscopy, the voltage and current perturbations of the battery had to be accurately measured by the NI-DAQ. The converter has a high switching frequency (20 $kHz$) and thus interferes with the measurement. It is desired that the switching frequency component be reduced significantly to increase measurement accuracy of the injected perturbations. In this thesis, a butter-worth filter was designed using the filter transfer function derived in Section 3.6.4. The low pass filter that was chosen was the unity-gain Sallen-Key active low pass filter. A second order unity gain Sallen key filter is shown in Figure 4-10. The advantage of this topology is that it can be cascaded to create higher order filters.

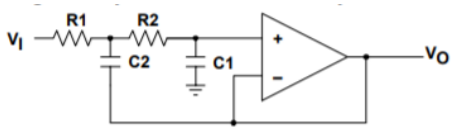


*Figure 4-10. Unity-Gain Sallen-Key [52]*

The following equations were used to obtain appropriate resistor and capacitor values for the Butterworth filter [50].

$$R_1 = mR_2\,, C_2 = nC_1$$

$$Q = \frac{\sqrt{mn}}{m+1} = 0.7071\,, f_c = \frac{1}{2\pi RC\sqrt{mn}} = 8000\ Hz$$

$$m = 1, n = 2,$$

$$R_2C_1 = \frac{1}{8000\times 2\pi\sqrt{2}}$$

$$If\ C = 10nF, R = \frac{1}{10\times 10^{-9}\times 8000\times 2\pi\sqrt{2}} \approx 1400\ Ohms$$

A 1.2 $kOhm$ resistor was chosen for simplicity. Therefore, the cut off frequency is now 9.38 $kHz$. The filter circuit was simulated on LT-SPICE. The 2nd order configuration was cascaded to achieve a higher order and therefore a steeper roll-off. The circuit diagram is shown in Figure 4-11 below.

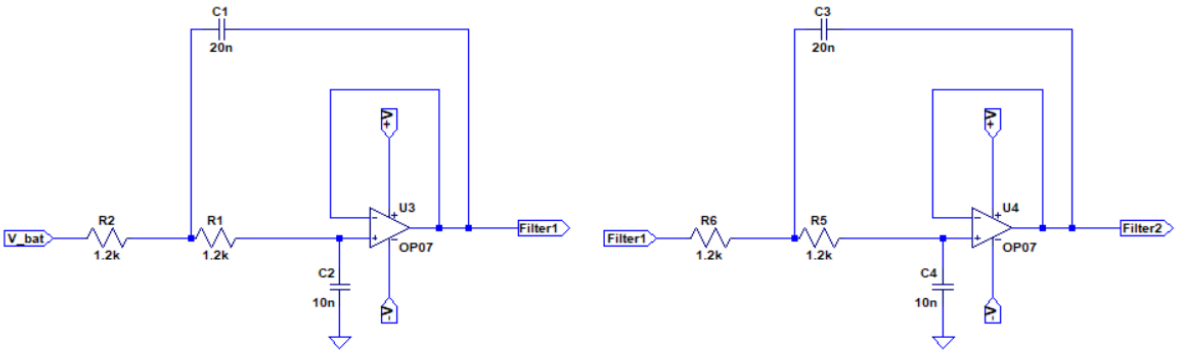


*Figure 4-11. LTSPICE diagram of 4th order butter-worth active low pass filter*

The AC response was then measured over a wide range of frequencies to validate the filter. The voltage magnitude response and phase response are given by Figure 4-12 below. The blue line is the 2nd order filter's magnitude and phase response, the red line is the output of the 4th order cascaded 4th order Butterworth filter.

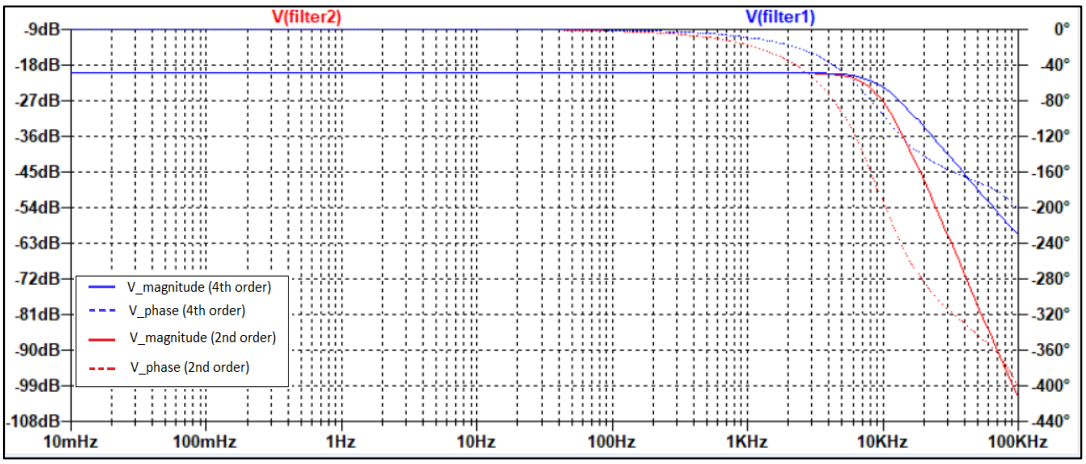


*Figure 4-12. Magnitude and phase response of low pass filters*

The following diagram shows the inductor current signal $I_L$, before and after the filter application. The 20-kHz switching component is almost completely removed.

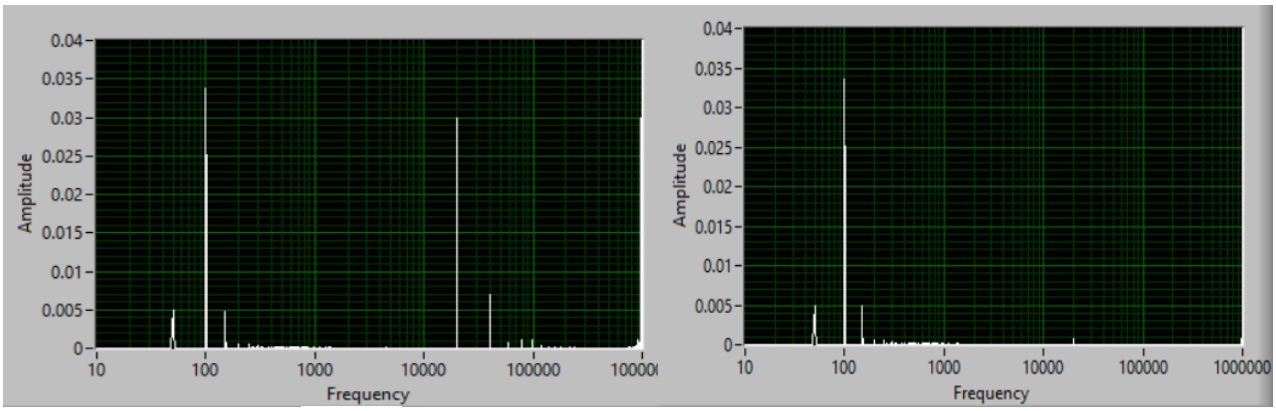


(a) (b)

*Figure 4-13. Frequency response of Butterworth filter (a) before (b) after*

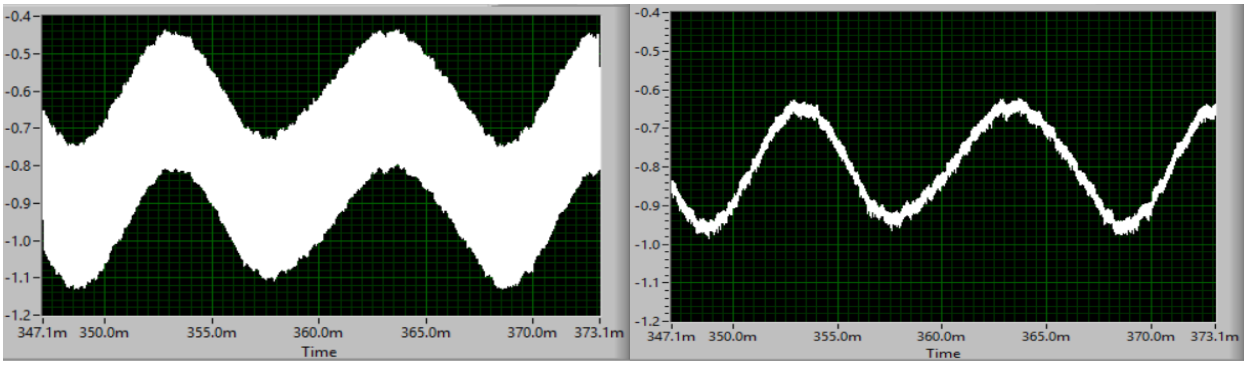


(a) (b)

*Figure 4-14. Time domain response of Butterworth filter (a) before, (b) after*

### *II. Inductor Current measurement*

The inductor current $I_L$ was measured using a LEM LA55 current transducer. It uses the Hall effect to measure current. It has a conversion ratio of 1:1000 and requires a supply voltage of +-15V. A 1 $kOhm$ resistor was used at the output of the LEM module to produce a voltage which represents the current. This meant there was a 1:1 relationship between voltage that was measured and current. i.e. when the inductor current equals 1A, a voltage of 1V appears across the LEM output. This was connected to the filters designed in the previous section. The LEM module and filters were supplied by a MORNSUN Isolated +15/-15 supply. See Figure 4-15.

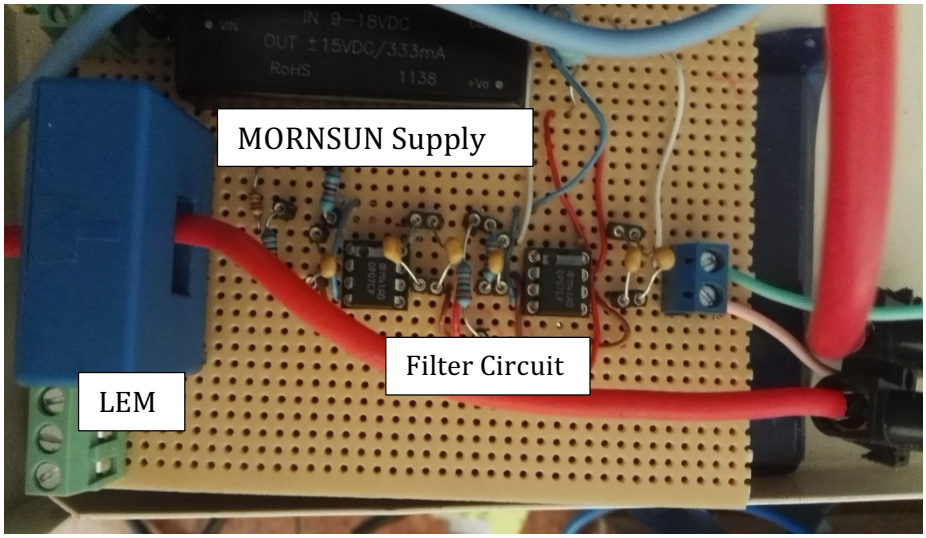


*Figure 4-15. Current measurement and filter circuit*

### *III. Voltage measurement*

The voltages of interest are the output voltage $V_c$ and the battery voltages $V_{bat(1,2,3)}$, ie. the 3 battery cells which are connected in series to make up the battery pack. The voltages had to be sampled by the NI-DAQ. For $V_c$, a voltage divider was used at the output of the converter to scale the measurement down such that it could be measured by the NI-DAQ.

For this prototype, there are 3 Li-Ion batteries in series.

### 4.2.4 Overall Bi-directional Converter Implementation

A top view of the converter system is shown in Figure 4-16. The converter system was fitted inside a container.

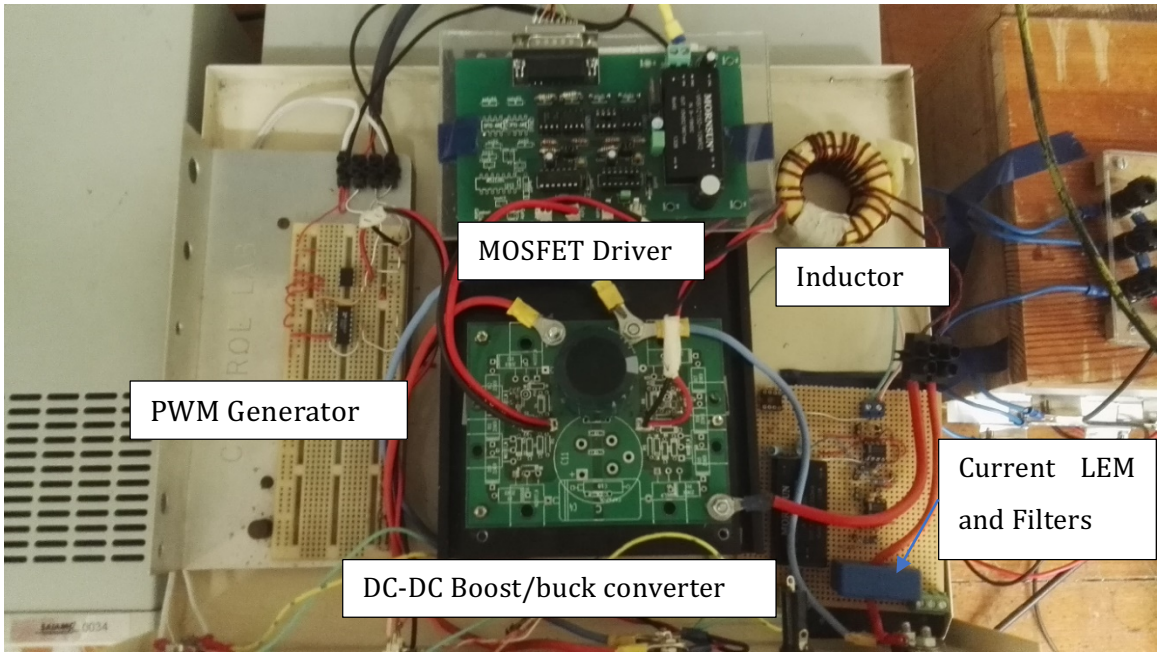


*Figure 4-16. Constructed DC-DC converter*

The external connections to the converter are shown below in Figure 4-17. Starting from the left of the figure, is the 10V DC input that is used by the PWM generator, MOSFET Driver, current LEM Module and filter. The next row consists of the 3 BNC connectors, the first two gives the inductor current output signal and the capacitor voltage signal, respectively. The bottom BNC connector takes in the duty cycle from the NI-DAQ. To the right of these is the connection to $V_{bus}$ and the connection to $V_{bat}$.

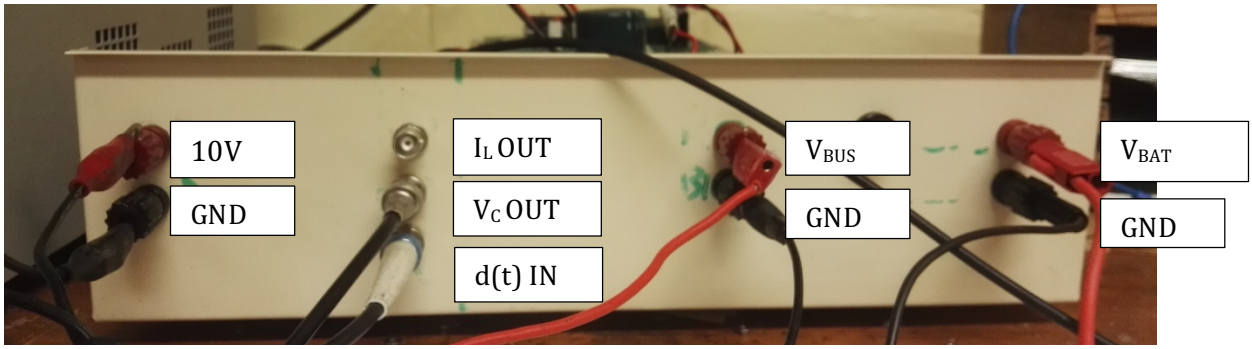


*Figure 4-17. Front panel view of the converter system showing input and output connections.*

## 4.3 IMPEDANCE SPECTROSCOPY ON SWITCHING CONVERTER

This section describes the experimental procedures that was followed on the converter system during experimentation.

### 4.3.1 Experiment Setup

The full experimental setup is shown in Figure 4-18 below. Starting on the left of the diagram is an electronic DC supply that is connected to $V_{bus}$. The electronic supply is connected in current control mode and thus is denoted as $I_{supply}$, which is also connected to $V_{bus}$ of the converter. The electronic supply is also controlled as a wind generator emulator. The Li-Ion cells are next to the DC-DC converter and are connected in series. The NI-DAQ and a PC with LABVIEW are located on the right of the figure. The electronic load is controlled in constant resistance mode.

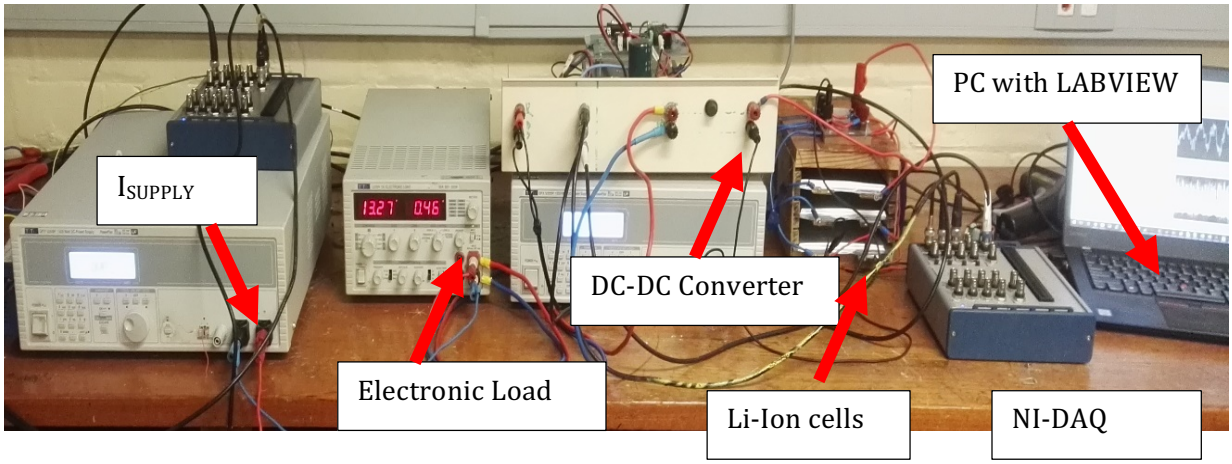


*Figure 4-18. Switching Converter EIS/BIS Experimental Setup*

### 4.3.2 Experimental Procedure

After the converter has reached its setpoint voltage, a BIS measurement procedure is triggered. The flow chart in Figure 4-19 illustrates the BIS measurement protocol on the converter. This procedure was setup in LABVIEW. The first part of the procedure determines if the voltage is stable on $V_{BUS}$ as was defined being within 10% of the $V_{BUS}$ setpoint value (20 V) as discussed in Chapter 4. If the conditions are stable, then the DC values of $V_C$ and $I_L$ are measured and fed into the calculate duty cycles required function. This determines the duty cycles required to produce the desired current perturbations as defined in Chapter 4. The BIS signal is then created, and the perturbations are injected by varying the duty cycle of the converter. While this takes place, $V_C$ is being measured, and if it falls outside its stable

boundary conditions, the measurement is suspended, and voltage control is reinstated. After the BIS measurement is completed, voltage control is reinstated.

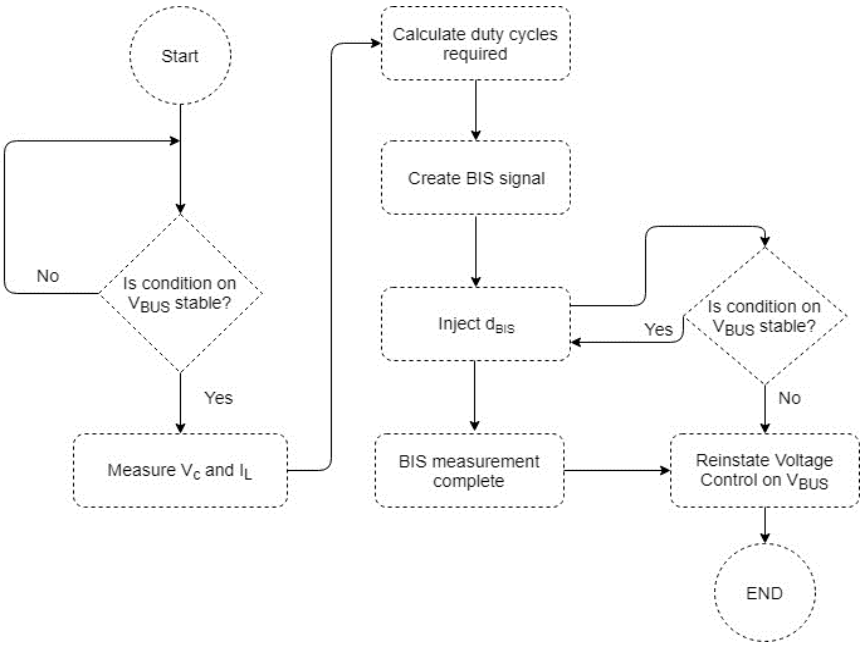


*Figure 4-19. Flow diagram of EIS/BIS measurement*

The BIS signal that was constructed in Chapter 3, which was also used as part of the electronic load experiment, is used by the switching converter, however, it is done in both charging and discharging mode. The DC bias current set-points were also maintained at 1 and 2 Amps for discharging and charging. Figure 4-20 (a) is an example of the calculated BIS perturbation on the duty cycle during a BIS procedure on the switching converter. Figure 4-20 (b) shows the resulting inductor current $I_L$ waveform.

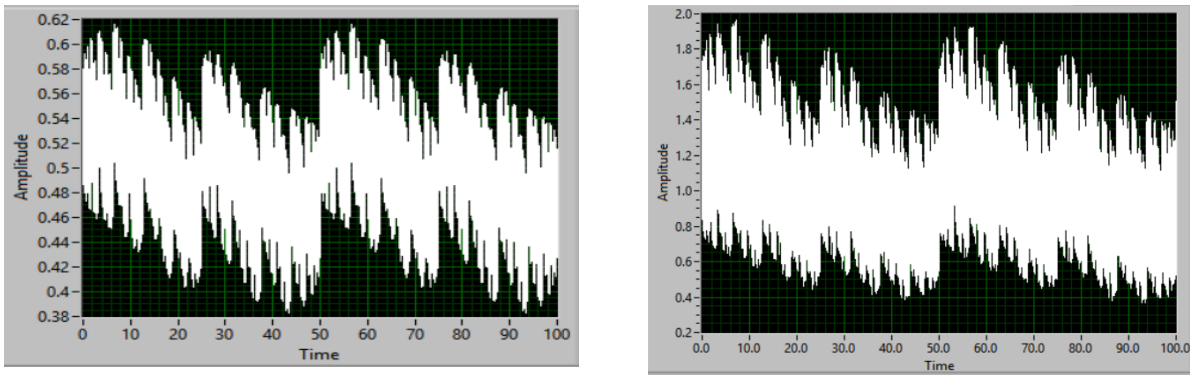


(a) (b)

*Figure 4-20 (a) Duty cycle perturbations, (b) resulting current waveform*

## 4.4 TEST CASE: BIS MEASUREMENTS DURING DC SUPPLY VARIATIONS

This section describes the protocol when attempting to perform a BIS measurement on a system experiencing variability. As an example, the DC supply is replaced with an emulator which mimics a wind generator system. The system is shown in Figure 4-21

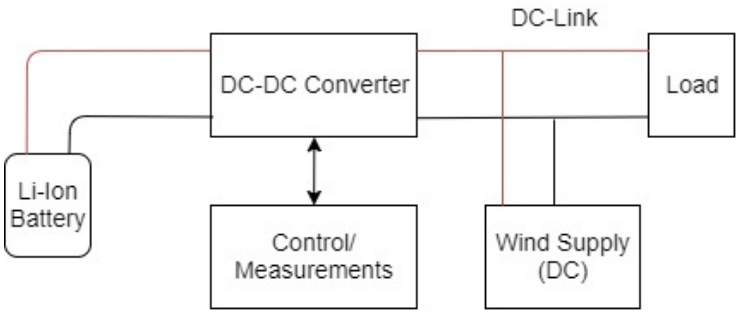


*Figure 4-21. Simplified DC-DC converter system*

In recent years, it has become common to find hybrid distributed generation systems. These systems do not have a constant power output as the wind varies. It is important that this BIS approach used in this dissertation is effective on systems that might experience variability. The variability of renewable energy sources is a prime example of when a system might change.

As a test case, this section explores the use of a bi-directional converter that is connected to a load and a micro-wind generator source and investigates whether BIS can effectively be applied if the wind varies between different speeds. This section does not investigate the limits of the IS procedure under current variation, but shows a practical example of how the system can work under slight current variation caused by a generator system.

To demonstrate this system's ability to conduct IS during power changing events, a simplified wind generator emulator was used. To emulate the wind system, the output current of the power supply was controlled to match the variability of wind. These were simplified into ramp events between different power levels. The output current of the generator emulator is shown in Figure 4-22[13].

[13] Refer to Appendix A5 for full details on how this test current profile was created.

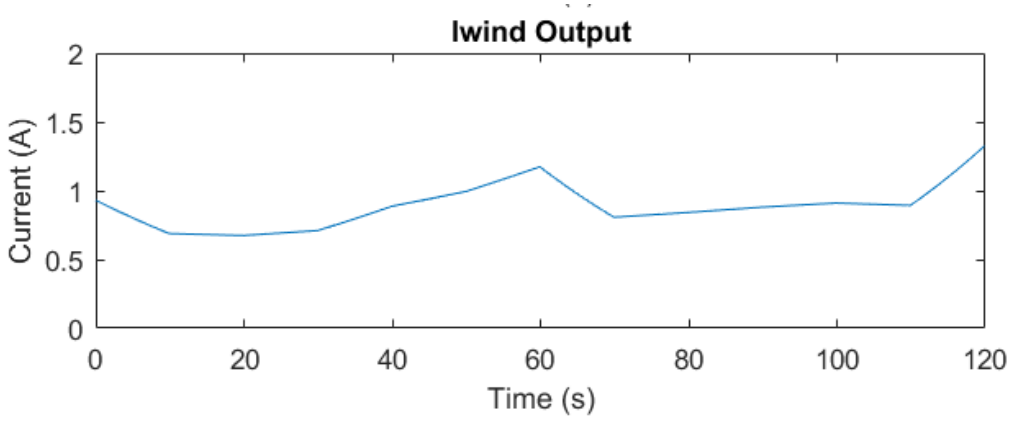


*Figure 4-22. Wind supply emulator current output*

During periods of variability from wind, the current through the batteries would also vary and thus this poses a challenge for BIS signal injection and measurement. The injected signals from the previous section took 100 seconds for measurement. It is possible to reduce this measurement time during periods of instability. This comes with a reduction in low frequency impedance information. Reference [23] showed that it is possible to obtain valuable impedance information with a 1 second measurement. Therefore, the BIS signal can be adjusted to remove all sub-hertz frequencies as was stated in Chapter 3.

The purpose of this section is to demonstrate a practical application of this BIS converter. A full analysis of the amount of load variability that that there can be in order to practically measure the impedance should be conducted in future research.

## 4.5 FREQUENCY RESPONSE ANALYSER AND ERROR ANALYSIS

To validate the results of the experiments, the frequency response analyser (FRA) from AUTOLAB was used to benchmark the results. The NOVA AUTOLAB PGSTAT302N FRA device that was used is shown in
Figure 4-23.

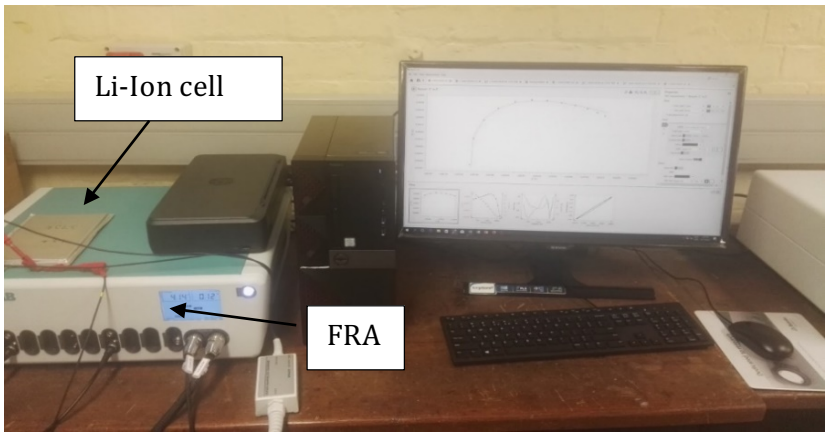


Figure 4-23. PGSTAT302N setup

The FRA measurements were taken using the same frequencies and were performed directly after a BIS/EIS test on the electronic load and switching converter. This was to ensure that the results were comparable to an industry standard method in obtaining impedance. The FRA allowed for charging and discharging measurements with a DC bias current of up to 2 A. The FRA was tested directly after the online measurement. The error in impedance estimation was calculated in terms of absolute impedance using (4-5) for both the DC-Load method and the switching converter varying duty cycle method at 100 SoC and 50 SoC.

$$error_{Z(f)} = 100 \times \frac{|Z_{FRA}(f) - Z_{measured}(f)|}{|Z_{FRA}(f)|} \tag{4-5}$$

The results obtained for both the linear amplification and bi-directional converter techniques are compared and analysed in Chapter 5.

# Chapter 5. RESULTS AND DISCUSSION

The results from the electronic-load IS tests and the switching converter IS tests are compared and analysed in this chapter. The electronic-load experiment could only be carried out for the discharge case, since an electronic-load is used for the signal injection, while the bi-directional converter results are obtained for both charging and discharging scenarios.

## 5.1 IS USING ELECTRONIC-LOAD

The BIS and EIS tests were compared for a Li-Ion cell at 20℃ at a DC bias of 0.5 A as shown in Figure 5-1 (a) for 50% SoC and Figure 5-1 (b) for 100% SoC. The basis of this test was to consider how well the electronic load performs when compared to a standard FRA, and how the BIS signal would compare to the FRA and EIS results.

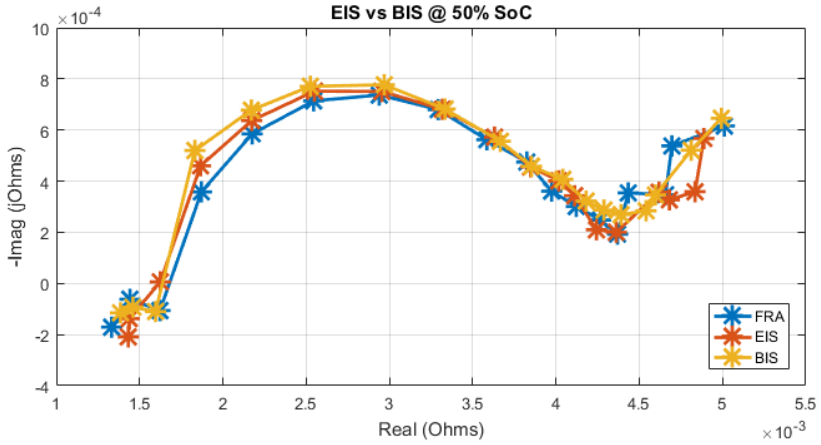


(a)

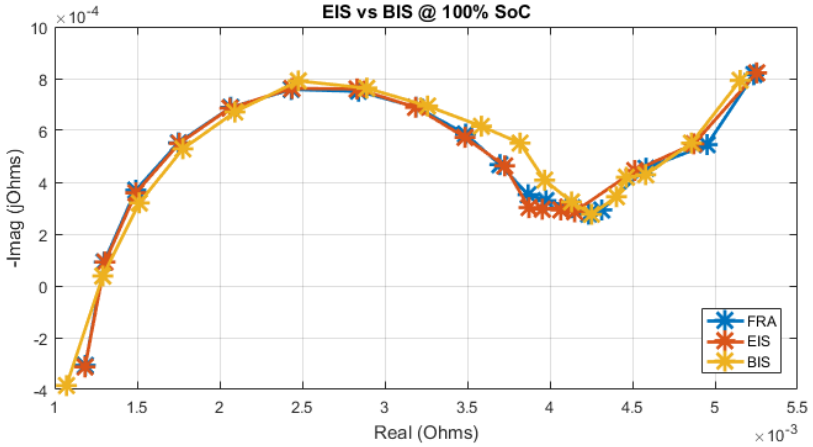


(b)

Figure 5-1. Nyquist plots 0.5 A discharge rate @ 20℃ using the FRA and implementing EIS and BIS on the electronic load for (a) 50% SoC (b) 100% SoC

Another way to visualize the impedance information is using the Bode plot. This is shown in Figure 5-2 below for the Li-Ion cell at 50% SoC and 100% SoC.

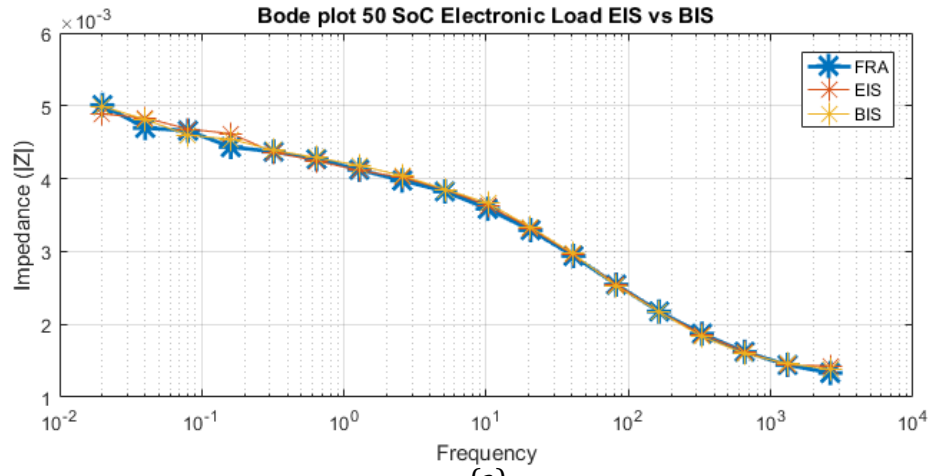


(a)

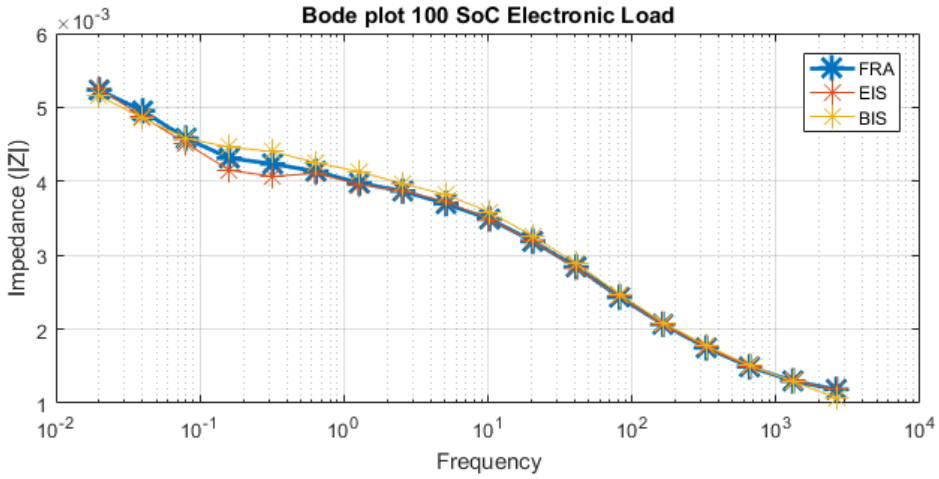


(b)

*Figure 5-2. Bode plot of EIS/BIS on electronic load (a) 100 SoC (b) 50 SoC*

From both the Bode and Nyquist plots, both the EIS and BIS using the electronic load corresponds very well with the FRA measurement. This is confirmed by the error table shown in Table 5-1 below. The errors are in reference to the FRA measurements. The frequencies were subdivided into 3 regions. Frequencies higher than 500 Hz are considered high frequencies, frequencies between 1 and 500 Hz are considered as mid frequencies, while low frequencies are frequencies less than 1 Hz. From the table, the error is less than 3% for both EIS and BIS measurements. In general, the error of the BIS and EIS is quite comparable. This demonstrates that for the Li-Ion cell, the BIS signal performs very similar to the conventional EIS signal.

Table 5-1. EIS vs BIS % error

| SoC | 50 | | 100 | |
|---|---|---|---|---|
| Test: | EIS | BIS | EIS | BIS |
| f< 1 | 1.75 | 1.23 | 1.96 | 2.35 |
| 1< f<500 | 0.72 | 1.07 | 0.28 | 2.29 |
| f>500 | 2.65 | 2.14 | 0.19 | 2.82 |
| All f | 1.38 | 1.30 | 0.83 | 2.40 |

## 5.2 EFFECT OF DISCHARGE RATE ON LI-ION BATTERIES

The next experiment was conducted on the switching converter. An experiment was conducted using the FRA to investigate the impact of varying the DC bias on the impedance of the Li-Ion cells. The currents that were selected are 1A and 2A. Figure 5-3 shows the impedance of the battery for both these currents using the FRA.

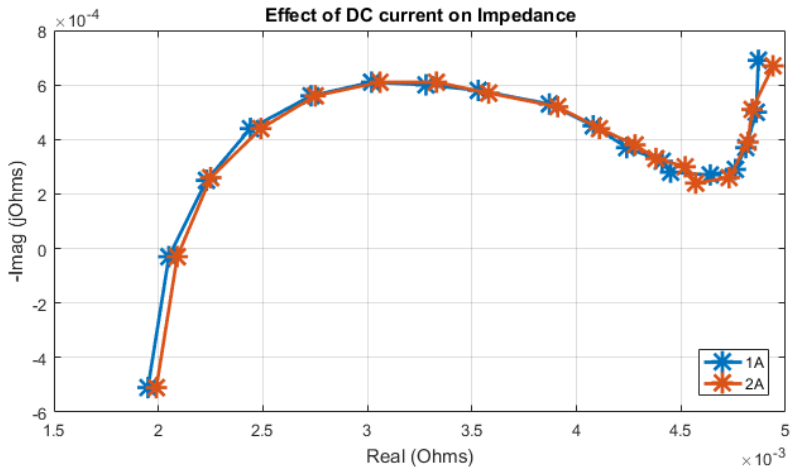


*Figure 5-3 Effect of DC current on Impedance using FRA*

It can be seen from Figure 5-3 that there is very little difference in the impedance at these current levels.

## 5.3 BIS USING THE SWITCHING CONVERTER

BIS was implemented using the switching converter for 100% SoC and 50% SoC. Figure 5-4 below shows the Nyquist and Bode magnitude plot of the Li-Ion cell at 100% SoC while discharging. For both 1A and 2A DC bias, the impedance is quite comparable to the impedance results obtained from the FRA[14] (1A), where there was little difference in found in varying the DC bias, Fig 5-3.

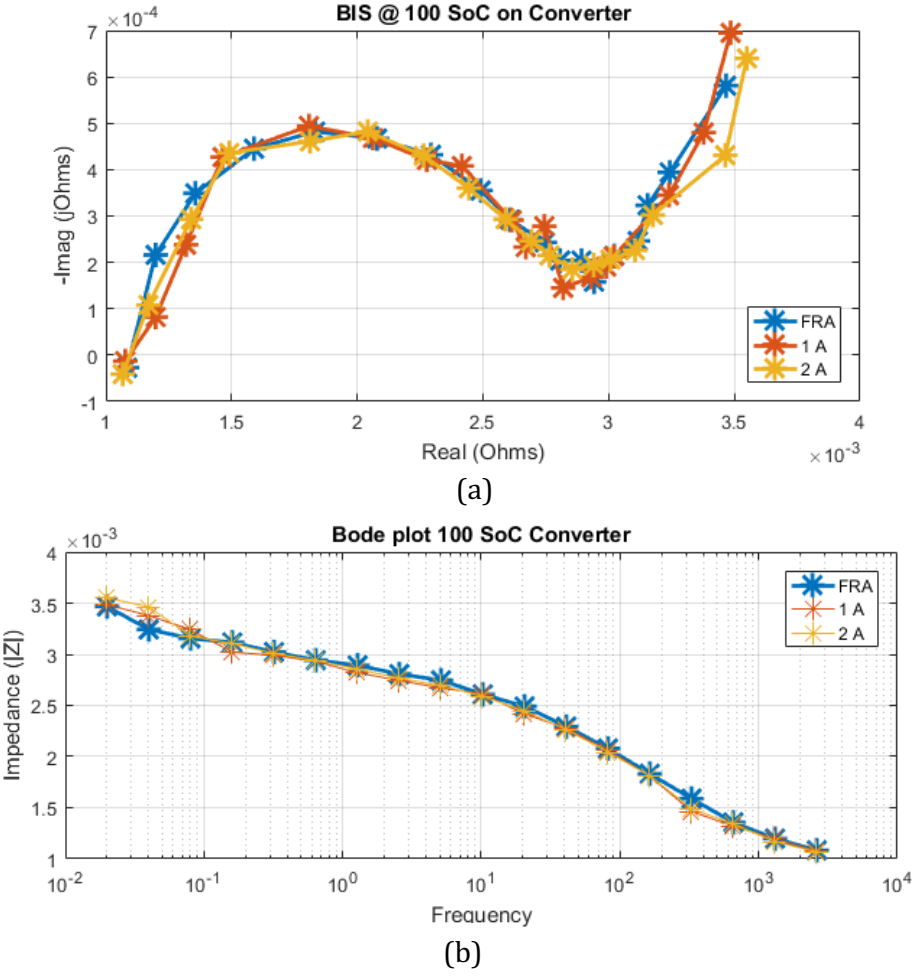


*Figure 5-4. BIS results on switching converter 100 SoC (@ 26 degrees C) (a) Nyquist plot (b) Bode Plot*

The same experiment was then conducted on the Li-Ion cell at 50% SoC, however it was done for discharging and charging. This was done to demonstrate and compare the converter's ability to perform BIS measurements during charging. The result for discharging and charging for the Li-Ion cell at 50 SoC is given in Figure 5-5. The results obtained by the

[14] The FRA was performed at 1A DC bias

converter in both charging and discharging are quite comparable to the FRA measurement of the Li-Ion cell.

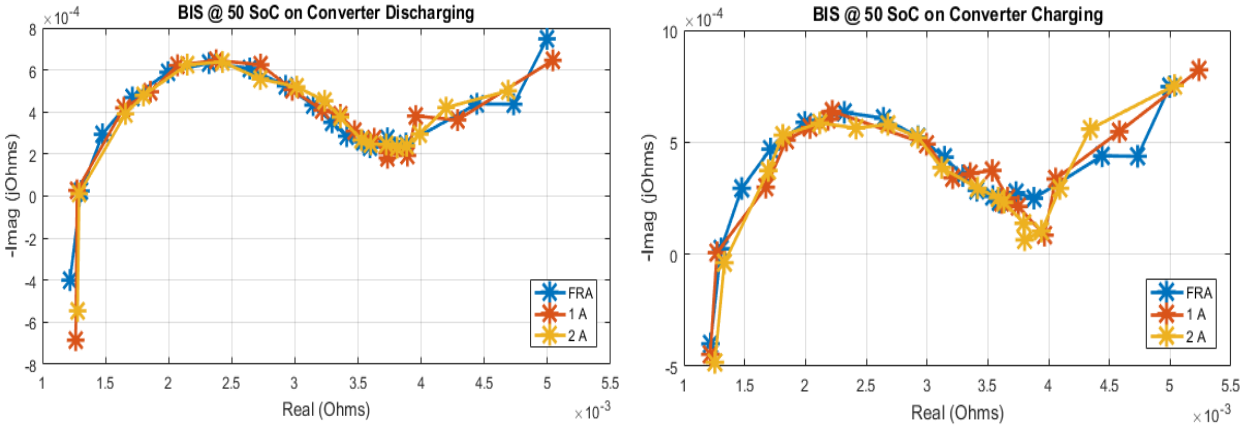


(a) (b)

*Figure 5-5. BIS results on switching converter 50 SoC discharging (@ 24 degrees C)*

Figure 5-6 shows the bode plot for BIS on the switching converter for discharging and charging (respectively) at 50 SoC.

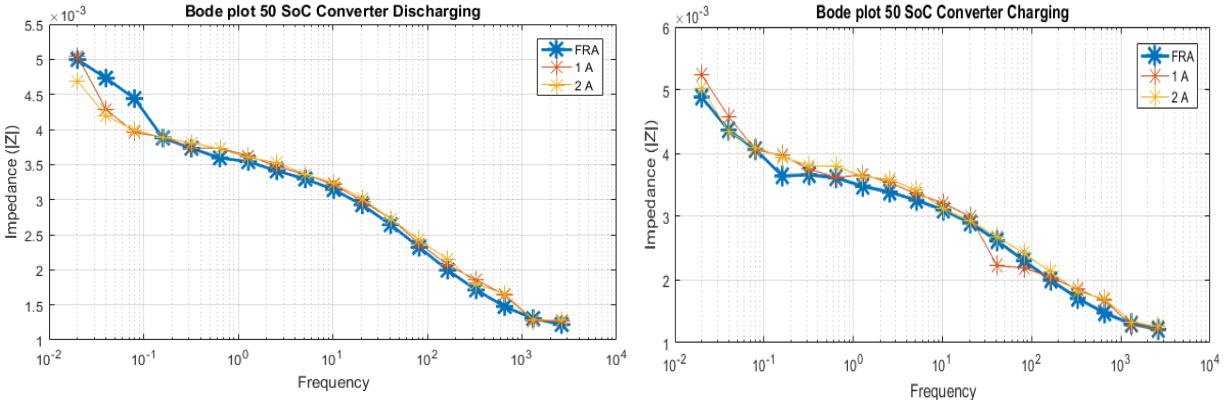


(a) (b)

Figure 5-6. BIS results on switching converter 50 SoC Charging (@ 24 degrees C)

The bode plot for the converter IS correlates well with that of the FRA for middle and higher frequencies but deviates slightly for low frequencies. Error analysis was performed for the impedance of each frequency and the average is given for each frequency group for 100 SoC and 50 SoC in Table 5-2 and Table 5-3 respectively. In general, the average error is less than 4% for the different frequency groups when the Li-Ion cell is at 100 SoC and less than 5% for both charging and discharging when the Li-Ion cell is at 50 SoC.

Table 5-2. 100 SoC Switching Converter % Error

| Current: | 1 | 2 |
|---|---|---|
| f< 1 | 4.19 | 1.84 |
| 1< f<500 | 4.49 | 1.90 |
| f>500 | 3.23 | 2.41 |
| All f | 3.86 | 1.96 |

Table 5-3. 50 SoC Switching Converter

| | Discharging | | Charging | |
|---|---|---|---|---|
| Current: | 1 | 2 | 1 | 2 |
| f< 1 | 4.19 | 4.95 | 3.27 | 4.21 |
| 1< f<500 | 3.09 | 3.57 | 4.77 | 3.15 |
| f>500 | 6.46 | 3.50 | 3.06 | 4.05 |
| All f | 4.46 | 4.49 | 4.40 | 4.21 |

## 5.4 BIS RESULTS IN PRESENCE OF CURRENT VARIATION

The converter has shown to be able to perform BIS with a reasonable level of accuracy for both charging and discharging, for different DC currents and when the battery is at different SoC. The next part of the experimentation is to test how BIS would perform during variability on the DC-bus.

A wind generator source was emulated using a controllable DC supply. The wind test data was obtained and described in Appendix A5. BIS impedance measurements were then conducted on the converter at various times as shown in Figure 5-7. The measurement times are labelled in Figure 5-7 as M1 to M5.

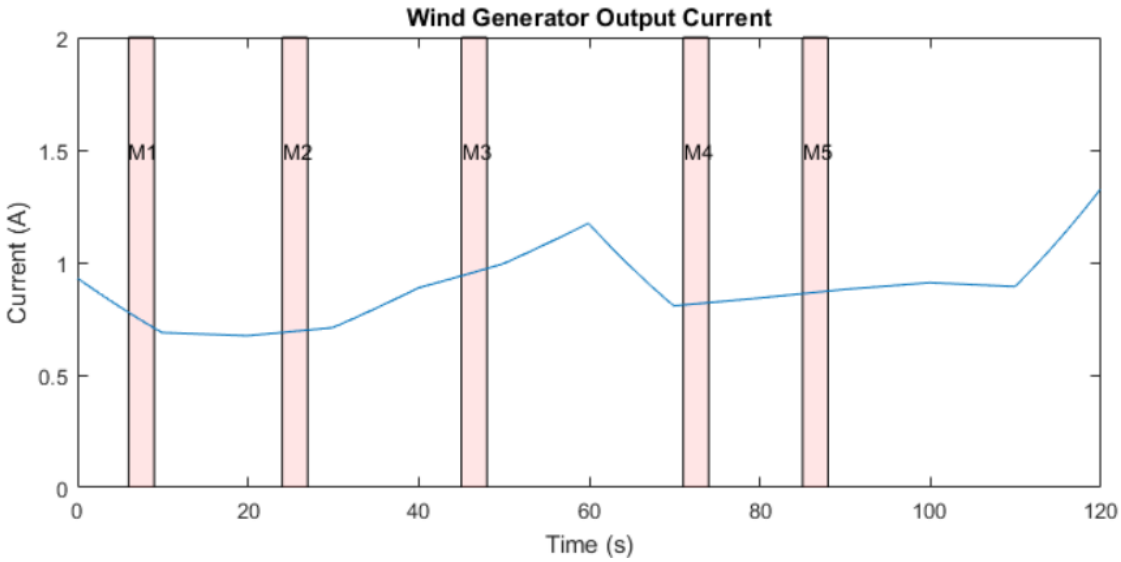


*Figure 5-7. Wind generator source current profile and BIS measurement times*

Each of these measurements are performed when the output current of the converter is changing. The frequency range that was measured was between 1 Hz and 2048 Hz. Each measurement was measured over 3 seconds, thus providing 3 periods of the lowest frequency. The frequency range was chosen to accurately measure mid and high impedance values of the battery and not the low frequencies ( f < 1Hz).

The impedance results from this experiment is given in Figure 5-8.

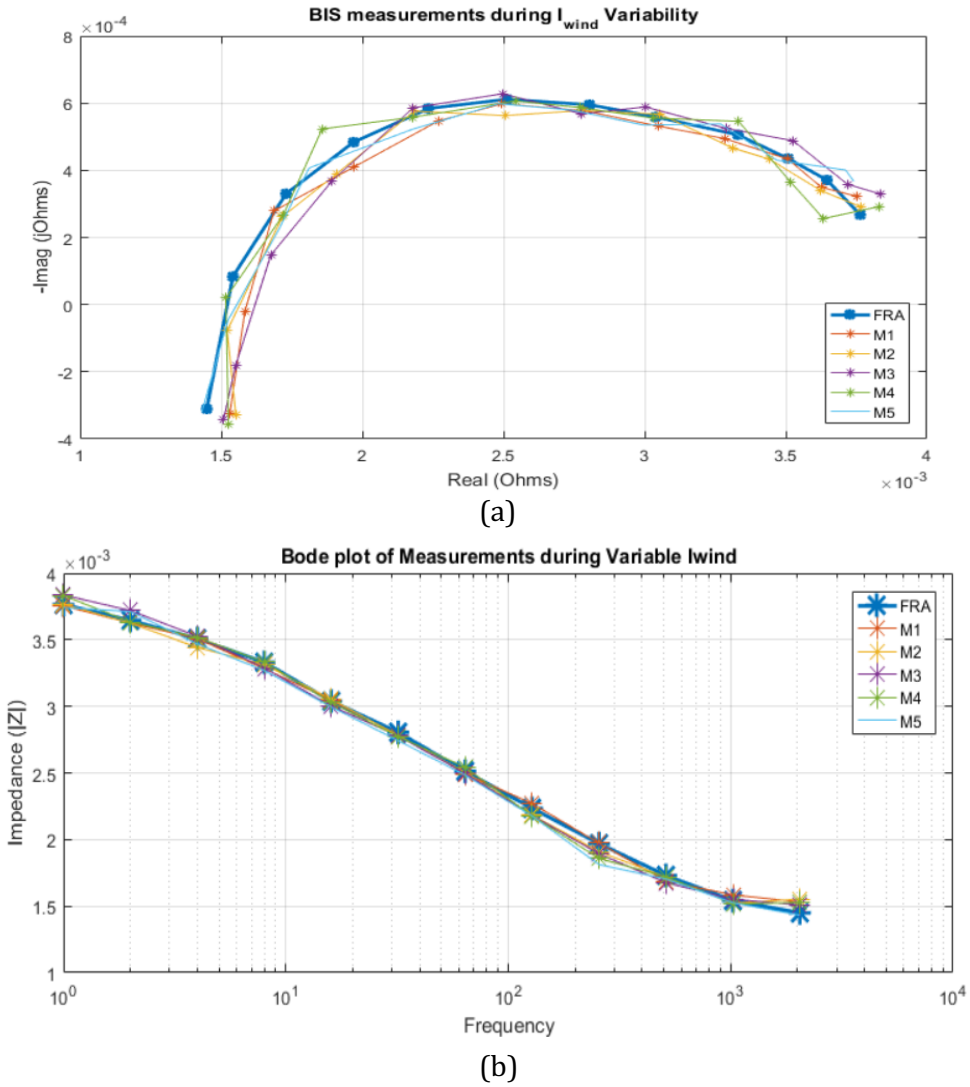


*Figure 5-8 . Results of Switching Converter (a) Nyquist Plot (b) Bode plot*

It can be seen from Figure 5-8 that the results are very similar. This was further investigated by calculating the error relative to the FRA measurement in the errors are given in Table 5-4. All measurements give a reasonable level of accuracy (less than 4%).

Table 5-4. Measurement Errors

| Current: | M1 | M2 | M3 | M4 | M5 |
|---|---|---|---|---|---|
| 1< f<500 | 0.63 | 1.29 | 1.73 | 1.42 | 2.40 |
| f>500 | 3.70 | 3.26 | 3.33 | 2.88 | 1.56 |

## 5.5 DISCUSSION AND CHALLENGES OVERCOME

The EIS/BIS performed by methods of linear signal injection through load variation showed excellent results compared to the FRA (less than 3% error), and shown to be more accurate than the IS method using the DC-DC converter. This method was shown to be highly effective at measuring the impedance of the battery, however in a practical application, it would require additional power electronics in parallel with the power converter system. Depending on the size of the battery pack, this might be impractical as a very large heatsink may be required to dissipate the heat created by the linear converter.

The EIS/BIS performed by the DC-DC converter system was shown to be slightly less accurate than the previous method compared to the FRA (less than 6% error). However, the IS signal is being injected by the power converter itself and does not require additional circuitry and is thus more practical to implement on online system.

The BIS test performed by the DC-DC converter connected to a wind generator emulator showed great results for middle and high frequency ranges. The test case only included mild current variations and thus did not demonstrate the limits of BIS in a varying system, however it did show that BIS can be performed accurately if there is some variation in current.

Some of the practical challenges experienced during experimentation was:

- Ensuring wires and connectors were short enough and did not contribute to the impedance measured from the battery.
- Ensuring the battery's temperature consistent between measurements. This was monitored by use of a thermometer.
- Ensuring sufficient rest times for the battery between measurements.

# Chapter 6. CONCLUSIONS AND RECOMMENDATIONS

This work set out to determine suitability of BIS for online condition monitoring of Li-ion battery under a varying Wind system. Two methods were investigated namely, online e-Load technique, and the duty cycle perturbation method using converters. EIS and BIS was both tested on an electronic load and a DC-DC bi-directional boost/buck converter was designed and implemented along with a battery measurement system, which could perform both EIS and BIS. The system was implemented on a low-cost prototype and controlled by LABVIEW.

It was shown that a BIS perturbation signal can be injected into a battery using a linear amplifier controllable load. The results of the controllable load experiment showed that the impedance obtained from EIS and BIS were quite comparable when comparing it to an industry standard FRA device. This shows that this multi-sine BIS technique can be used to obtain the Nyquist plot of the Li-Ion cell. The use of BIS multi-sine signals reduces measurement time associated with EIS, at a cost of a higher disturbance to the system.

It was then demonstrated that EIS and BIS can be performed on a switching converter by varying the duty cycle. Small signal analysis can be used to create a feedforward control to create accurate perturbations in the inductor current on the switching converter. These inductor current perturbations were effective at creating a battery voltage response, so that impedance could be measured.

Analogue Butterworth filters were shown to be very effective at removing high frequency switching components from the measurement signals. It was also shown that BIS on the switching converter could be performed during a battery discharge and charge. Average impedance errors when compared to an industry standard FRA was 3.80 during charging and 5.43% during discharging.

A simple wind generator emulator was created and attached to the converter system to demonstrate the converters ability to perform BIS in a system that varies periodically. Decent results were obtained from this experiment with errors less than 4% when measuring mid-range and high frequencies.

# Chapter 7. FUTURE WORK

The following are recommendations of future work in order to expand on the research conducted in this dissertation.

1. Future work should include using the equivalent circuit parameters to accurately track SoH, SoF, SoC of the batteries in a running system.
2. Reducing the amount of low frequencies in the Impedance Spectroscopy signals to significantly reduce measurement time as well as determine the minimum amount of impedance points required to produce an accurate representation of the cell.
3. Finding the limits of BIS methods on a running system, by investigating where the operating conditions of the batteries violate the required IS conditions for linearity and stability.
4. Expand the investigation of implementing IS methods in various types of electrochemical systems.

# Chapter 8. REFERENCES


[1] M. Hannan, M. Hoquw, A. Mohamed and A. Ayob, "Review of energy storage systems for electric vehicle applications: Issues and challenges," *Renewable and Sustainable Energy Reviews,* vol. 69, pp. 771-789, 2017.

[2] S. M. Rezvanizaniani, Z. Liu, Y. Chen and J. Lee, "Review and revent advances in battery health monitoring and prognostics technologies for electric vehicle (EV) safety and mobility," *Power Sources,* vol. 256, pp. 110-124, 2014.

[3] A. Waligo and P. Barendse, "A Comparison of the Different Broadband Impedance Measurement Techniques for Lithium-Ion Batteries," Cape Town, 2016.

[4] R. Koch and A. Jossen, "Speed Optimized Multisine Stimuli for Electrochemical Impedance Spectroscopy with a Switched Mode Excitation," in *Vehicle Power and Propulsion Conference*, Coimbra Portugal , 2015.

[5] C. d. Beer, P. S. Barendse and P. Pillay, "Fuel Cell Condition Monitoring Using Optimized Broadband Impedance Spectroscopy," *IEEE TRANSACTIONS ON INDUSTRIAL ELECTRONICS,,* vol. 62, no. 8, pp. 5306- 5316, 2015.

[6] S. Moore and P. Barendse, "Online condition monitoring of lithium-ion batteries using impedance spectroscopy," in *Energy Conversion Congress and Exposition (ECCE)*, Cincinnati, OH, USA, 2017.

[7] Battery University, "BU-106: Advantages of Primary Batteries," Cadex, 9 April 2017. [Online]. Available: http://batteryuniversity.com/learn/article/primary_batteries. [Accessed 10 January 2018].

[8] University of Washington, "Classification of Cells or Batteries," [Online]. Available: http://depts.washington.edu/matseed/batteries/MSE/classification.html. [Accessed 20 January 2018].

[9] Cadex, Battery University, "BU-204: How do Lithium Batteries Work?," Cadex, 31 July 2017. [Online]. Available: http://batteryuniversity.com/learn/article/lithium_based_batteries. [Accessed 3 December 2017].

[10] H. Lee, M. Yanilmaz, O. Toprakci, K. Fu and X. Zhang, "A revuew of recent developments in membrane seperators for rechargeable lithium-ion batteries," *Energy & Environmental Science,* no. 12, pp. 3857-3886, 2014.

[11] S. M. I. M. P. M. I. M. M. I. a. A. E. F. I. Ephrem Chemali, "Electrochemical and Electrostatic Energy Storage and Management Systems for Electric Drive Vehicles: State-of-the-Art Review and Future Trends," *IEEE JOURNAL OF EMERGING AND SELECTED TOPICS IN POWER ELECTRONICS,* vol. 4, no. 5, pp. 1117-1134, 2016.

[12] Battery University, "BU-808b: What Causes Li-ion to Die?," Cadex, 02 07 2017. [Online]. Available: http://batteryuniversity.com/learn/article/bu_808b_what_causes_li_ion_to_die. [Accessed 1 August 2017].

[13] Battery University, "BU-409: Charging Lithium-ion," Battery University (Cadex), 09 05 2017. [Online]. Available: http://batteryuniversity.com/learn/article/charging_lithium_ion_batteries. [Accessed 29 11 2017].

[14] Battery University , "BU-205: Types of Lithium-ion," Cadex, 15 November 2017. [Online]. Available: http://batteryuniversity.com/learn/article/types_of_lithium_ion. [Accessed 10 February 2018].

[15] A. Barré, B. Deguilhem, S. Grolleau, M. Gérard, F. Suard and D. Riu, "A review on lithium-ion battery ageing, mechanisms and estimations for automotive applications," *Journal of Power Sources,* vol. 241, pp. 680-689, 2013.

[16] Laboratory for Energy Storage and Conversion, "Lithium Ion Batteries," LESC, [Online]. Available: http://smeng.ucsd.edu/sodium-and-lithium-ion-batteries/. [Accessed 3 December 2017].

[17] C. F. D. U. S. Wladislaw Waag, "Critical review of the methods for monitoring of lithium-ion batteries in electric and hybrid vehicles," *Journal of Power Sources,* vol. 258, pp. 321-339, 2014.

[18] D. Depernet, O. Ba and A. Berthon, "Online impedance spectroscopy of lead acid batteries for storage management of a standalone power plant," *Journal of Power Sources,* vol. 219, pp. 65-74, 2012.

[19] M. S. A.-I. S. S. K. K. Daniel-Ioan Stroe, "Generalized Characterization Methodology for Performance Modelling of Lithium-Ion Batteries," *MDPI Batteries,* vol. 2, no. 37, 2016.

[20] A. Fotouhi, D. J. Auger, K. Propp, S. Longo and M. Wild, "A review on electric vehicle battery modelling: From Lithium-ion toward Lithium-Sulphur," *Renewable and Sustainable Energy Reviews,* vol. 56, pp. 1008-1021, 2016.

[21] M. Hannan, “A review of lithium-ion battery state of charge estimation and managemnet system in electric vehicle applications: Challenges and recommendations”.

[22] T. Stockley and M. B. K. Thanapalan, “Advanced EIS Techniques for performance Evaluation of Li-Ion cells,” in *IFAC World Congress*, Cape Town, 2014.

[23] W. Huang and J. A. A. Qahouq, “An Online Battery Impedance Measurement Method Using DC–DC Power Converter Control,” *IEEE TRANSACTIONS ON INDUSTRIAL ELECTRONICS,* vol. 61, no. 11, pp. 5987-5995, 2014.

[24] D. A. Howey, V. Y. Paul D.Mitcheson, G. K.Offer and N. P.Brandon, “Online Measurement of Battery Impedance Using Motor Controller Excitation,” *IEEE Transactions on vehicular technology,* vol. 63, no. 6, pp. 2557-2566, 2014.

[25] J. Larmhie, “CURRENT INTERRUPT TECHNIQUES FOR CIRCUIT MODELLING”.

[26] J.-B. J. T.-H. K. a. H.-J. K. Dong-Hyun Shin, “Modeling of Lithium Battery Cells for Plug-In Hybrid Vehicles,” *Journal of Power Electronics,* vol. 13, no. 3, pp. 429 - 436, 2013.

[27] T. Jaumann, J. Balach, U. Langklotz, V. Sauchuk, M. Fritsch, A. Michaelis, V. Teltevskij, D. Mikhailova, S. Oswald, M. Klose, G. Stephani, R. Hauser, J. Eckert and L. Giebeler, “Lifetime vs. rate capability: Understanding the role of FEC and VC in high-energy Li-Ion batteries with nano-silicon anodes,” *Energy Storage Materials,* vol. 6, pp. 26-35, 2014.

[28] C. Fleischer, W. Waag, H.-M. Heyn and D. U. Sauer, “On-line adaptive battery impedance parameter and state estimation considering physical principles in reduced order equivalent circuit battery models: Part 1. Requirements, critical review of methods and modeling,” *Journal of Power Sources,* vol. 260, pp. 276-291, 2014.

[29] T.-T. Nguyen, V.-L. Tran and W. Choi, “Development of the Intelligent Charger with Battery State-Of-Health Estimation Using Online Impedance Spectroscopy,” in *Industrial Electronics (ISIE)*, Instanbul Turkey, 2014.

[30] N. Lohmann, P. Weßkamp, P. Haußmann, J. Melbert and T. Musch, “Electrochemical impedance spectroscopy for lithium-ion cells: Test equipment and procedures for aging and fast characterization in time and frequency domain,” *Journal of Power Sources,* vol. 273, pp. 613-623, 2015.

[31] A. Densmore and M. Hanif, "Determining Battery SoC Using Electrochemical Impedance Spectroscopy and the Extreme Learning Machine," in *2015 IEEE 2nd International Future Energy Electronics Conference (IFEEC)*, Taipei, 2015.

[32] D. I. Stroe, M. Swierczynski, A. I. Stan, V. Knap, R. Teodorescu and S. J. Andreasen, "Diagnosis of lithium-ion batteries state-of-health based on electrochemical impedance spectroscopy technique," in *IEEE Energy Conversion Congress and Exposition (ECCE)*, Pitsburg, 2014 .

[33] R. Koch and A. Jossen, "Impedance Spectroscopy for Battery Monitoring with Switched Mode Amplifiers," in *16th International Power Electronics and Motion Control Conference and Exposition* , Antalya,Turkey, 2014.

[34] Gamry, "Basics of Electrochemical Impedance Spectroscopy," Gamry Instruments, [Online]. Available: https://www.gamry.com/application-notes/EIS/basics-of-electrochemical-impedance-spectroscopy/. [Accessed 18 09 2017].

[35] J. Giner-Sanz and V. P.-H. E.M. Ortega, "Optimization of the Perturbation Amplitude for Impedance Measurements in a Commerical PEM Fuel Cell Using Total Harmonic Distortion," *Fuel Cells,* vol. 16, no. 4, pp. 469-479, 2016.

[36] R. Nazer, V.Cattin, P.Granjon, M. Montaru and M. Ranieri, "Broadband Identification of Battery Electrical Impedance for HEVs," *IEEE Transactions on vehicular technology,* vol. 62, no. 7, pp. 2896-2905, 2013.

[37] E. Din, C. Schaef, K. Moffat and J. T. Stauth, "A Scalable Active Battery Management System With Embedded Real-Time Electrochemical Impedance Spectroscopy," *IEEE Transactions on Power Electronics* , vol. 32, no. 7, pp. 5688-, 2017.

[38] P. Hong, J. Li, L. Xu, M. Ouyang and C. Fang, "Modeling and simulation of parallel DC/DC converters for online AC impedance estimation of PEM fuel cell stack," *International Journal of Hydrogen Energy,* vol. 41, no. 4, pp. 3004-3014, 2016.

[39] A. Debenjak, J. Petrovcic, P. Boskoski, B. Musizza and D. Juricic, "Fuel Cell Condition Monitoring System Based on Interconnected DC-DC Converter and Voltage Monitor," *IEEE Transactions on Industrial Electronics,* vol. 62, no. 8, pp. 5293-5305, 2015.

[40] O. Bethoux, M.Hilairet and T. Azib, "A new on-line state-of-health monitoring technique dedicated to PEM fuel cell to PEM fuel cell," in *Industrial Electronics IECON*, Porta Portugal, 2009.

[41] J. A. A. Qahouq, “Online Battery Impedance Sectrum Measurement Method,” in *Applied Power Electronics Conference and Exposition*, Long Beach, CA USA, 2016.

[42] N. Katayama and S. Kogoshi, “Real-Time Electrochemical Impedance Diagnosis for Fuel Cells Using a DC-DC Converter,” *IEEE Transactions on Energy Conversion,* vol. 30, no. 2, pp. 707-713, 2015.

[43] D. Depernet, A. Narjiss, F. Gustin, D. Hissel and M.-C. Pera, “Integration of electrochemical impedance spectroscopy functionality in proton exchange membrane fuel cell power converter,” *International Journal of Hydrogen Energy,* vol. 41, no. 11, pp. 5378-5388, 2016.

[44] J. P. Christophersen, J. Morrison, W. Morrison and C. Motloch, “Rapid Impedance Spectrum Measurements for State-of-Health Assessment of Energy Storage Devices,” *SAE International Journal of Passenger Cars-Electronic and Electrical Systems,* vol. 5, pp. 246-256, 2012.

[45] Z. Liao and X. Ruan, “Control Strategy of Bi-directional DC-DC Converter for a Novel Stand-alone Photovoltaic Power System,” in *IEEE Vehicle Power and Propulsion Conference (VPPC)*, Harbin, China, 2008.

[46] H. Abdel-Gawad and V. Sood, “Small-Signal Analysis of Boost Converter, including Parasitics, operating in CCM,” in *IEEE*, Oshawa, Canada, 2014.

[47] N. Mohan, T. M. Undeland and W. P. Robbins, Power Electronics. Converters, Applications, and Design, John Wiley & Sons, INC, 2003.

[48] M. S. Hassan and A. A. Elbaset, “Small-Signal MATLAB/Simulink Model of DC-DC Buck Converter using State-Space Averaging Method,” in *17th International Middle-East Power System Conferennce (MEPCON'15)*, Mansoura, Egypt, 2015.

[49] [Online]. Available: http://www.ni.com/white-paper/4844/en/.

[50] J. Karki, “Active Low-Pass Filter Design,” Texas Instruments- AAP precision Anlag, Dallas, Texas, 2002.

[51] Infineon, “International Rectifiers,” 12 4 2006. [Online]. Available: https://www.infineon.com/dgdl/irs2108.pdf?fileId=5546d462533600a4015356764 9d627a8. [Accessed 22 12 2017].

[52] J. Karki, “Analysis of the Sallen-Key Architecture,” July 2002. [Online]. Available: http://www.ti.com.cn/cn/lit/an/sloa024b/sloa024b.pdf. [Accessed 3 December 2017].

[53] South African National Space Agency, “Current Hermanus Weather,” 01 01 2018. [Online]. Available: http://weather.hmo.ac.za/data. [Accessed 18 01 2018].

[54] K. Suresh and D. Arulmozhiyal, “Design and Implementation of Bi-Directional DC-DC Converter for Wind Energy Systems,” *Circuits and Systems,* vol. 7, pp. 3705-3722, 2016.

[55] D. M. Bellur and M. Kazimierczuk, “DC-DC Converters for electric vehicle applications,” in *Electrical Insulation Conference and Electrical Manufacturing Expo*, Nashville, 2007.

[56] R. G. A. Bondarenko A. S., “In Progress in Chemometrics Research (the program is available online at http://www.abc.chemistry.bsu.by/vi/analyser/),” *Nova Science Publishers,* pp. 89-102, 2015.

[57] International Rectifier, “IRFP260N,” [Online]. Available: https://www.infineon.com/dgdl/irfp260n.pdf?fileId=5546d462533600a4015356289dcf1fe2. [Accessed 15 1 2018].

# APPENDIX

## A1. STEP TEST OF LITHIUM ION CELL

A step test was performed on the Li-Ion cells as a comparison for the EIS measurements. It was also used to obtain parameters for simulations. For comparison, the step response performed on the Li-Ion cells as was done by [25] on a Fuel Cell system. The cell was initially discharging at 4A, the cell was then made to discharge at 2A using the electronic load, and the response was measured by the NI-DAQ and LABVIEW. The resulting voltage response is shown in Figure 8-1 below.

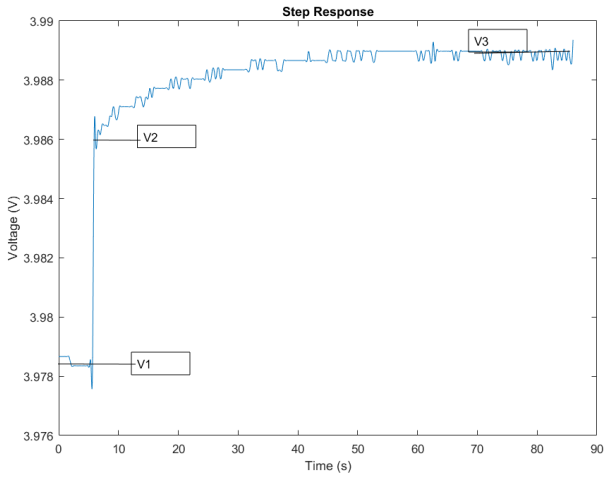


*Figure 8-1. Voltage response to current step change*

This voltage response can be modelled as a second order exponential decay. This is shown by the equation below. The parameters were fit to the voltage response in Figure 8-8 above using the trust region reflective algorithm.

$$V(t) = V_3 + Ae^{(\frac{-t}{\tau_1})}$$

The equivalent circuit used to map this response was a Thevinin equivalent circuit shown in Figure 8-2 below.

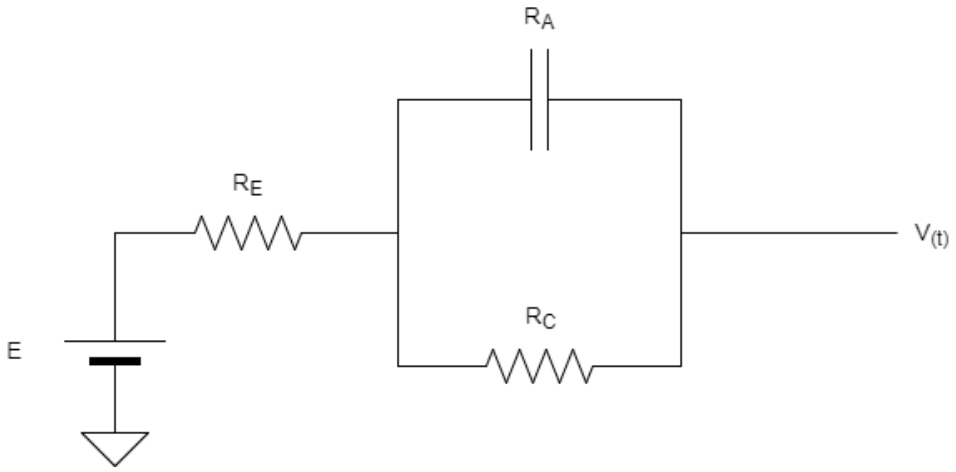


*Figure 8-2 Thevenin Equivalent Circuit.*

The following equations from [25] were used to find the Resistor and Capacitor values of the Equivalent Circuit

$$\tau_1 = R_a C_a$$
$$A = R_a(I_2 - I_1)$$
$$V_1 = E - I_1(R_a + R_e)$$
$$V_2 = E - I_2 R_e - I_2(R_a + R_e)$$
$$V_3 = E - I_2(R_a + R_e)$$

Rearranging and solving for the unknowns results in Table 8-1 below.

*Table 8-1 Parameters of Equivalent Circuit*

| Parameter | Value |
|---|---|
| Re | 0.002 |
| Ra | 0.0012 |
| Ca | 55.7 |
| E | 4 |

## A2. LI-ION CELL DATASHEET

# ePLB C High Energy Product


**Technology**
Lithium Ion Polymer Battery
$Li[NiCoMn]O_2$-based Cathode
Graphite-based Anode
High Energy Density
Optimized for PHEV, EV

### Product General Specification

**Mechanical Characteristics**

| | |
|---|---|
| Model | C020 |
| Length | 217.0 ± 1 mm (excluding terminal) |
| Width | 129.0 ± 1 mm |
| Thickness | 7.2 ± 0.2 mm |
| Weight | approx. 428 g |

**Electrical Characteristics**

| | |
|---|---|
| Nominal Voltage | 3.65 V |
| Nominal Capacity | 20 Ah |
| AC Impedance (1 KHz) | < 3 mΩ |
| Specific Energy | 174 Wh/Kg |
| Energy Density | 370 Wh/L |
| Specific Power(DOD50%, 10sec) | 2300 W/Kg |
| Power Density(DOD50%, 10sec) | 4600 W/L |

**Operating Conditions**

| | |
|---|---|
| Charge Conditions : | |
| Recommended Charge Method | CC/CV |
| Maximum Charge Voltage | 4.15 V |
| Recommended Charge Current | 0.5 C Current |
| Discharge Conditions : | |
| Recommended Voltage Limit for Discharge | 3.0 V |
| Lower Voltage Limit for Discharge | 2.5 V |
| Maximum Discharge Current (Continuous) | up to 5 C Current |
| Maximum Discharge Current (Peak < 10 sec) | 10 C Current |
| Operating Temperature : | -30°C / + 55°C |
| Recommended Charge Temperature | 0°C / + 40°C |
| Storage Temperature | -30°C / + 55°C |

Cycle Life at 25°C : (1 C Charge / 1 C Discharge, DOD100%)
1000 Cycles to 80% Nominal Capacity

### ePLB C020 Performance

Rate Capability

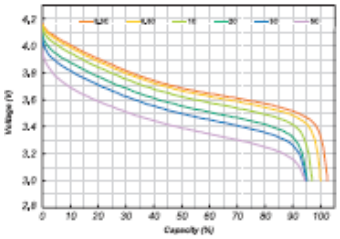

CHARGE : CC(0.5C)/CV(4.15V to 0.05C) at 25°C
DISCHARGE : CC to 3.0V at 25°C

Pulse Power Characteristics

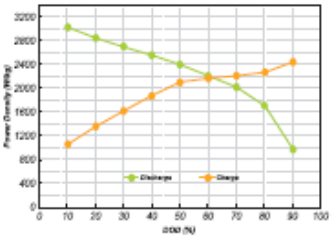

HPPC calculated from FreedomCAR Battery Test Manual

Cycle Life

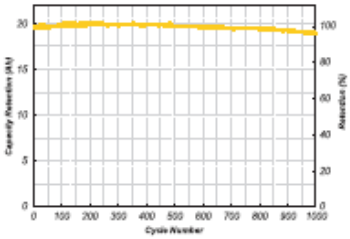

CHARGE : CC(1.0C)/CV(4.15V to 0.05C) at 25°C
DISCHARGE : CC(1.0C) to 3.0V at 25°C (DOD100%)

EiG

## A3. MATLAB-CODE

The following code was used in creating an optimal BIS signal.

**BIS Signal Optimization**

```
%==========Create BIS Optimized Signal==========%
%   Author:    Sean Moore

amp_dc = 0.5; %DC Value
amp_percentage= 10; %Percentage of DC value
amplitude = amp_percentage*amp_dc/100;

% Inital Nyquist Plot values
f = [0.02,0.04,0.08,0.16,0.32,0.64,1.28,2.56,5.12,10.24,20.48,40.96,81.92,163.84,327.68,655.36,1310.72,2621.44];
z_real = [0.005163579,0.004821629,0.004665703,0.004519723,0.004423447,0.004291001,0.004168372,0.004026705,0.0038
z_imag = [0.000865098,0.000580775,0.000423726,0.000370201,0.000328379,0.000316046,0.00035324,0.000404381,0.00049


z= [z_real+i*z_imag];

lowest_frequency = min(f);
highest_frequency = max(f);
longest_period = 1/lowest_frequency;
t = 0:1/highest_frequency:longest_period;

a_unoptimized = amplitude*ones(size(f));

% Optimize Amplitudes
z_new = abs(z);
i_new = z_new.^-1;
i_max = max(i_new);
i_norm = i_new/i_max;
a_optimized = i_norm *amplitude;



% Build a_Unoptimized graph
unoptimized_graph = 0;
for k = 1:1:size(a_unoptimized,2)
    unoptimized_graph = unoptimized_graph +  a_unoptimized(k)*sin(t(:)*f(k));
end
unoptimized_graph = unoptimized_graph;


% Build a_optimized graph
optimized_graph = 0;
for k = 1:1:size(a_optimized,2)
    optimized_graph = optimized_graph +  a_optimized(k)*sin(t(:)*f(k));
end


if 1==1
    disp('phaseOptimization');
    options = optimset('Display','final','TolFun',1.e-3);
    x0 = zeros(1,size(a_optimized,2));
    [x,fval,exitflag,output] = fminsearch(@(x)phaseFunction(x,f,a_optimized,t),x0,options);
    phase_optimized_graph = 0;
    for k = 1:1:size(a_optimized,2)
        phase_optimized_graph = phase_optimized_graph +  a_optimized(k)*sin(t(:)*f(k)+x(k));
    end
end
```

## A4. BIS TESTING VALUES

Table 8-2. Optimized Multi-sine *signal parameters*

| | DC = 0.5 A | | DC = 1 A | | DC = 2 A | |
|---|---|---|---|---|---|---|
| Frequency | $a_n$ | $\theta_n$ | $a_n$ | $\theta_n$ | $a_n$ | $\theta_n$ |
| 0.02 | 0.013 | -0.815 | 0.026 | -0.815 | 0.052 | -0.815 |
| 0.04 | 0.014 | 0.243 | 0.028 | 0.243 | 0.056 | 0.243 |
| 0.08 | 0.014 | 0.946 | 0.029 | 0.946 | 0.058 | 0.946 |
| 0.16 | 0.015 | -0.158 | 0.030 | -0.158 | 0.060 | -0.158 |
| 0.32 | 0.015 | 1.833 | 0.031 | 1.833 | 0.061 | 1.833 |
| 0.64 | 0.016 | -1.557 | 0.032 | -1.557 | 0.063 | -1.557 |
| 1.28 | 0.016 | 0.728 | 0.032 | 0.728 | 0.065 | 0.728 |
| 2.56 | 0.017 | -0.256 | 0.034 | -0.256 | 0.067 | -0.256 |
| 5.12 | 0.018 | -0.332 | 0.035 | -0.332 | 0.070 | -0.332 |
| 10.24 | 0.019 | 0.070 | 0.037 | 0.070 | 0.074 | 0.070 |
| 20.48 | 0.020 | 0.838 | 0.040 | 0.838 | 0.081 | 0.838 |
| 40.96 | 0.023 | -1.387 | 0.045 | -1.387 | 0.090 | -1.387 |
| 81.92 | 0.026 | -1.620 | 0.052 | -1.620 | 0.104 | -1.620 |
| 163.84 | 0.031 | 2.698 | 0.062 | 2.698 | 0.123 | 2.698 |
| 327.68 | 0.037 | 1.016 | 0.073 | 1.016 | 0.146 | 1.016 |
| 655.36 | 0.044 | -4.532 | 0.087 | -4.532 | 0.175 | -4.532 |
| 1310.72 | 0.050 | 1.077 | 0.100 | 1.077 | 0.200 | 1.077 |
| 2621.44 | 0.049 | 1.492 | 0.099 | 1.492 | 0.198 | 1.492 |

## A5. WIND SAMPLE DATA

Wind data was created using data from the South African National Space Agency (SANSA) situated in Hermanus in the Western Cape [53]. A random normal distribution method was used based on the data obtained from [53] to create 120 seconds of sample data. The wind data is shown below in Figure 8-3 Sample Wind Turbine Data.

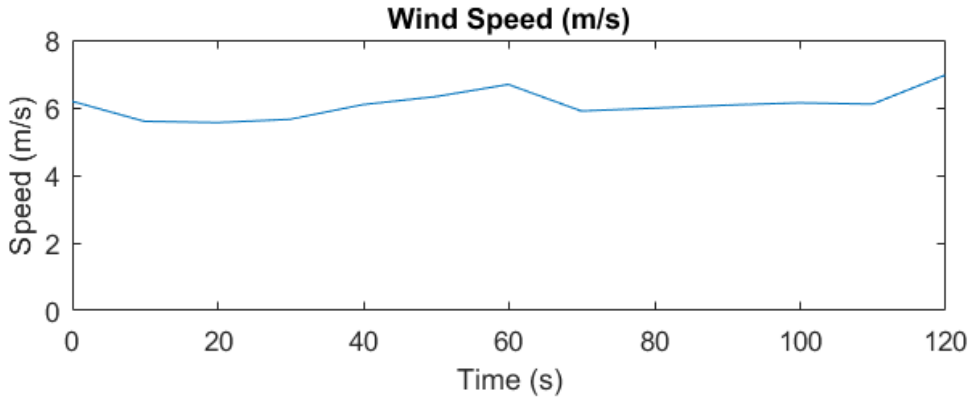


*Figure 8-3 Sample Wind Turbine Data*

In recent years, it has become common to find hybrid distributed generation systems. There are multiple types of wind generators that are used for small microgrids and residential usages. The most common type of wind turbines for residential use is the horizontal axis wind turbine which generally has 3 or 4 blades. The turbine extracts power from the wind. The mechanical power of the wind equation (7-1). The power that is captured from the wind turbine is given by equation (7-2) [54].

$$P_{wind} = \frac{pAv^3}{2} \quad (8\text{-}1)$$

$$P_{turbine} = T_m\omega_r = C_p\frac{1}{2}p\pi R^2v^3 \quad (8\text{-}2)$$

Where $A$ is the swept area of the blades, $p$ is the air density and $v$ is the wind speed, $R$ is the radius of the blades, and $C_P$ is the power coefficient of the turbine.

$P_{turbine}$ then goes into a Permanent Magnet Synchronous Generator (PMSG) where the energy is transformed into electrical energy. The wind turbine that is modelled is assumed to be small and thus has low inertia. The wind generator connects the DC bus and follows the output voltage of the DC-DC Converter.

## A6. EQUIVALENT CIRCUIT MODELLING

As was discussed in Chapter 2.5, batteries can be monitored by creating an equivalent circuit and pulling out the circuit parameters from the measurements. Changes in these elements can then be monitored and different states can be inferred. The circuit that was used to for parameterizing the Nyquist plot is shown in Figure 8-4 below. This is a modified ECCE that was used in [3] [24]. Each element is label according to the internal mechanism of the Li-Ion cell it represents.

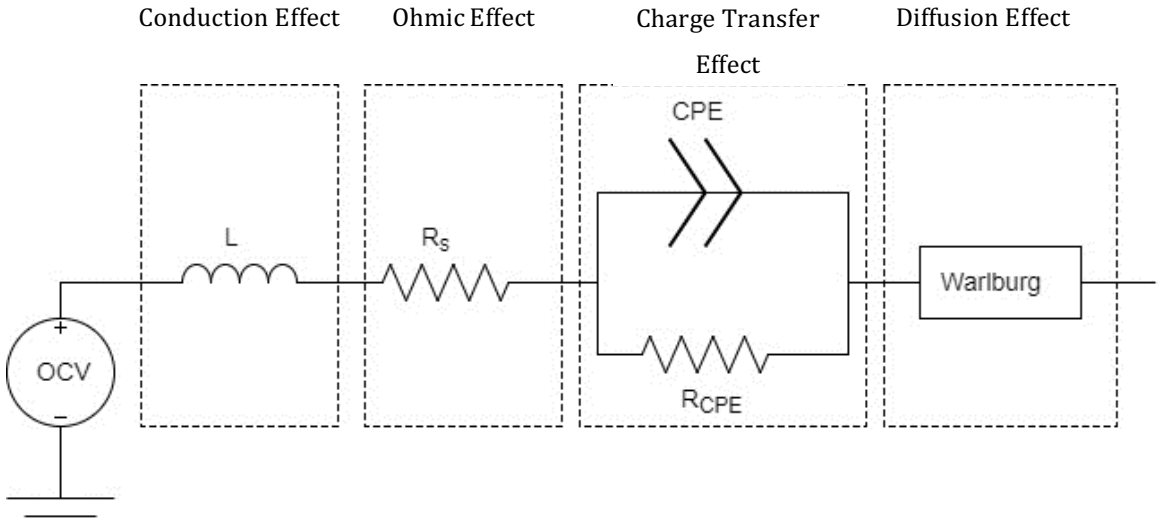


*Figure 8-4 Li-Ion equivalent circuit*

The Levenberg Marquardt non-linear least squares fitting algorithm was used to extract equivalent circuit parameters from the impedance data. The purpose of parameterization in this dissertation is merely to demonstrate how parameters of an equivalent circuit change for different selected states and there no exhaustive tests conducted to pull out parameters at every possible state.

It should be noted that online condition monitoring is essentially carried out using the model parameters of the EEC developed from the Nyquist and Bode plots. The variation in the parameters of the EEC describe the internal processes of the cell/battery and therefore used to deduce the condition of the cell/battery. Parameter estimation for the Li-ion cell is demonstrated using the Nyquist plot obtained from BIS test at 100 SoC, and 0.5 A on the e-load shown in Figure 8-5.

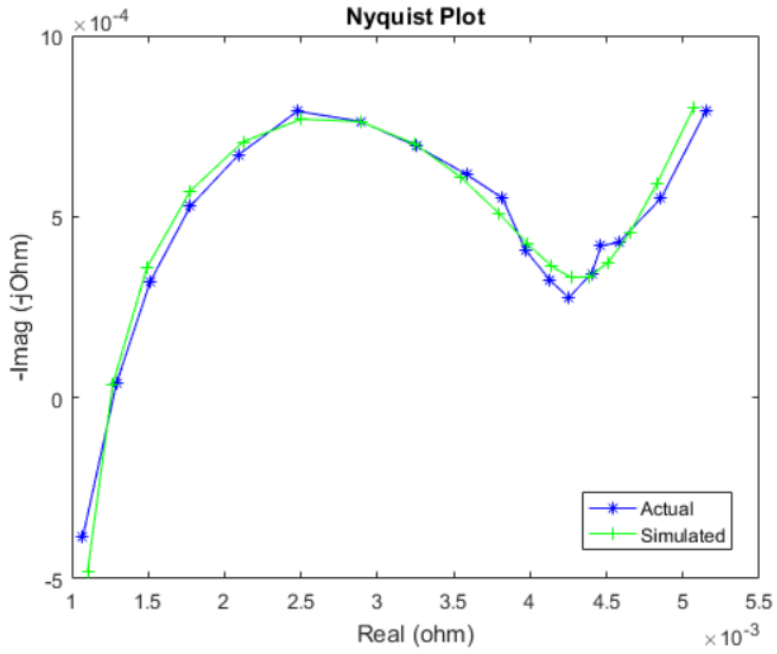


*Figure 8-5. Nyquist plot of BIS on DC load at 100 SoC vs simulated.*

The extracted parameter values at 100, 75 and 50 SoCs are further compared as shown in Table 8-3. Note that, the depression factor ($\varphi$) of the CPE element was fixed at 0.6 and the virtual inductance at $5\times10^{-8}H$. Fixing the inductor as well as the depression factor is to aid computational time as was done in [3].

Table 8-3 Parameter Variation

| SOC | 100 | 75 | 50 |
|---|---|---|---|
| $R_s$ | 0.00063996 | 0.00069758 | 0.00113 |
| $R_{CPE}$ | 0.003729 | 0.003682 | 0.0035544 |
| $CPE$ | 11.9218 | 12.3432 | 14.0397 |
| $\varphi$ | 0.5379 | 0.5379 | 0.5379 |
| $Z_{Warlburg}$ | 2664.8 | 2911.5 | 3477.2 |

The parameter variation across the estimated SoC is illustrated in Figure 8-6. The values of the equivalent circuit parameter decrease with increasing state of charge. Except for the CPE resistance which increases with increasing SoC.

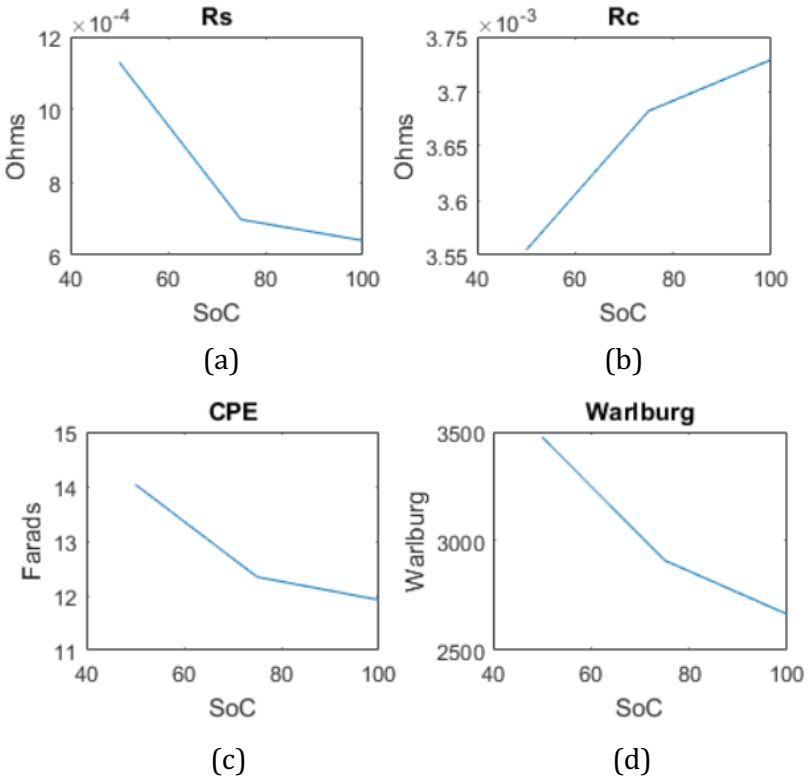


*Figure 8-6. Change of Equivalent Circuit Parameters with Change in SOC*

The next test investigates the relationship between SoC by observing the variation of the obtained Nyquist plots as shown in Figure 8-7. It is observed that, as SoC decreases, there is a general shift of the impedance spectra to the right. Abrupt variations are more prevalent on the low frequency spectra as lower frequency side of the spectra is more affected by the diffusion process of the cell. The higher frequency spectra are also clearly observed and characterized by an increase in the internal cell resistance using the right-side shift of the impedance spectra. Similar observations were made in literature to confirm the internal process of the Li-Ion cell at different SoCs [3].

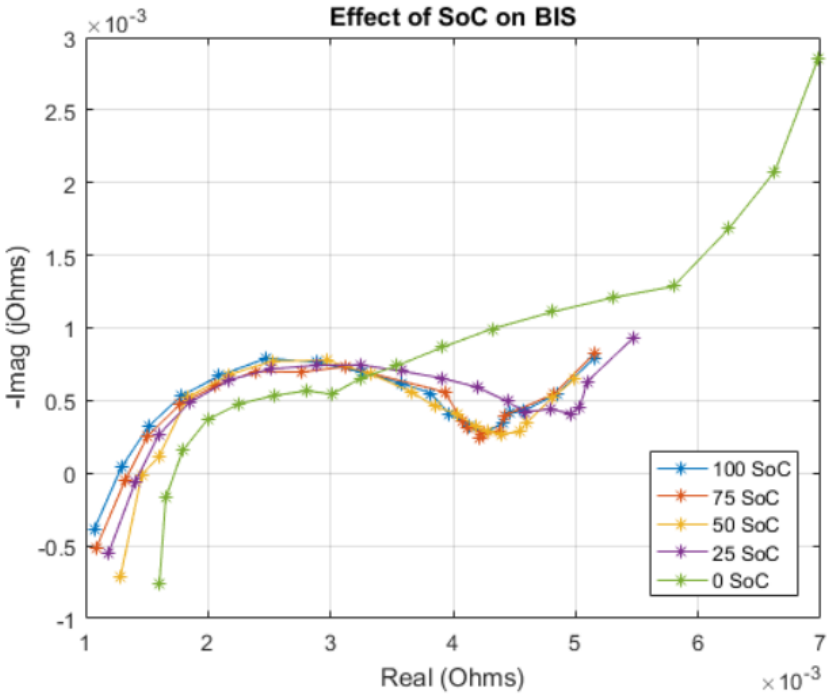


*Figure 8-7. BIS plots showing the effects of SoC on Impedance (@24 degress C)*

## A7. CONVERTER SIMULINK MODEL

The full converter model is shown in Figure 8-8 below. It consists of a battery model on the left, the DC-DC Converter highlighted in blue, and a DC_BUS which has a resistive load as well as a wind generator connected to it.

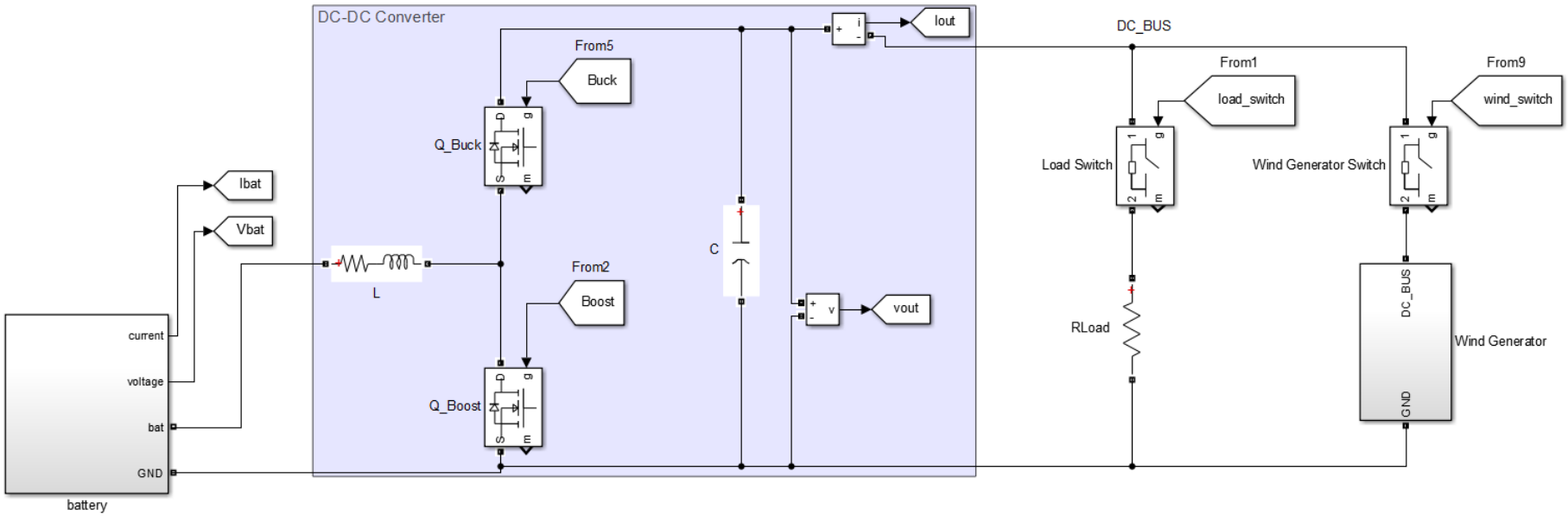


*Figure 8-8. Simulink Model of Converter*

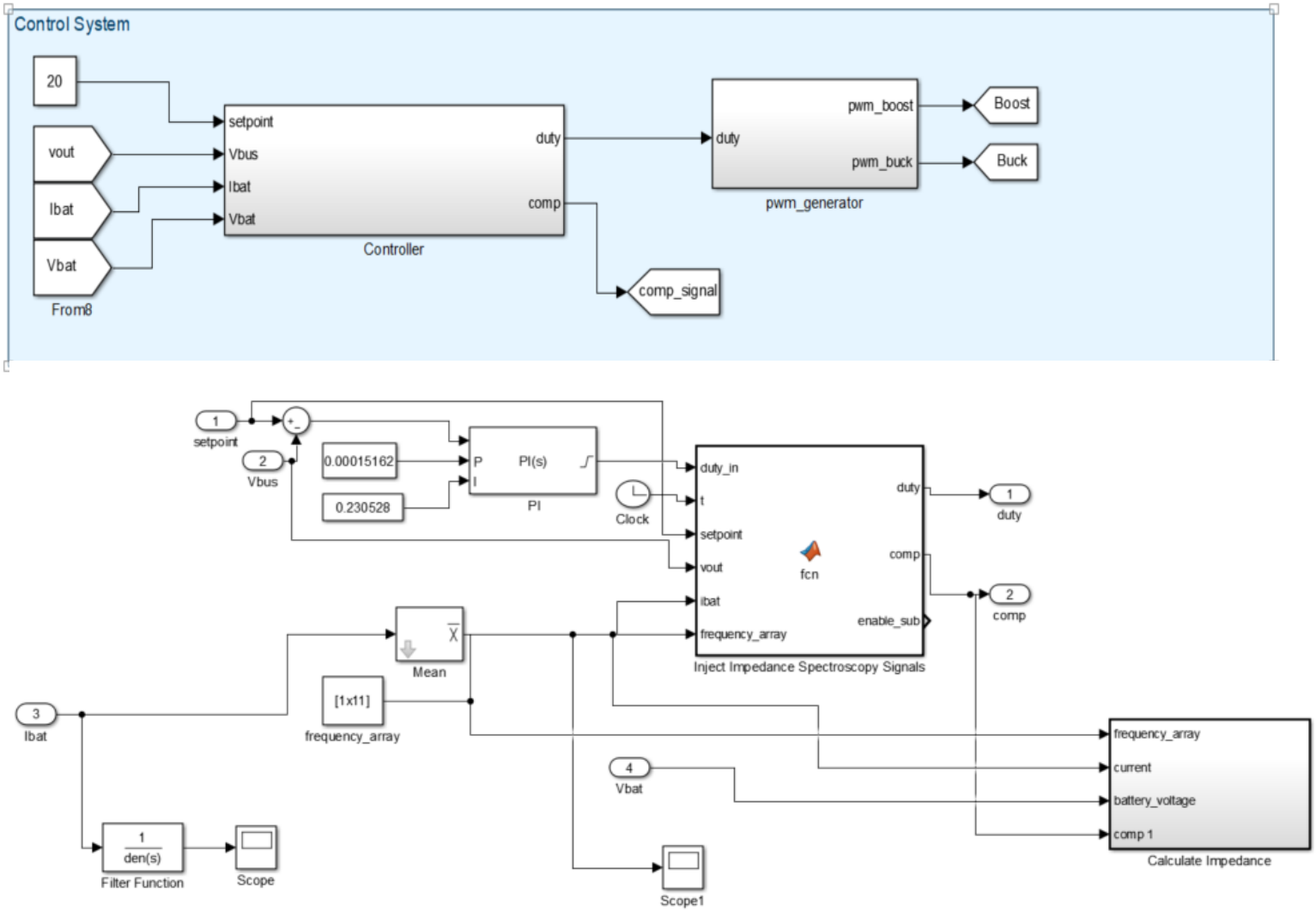


*Figure 8-9. Simulink Control Diagram*

# Chapter 9. ETHICS FORM

Application for Approval of Ethics in Research (EiR) Projects
Faculty of Engineering and the Built Environment, University of Cape Town

## APPLICATION FORM

**Please Note:**
Any person planning to undertake research in the Faculty of Engineering and the Built Environment (EBE) at the University of Cape Town is required to complete this form **before** collecting or analysing data. The objective of submitting this application *prior* to embarking on research is to ensure that the highest ethical standards in research, conducted under the auspices of the EBE Faculty, are met. Please ensure that you have read, and understood the **EBE Ethics in Research Handbook** (available from the UCT EBE, Research Ethics website) prior to completing this application form: http://www.ebe.uct.ac.za/ebe/research/ethics1

| APPLICANT'S DETAILS | | |
|---|---|---|
| Name of principal researcher, student or external applicant | | Sean Moore |
| Department | | Electrical Engineering |
| Preferred email address of applicant: | | Mrxsea001@myuct.ac.za |
| If Student | Your Degree: e.g., MSc, PhD, etc. | MSc(Eng) Electrical Engineering |
| | Credit Value of Research: e.g., 60/120/180/360 etc. | 180 |
| | Name of Supervisor (if supervised): | Paul Barendse |
| If this is a researchcontract, indicate the source of funding/sponsorship | | |
| Project Title | | Online Condition Monitoring of Li-Ion batteries |

**I hereby undertake to carry out my research in such a way that:**

- there is no apparent legal objection to the nature or the method of research; and
- the research will not compromise staff or students or the other responsibilities of the University;
- the stated objective will be achieved, and the findings will have a high degree of validity;
- limitations and alternative interpretations will be considered;
- the findings could be subject to peer review and publicly available; and
- I will comply with the conventions of copyright and avoid any practice that would constitute plagiarism.

| SIGNED BY | Full name | Signature | Date |
|---|---|---|---|
| **Principal Researcher/ Student/External applicant** | Sean Moore | Signed by candidate | 4/12/07 17 |

| APPLICATION APPROVED BY | Full name | Signature | Date |
|---|---|---|---|
| Supervisor (where applicable) | Paul Barendse | | 4/12/07 17 |
| **HOD (or delegated nominee)** Final authority for all applicants who have answered NO to all questions in Section1; and for all Undergraduateresearch (Including Honours). | S. CHOWDHURY | | 5/12/07 |
| **Chair : Faculty EIR Committee** For applicants other than undergraduate students who have answered YES to any of the above questions. | | | |

Page 1 of 1